Articulated Mechanisms and Electrostatic Actuators for Autonomous Microrobots

by

Richard Yeh

B.S. (University of California at Berkeley) 1993

M.S. (University of California at Los Angeles) 1995

A dissertation submitted in partial satisfaction of the

requirements for the degree of

Doctor of Philosophy

in

Engineering-Electrical Engineering

and Computer Science

in the

GRADUATE DIVISION

of the

UNIVERSITY OF CALIFORNIA, BERKELEY

Committee in charge:

Professor Kristofer S. J. Pister, chair

Professor Roger T. Howe

Professor Dorian Liepmann

Spring 2001

The dissertation of Richard Yeh is approved:

Professor Kristofer S. J. Pister, Chair	Date
Professor Roger T. Howe	Date
Professor Dorian Liepmann	Date

University of California, Berkeley

Spring 2001

Abstract

Articulated Mechanisms and Electrostatic Actuators for Autonomous Microrobots

by

Richard Yeh

Doctor of Philosophy in Electrical Engineering and Computer Science

University of California, Berkeley

Professor Kristofer S.J. Pister, Chair

Enabled by advances in both integrated circuit technology and micro electromechanical systems (MEMS), the continuing miniaturization and integration of electronics, sensors, actuators and mechanisms will make it feasible to create insect-sized autonomous microrobots. We propose to create a class of autonomous crawling microrobots the size on the order of $1cm^3$ and equipped with a power source, low-power CMOS controller, sensors, wireless communications devices and motorized articulated legs. The work presented here demonstrates how articulated insect legs could be created from rigid links, mechanical couplings and low-power electrostatic micromotors.

Articulated legs require rigid links to support the weight of the microrobot and also have joints that allow out-of-plane motion. Surface micromachined polysilicon hinges are utilized to satisfy both requirements. Rigid links are created by folding three hinged polysilicon plates into a hollow triangular beam which snap into place using snaplocks. These links can be fabricated in series with hinges as revolute joints. Two-link legs with up to three degrees-of-freedom (DOF) have been demonstrated.

Each link has a mechanical coupling that couples it to its own motor on-chip. Using hinged lever arms, hinged tendons and sliders, multi-DOF mechanical couplings can be created to convert linear motion at the motor to angular displacement at the joint. A 2-link, 2-DOF leg has been demonstrated with two mechanical couplings. The first mechanical coupling (with 1-DOF) is created from a four-bar linkage (sliding crank) and coupled to the first link. The second mechanical coupling (with 2-DOF) is created from a four-bar linkage in series with a five-bar linkage and coupled to the second link. Higher DOF mechanical couplings could be achieved with higher order *n*-bar linkages but at a cost of higher complexity.

The main considerations for actuation are output power density, efficiency, force density, and integration with the rest of the microrobot. Of the MEMS actuation technologies that have emerged over the years, electrostatic gap-closing actuators (GCA) in an inchworm motor topology is currently best suited for microrobots. Motors fabricated on silicon-on-insulator (SOI) wafers have been demonstrated with 80µm of travel, stepping rates of 1000 full steps/second corresponding to 4mm/s shuttle velocity, and ~260µN of force (~130 times its own weight). In all cases, displacement was limited by contact with a physical constraint (spring travel limits, nearby structures, etc.) rather than an intrinsic limit.

In addition to inchworm motors, mechanical digital-to-analog converters (DAC) have been demonstrated. These DAC’s convert a *n*-bit digital electrical input to an analog mechanical output (displacement) with 2^n position. Based on cascaded lever arms with high output resistance and gap-stop-limited actuator arrays at the input, the DAC are less sensitive to loading effects and input noise. These properties are ideal for possible open-

loop actuation of microrobots where joint angle feedback is difficult to implement. Four-bit DAC's with electrostatic actuators have been demonstrated in SOI technology with a least significant bit (LSB) of 0.6μm, an integrated non-linearity (INL) of ±0.38 LSB and a differential non-linearity of ±0.35 LSB. Surface micromachined 6-bit DAC's with hinged micromirrors have also been demonstrated with an LSB of 90nm, INL of ±3.2 LSB and a DNL of ±0.7 LSB.

Professor Kristofer S. J. Pister, Chair

Dedicated to my mother,

the memory of my father

and

the memory of my grandfather.

Grandfather Hsu, a self-taught engineer, standing next to machines he built during the Japanese occupation period in Taiwan.

Contents

List of Figures ... **v**

List of Tables ... **vii**

1 Introduction ... **1**
- 1.1 The Vision ... 1
- 1.2 Overview of the Dissertation ... 2
- 1.3 Previous Work ... 3
- 1.4 Concept ... 6
  - 1.4.1 Power ... 7
  - 1.4.2 Controller ... 8
  - 1.4.3 Articulated Legs and Mechanical Couplings ... 10
  - 1.4.4 Actuation ... 11
  - 1.4.5 Sensors ... 11
  - 1.4.6 Communication ... 12
  - 1.4.7 Gait ... 14

2 Articulated Mechanism ... **17**
- 2.1 Introduction ... 17
- 2.2 Legs or Wheels ... 17
- 2.3 Rigid Links ... 17
- 2.4 Stiffness ... 21
- 2.5 Articulated Joints and Multiple DOF ... 23
- 2.6 Mechanical Coupling ... 25

3 Actuation ... **31**
- 3.1 Introduction ... 31
- 3.2 Figures of merit ... 31
  - 3.2.1 Output Power Density ... 31
  - 3.2.2 Force density and force coefficient ... 32
  - 3.2.3 Efficiency ... 32

3.2.4 Integration 33
3.3 Comparison of Actuation Methods 33
3.3.1 Thermal Actuation 33
3.3.2 Magnetic Actuation 35
3.3.3 Piezoelectric actuation 36
3.3.4 Electrostatic Actuation 36
3.3.4.1 Efficiency of electrostatic actuators 37
3.3.4.2 Force density of electrostatic actuators 39
3.4 Comparison of Electrostatic Actuators 39
3.5 Gap-Closing Actuator Design 44
3.6 Static Model 46
3.6.1 Forces 46
3.6.2 Pull-in Voltage and pull-in gap 46
3.6.3 Failure Voltage 48
3.6.4 Force Density 49
3.7 Dynamic Model 50
3.8 Optimization 50
3.8.1 Initial gap (g) 51
3.8.2 Actuator stroke (g_s) 52
3.8.3 Electrode thickness (t) 52
3.8.4 Maximum voltage (V) 52
3.8.5 Electrode length (l) 52
3.8.6 Electrode width (w) 53
3.8.7 Unit cell separation (z) 53
3.8.8 Optimization for high force density 53
3.9 Fabrication 54
3.9.1 Polysilicon Process 54
3.9.2 Single Crytalline Silicon Process 56

4 Linear Electrostatic Inchworm Motors 59
4.1 Introduction 59
4.2 Design 61
4.2.1 Attachment Force 62
4.2.2 Pulling Force 63
4.2.3 Gear Teeth 64
4.2.4 Speed 64
4.2.5 Power 65
4.3 Scaling Effects 66
4.3.1 Actuator Force 66
4.3.2 Dissipative Forces 67
4.3.3 Output Power Density 67
4.4 Results 68

5 Mechanical Digital-To-Analog Converters 73

5.1 Introduction 73
5.2 Design 73
5.2.1 Input Noise Immunity and Resolution 77
5.2.2 Low loading effect and force magnification 78
5.2.3 Actuation 79
5.3 Results 80
5.3.1 Transfer Function 82
5.3.2 Nonlinearity 86
5.3.3 Maximum Resolution 89
5.3.4 Maximum Operating Frequency 89

6 System Integration 91
6.1 Introduction 91
6.2 Proposed Assembly Process 91
6.2.1 Proposed assembly process for legs and motors 93
6.2.2 Proposed assembly process for motorized legs and Smart Dust 97
6.3 Power 99

7 Conclusion 103
7.1 Summary of Results 103
7.2 Future research directions 105
7.2.1 Integration/Assembly 105
7.2.2 Optimization 106
7.2.3 Computer aided design 107

Appendix A: Matlab Code for Force Optimization 125

Appendix B: Single Mask Motor Process 129

List of Figures

Fig. 1-1. SEM of a six-legged microrobot (without motors) 1
Fig. 1-2. First microhinges. 3
Fig. 1-3. Photograph of microrobot actuated by a piezoelectric vibrator. 4
Fig. 1-4. A microrobot created from arrays of hinged thermal actuators. 5
Fig. 1-5. The first walking microrobot 5
Fig. 1-6. Concept of microrobot component. 7
Fig. 1-7. Photo of an in-house fabricated solar cell (left) and a MUMPs chip 8
Fig. 1-8. SEM of a preliminary Smart Dust circuit 9
Fig. 1-9. SEM of a 2-DOF robot leg. 10
Fig. 1-10. SEM of an electrostatic linear inchworm motor 11
Fig. 1-11. SEM of a corner cube reflector fabricated in MUMPs. 13
Fig. 1-12. Concept of the Steerable Agile Laser Transmitter (SALT) and receiver. ... 14
Fig. 1-13. A crawling microrobot with two legs. 15
Fig. 2-1. Two versions of microhinges. 18
Fig. 2-2. SEM picture of various surface micromachined components 18
Fig. 2-3. HTB's 19
Fig. 2-4. Two versions of snaplocks which fasten the HTB plates. 20
Fig. 2-5. HTB's rotated by 90o (foreground) with respect to the substrate. 20
Fig. 2-6. Loading test on four corner HTB's. 21
Fig. 2-7. Stop-motion pictures of HTB collapsing under a load. Top view shown... 21
Fig. 2-8. Pictures of the remains of four corner HTB's after collapse. 22
Fig. 2-9. Force being applied to both a flat beam and a hollow triangular beam. 22
Fig. 2-10. Multiple DOF links. 23
Fig. 2-11. (a) SEM of a 3-DOF leg with two links fabricated in the MUMPs process. 24
Fig. 2-12. Test procedure of scissor hinges. 25
Fig. 2-13. SEM of a slider crank 26
Fig. 2-14. Diagram of a slider crank coupled to a five-bar linkage. 27
Fig. 2-15. Mechanical coupling for 2-link structure. 28
Fig. 2-16. 2-DOF legs and mechanical coupling. 29
Fig. 3-1. Circuit model for adiabatic charging 38
Fig. 3-2. A plot of the Paschen Curve 39
Fig. 3-3. Diagram of a gap-closing actuator. 40
Fig. 3-3. Plot of force vs. electrode position 40
Fig. 3-4. Diagram of a comb-drive actuator. 42
Fig. 3-5. The scratch-drive actuator (SDA). 43
Fig. 3-6. Different gap-closing actuator topologies. 44
Fig. 3-7. An array of two gap-closing actuators. 45

Fig. 3-8. Total energy of the GCA system 47
Fig. 3-9. Maximum voltage 48
Fig. 3-10. Four SEM photos of a DRIE etched SOI sidewall. 51
Fig. 3-11. Output of GCA optimizer. 55
Fig. 3-12. SEM of a gap-closing actuator array 56
Fig. 3-13. Single-Mask fabrication process. 57
Fig. 3-14. SEM of a gap-closing actuator 57
Fig. 4-1. A log-log plot of the force densities 60
Fig. 4-2. Examples of various inchworm motor layouts. 61
Fig. 4-3. Diagram of an inchworm cycle for motor configuration in Fig. 4-2a. 62
Fig. 4-4. Timing diagram for the inchworm motor through one cycle. 65
Fig. 4-5. (a) SEM of an inchworm motor fabricated on an SOI wafer. 69
Fig. 4-6. Measured force vs. pull-in voltage 71
Fig. 5-1. The DAC concept. 74
Fig. 5-2. (a) An electrical implementation of the DAC 74
Fig. 5-3. A mechanical implementation of the DAC 75
Fig. 5-4. A MEMS implementation of the DAC 75
Fig. 5-5. Example of a 2-bit DAC created by cascading two lever arm stages. 76
Fig. 5-6. Low loading effect of DAC's 78
Fig. 5-7. Diagram of a DAC using thermal actuators. 79
Fig. 5-8. Diagram of a DAC using electrostatic gap-closing actuators. 79
Fig. 5-9. SEM picture of a lever arm 80
Fig. 5-10. SEM picture of four cascaded lever arms 81
Fig. 5-11. SEM of 4-bit DAC with electrostatic gap-closing actuator arrays. 82
Fig. 5-12. DAC-driven mirrors. 83
Fig. 5-13. Diagram of the optical method of characterization. 84
Fig. 5-14. Output beam position of the 6-bit DAC. 84
Fig. 5-15. Output beam position of the 6-bit DAC through 19 cycles. 85
Fig. 5-15. The average beam position of each output state 85
Fig. 5-16. The standard deviation of the beam positions 86
Fig. 5-17. Output of 4-bit electrostatically-driven DAC. 87
Fig. 5-18. SEM of STS etched silicon 87
Fig. 5-19. Nonlinearity 88
Fig. 5-20. Step Response of 4-bit DAC/mirror. 90
Fig. 6-1. System diagram. 92
Fig. 6-2. Gold bump flip-chip process flow. (From Maharbiz [58]). 93
Fig. 6-3. Proposed method of connecting SOI motors 94
Fig. 6-4. Proposed assembly process 95
Fig. 6-5. SEM of a polysilicon serpentine beam 96
Fig. 6-6. Proposed process for assembly 97
Fig. 6-7. SEM of a $138mm^3$ Smart Dust node 98
Fig. 6-8. Concept of microrobot component. 99

List of Tables

Table 3-1: Input 53
Table 3-2: Optimized Output 54
Table 4-1: Scaling Effects 68
Table 6-1: Processes used for current Components 92
Table 6-1: Initial Design for a six-Legged Microrobot 100

Acknowledgements

No man is an island and this is certainly true in graduate school. I owe many thanks to all the students and professors whom I interacted with at UCLA and the Berkeley Sensor and Actuator Center (BSAC). I will attempt to acknowledge them all here but for those whom I inadvertently miss, I humbly issue a heartfelt thanks.

I thank my original research group from UCLA for making my early and formidable years in graduate school a memorable one. Gisela Lin provided the leadership that held the group together and gave the group an identity. Mike Klitzke entertained us with invitations to his rock concerts. Beverly Eyre, Roger Lo, Devi Gunawan, Patrick Chu, Floy Chang, Win Li and Jack Shih provided great company and discussion. I also thank Zeke Kruglick for being the first graduate student from our UCLA group to move to BSAC and did most of the work in establishing our lab space in Cory Hall.

I thank Jim Bustillo, Amy Wang, Audra Meng, Michael Helmbrecht, Dubravka Bilic, Cliff Knollenberg, Lilac Muller and many others for qualifying me on equipment and procedures in BSAC and the microlab. Brett Warneke, Veljko Milanovic, Matt Last, Brian Atwood and Justin Black were colleagues that often kept me company on late night stays in lab. In addition to the late-night crew, Brian Leibowitz, Ningning Zhou, Thara Srinivasan, Jocelyn Nee, Rob Conant, Michel Maharbiz, Joe Seeger and Chris Keller always offered valuable advice on research. James McLurkin, Dana Teasdale and Lance Doherty were labmates not only did good research but also helped the group chemistry. Special thanks go to Joe for hours of coaching when I practiced for the qualifying examination and to Seth Hollar for being a great research partner and for teaching me the card game "bull." Also, Dr. Ron Wilson and the late Dr. Richard Lysee patiently provided beautiful SEM photos of my work

Of course, BSAC'ers work hard and play hard. Whether it'd be a football game, a basketball game, a foosball game or a BIG GAME, you're sure to find some BSAC'ers there. I thank Carl Chang, Patrick Riehl, Sharon Oh, Cliff Knollenberg, Michael Helmbrecht, Elliot Hui, Hyuck Choo, Wesley Chang, Jodie Nakamura and many others for the company. Go Bears!

On the spiritual side, I thank my brother, Frank, for introducing me to Tzu Chi, a Buddhist community service group. There I met an excellent group of fellow students who were willing to give time to do community service and learn Buddhism at the same time. I thank the Chiu sisters, Anny Sun, Frank Lin, Dave Lee, Szuyin Chen, Sandi Zee, Nelson Su, Rose Chen, Howard Huang, Ting-Wei Chang, Peggy Lo, Lissa "Metta" Shih, Wendy Hsu and many others for helping me grow spiritually. I also thank Rev. Heng Sure, Dr. Martin Verhoeven and Doug Powers for all the Dharma and meditation lessons they taught.

I thank my advisor Prof. Kristofer Pister whom I have known since his last year in graduate school and whom got me involved in MEMS research. I also thank my quals and dissertation committee members Profs. Roger Howe, Dorian Liepmann and Richard White for their valuable advice and time. I am grateful to Prof. Richard Muller for giving me the very first issue of the Journal of Microelectromechanical Systems in my undergraduate senior year and got me interested in MEMS.

Finally, I thank my family for always being there and providing a source of strength for me through the thick and thin. I can never repay my parents, Tony and Julie Yeh, for the sacrifices they made 22 years ago when they traded their comfortable lifestyles and high-paying careers in Taiwan for the string of tiring jobs of flipping burgers, selling newspapers, and selling socks at swap meets in the hot LA sun. All that so Frank and I could get a better education.

CHAPTER 1. INTRODUCTION

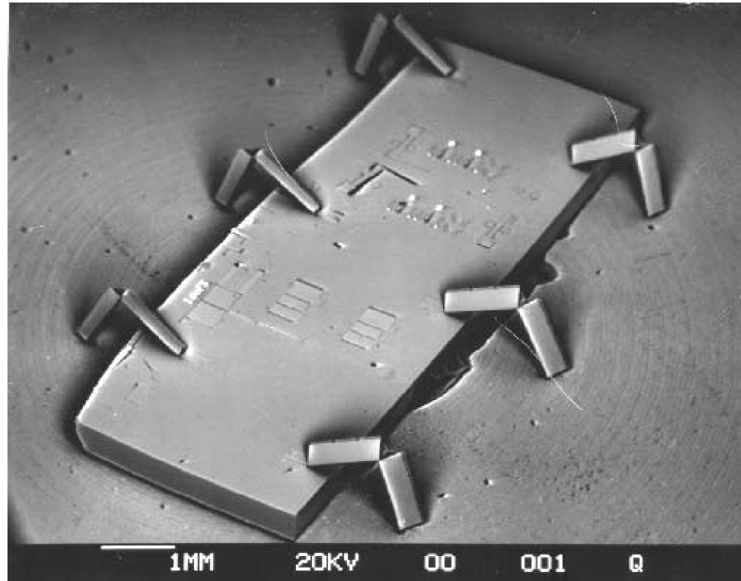

Fig. 1-1. SEM of a six-legged microrobot (without motors) fabricated in the commercial MUMPs process.

1.1 The Vision

Microrobotics has always been one of the aspirations of micromachining. In fact, the first micromachining workshop was sponsored by the IEEE Robotics and Automation Society in 1987 [69]. In 1959, Dr. Richard Feynman challenged an audience of physicists at the American Physical Society Annual Meeting to explore the vast microscopic world through miniaturization [27]. Today, integrated circuit (IC) technology and micromachining are the best tools available for miniaturization. The capability of integrating sensors and actuators with ever-shrinking electronics leads to the tantalizing possibility of creating insect-sized autonomous microrobots with a power source, sensors, a controller, wireless

communications devices, actuators and articulated legs. These microrobots could communicate with each other or with a base station. A swarm of robots equipped with infrared thermal sensors could crawl into earthquake rubble to search for survivors or a squadron of robots with CMOS imagers could crawl into insect hives and collect data about insect behavior.

1.2 Overview of the Dissertation

Today, microrobots still have a long ways to go before they are at the stage where conventional-sized robots are. One difficulty of building microrobots is that, unlike building conventional robots, micro-sized off-the-shelf components are not readily available. The contribution of this work is closing that gap by creating a set of components that are appropriate for a microrobot *system*. To that point, a method for creating articulated microrobot legs with multiple degrees-of-freedom and mechanical couplings is developed. To actuate the legs, low-power micromotors with a high force density and high efficiency were created. Also because joint angle feedback is difficult to attain for microrobots, a mechanical digital-to-analog converter was demonstrated to explore a technique for open-loop actuation. This work, in conjunction with the Smart Dust Project [85], is the first systems-level approach at building an autonomous microrobot with an architecture for power, sensing, control, wireless communications and mobility. As the microrobotic field matures, future work is likely to address the issues of integration, optimization, controls and the interaction of multiple microrobots.

We begin in Chapter 1 by reviewing related work from the last decade and describing a new class of MEMS articulated microrobots. In Chapter 2, methods for creating multi-DOF articulated mechanisms and results are reported. Low-power electrostatic gap-

closing actuators are described in Chapter 3. To overcome the force-displacement trade-off of electrostatic gap-closing actuators, a large force, large displacement, electrostatic linear inchworm motor with high efficiency is described in chapter 4 along with results. Following that, a novel mechanical digital-to-analog converter is reported in chapter 5. Finally, Chapter 6 proposes a method to integrate these components.

1.3 Previous Work

One of the challenges of creating microrobots in micromachining is making 3-dimensional structures from an inherently 2-dimensional process. A solution to this problem was introduced in 1992 when Pister *et al.* [68] demonstrated a pin-in-slot microhinge (Fig. a) and Suzuki *et al.* [79] demonstrated a flexural microhinge (Fig. b). These hinges

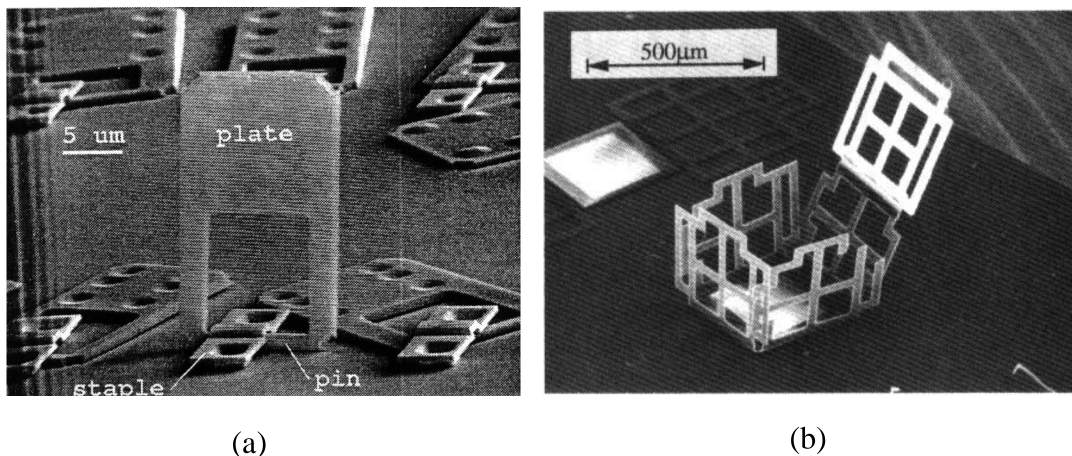

(a) (b)

Fig. 1-2. First microhinges. (a) An array of polysilicon plates with rotational hinges. Anti-stiction dimples can be seen on some plates. (From Pister [68]). (b) A 3-dimensional structure with polysilicon frames and flexural polyimide hinges. (From Suzuki [79]).

allow planar microstructures to be folded into 3-dimensional shapes. Suzuki *et al.* proposed folding hinged silicon plates to form an insect exoskeleton [79]. Yasuda et al. used these polyimide hinges to create a microrobot which moves on a piezoelectric vibrator.

The microrobot has two moving polysilicon legs created by a beam-supported plate (Fig. 1-3). The supporting beams have different lengths for each leg resulting in unique reso-

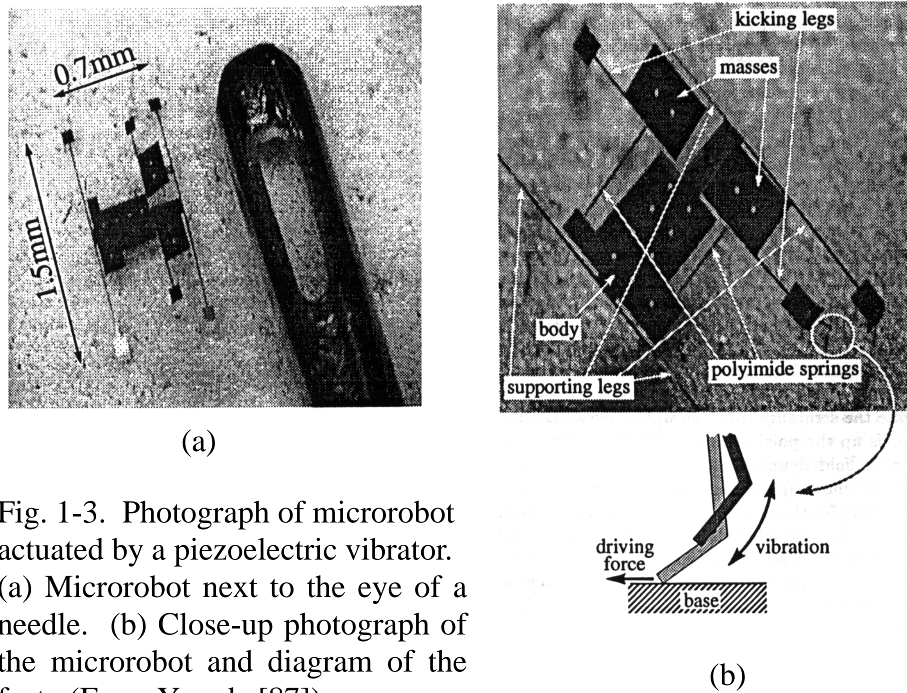

(a)

(b)

Fig. 1-3. Photograph of microrobot actuated by a piezoelectric vibrator. (a) Microrobot next to the eye of a needle. (b) Close-up photograph of the microrobot and diagram of the feet. (From Yasuda [87]).

nant frequencies for each leg. This allows the legs to be addressed independently by the frequency of the piezoelectric vibrator. The legs have feet with polyimide "ankles." When a leg vibrates, its foot scratches forward on the contact surface.

Though this was a good demonstration of MEMS microrobotics, it required an off-chip piezoelectric vibrator to provide the power source, actuation, and control which limited the robot workspace to the vibrator area. As microrobotics matured, micro-sized actuators were integrated into the design. One of these designs, proposed by Kladitis et al. [45], is based on a popular thermal actuator originally invented by Guckel et al. in the

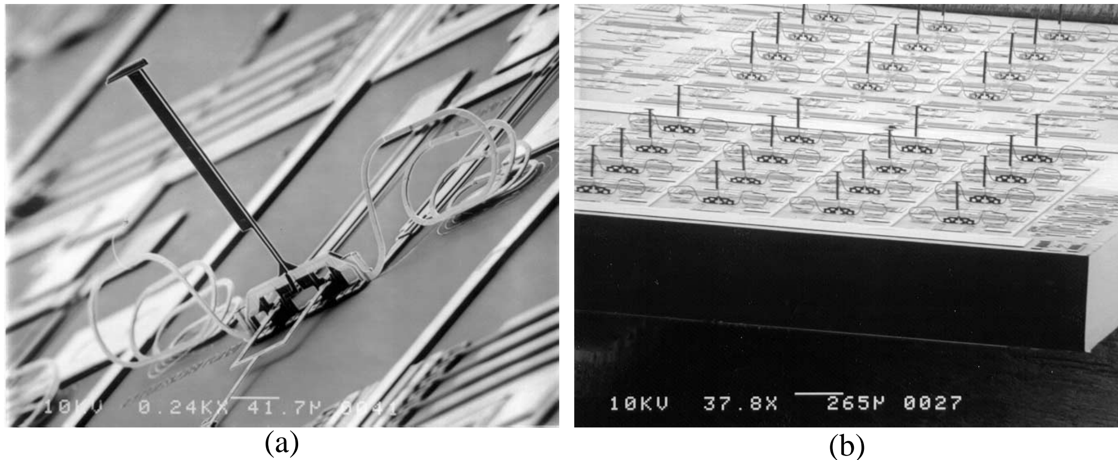

Fig. 1-4. A microrobot created from arrays of hinged thermal actuators. (a) Close-up SEM of a 2-DOF hinged thermal actuator rotated out of the plane of the substrate. (b) SEM of arrays of 16 such actuators. (From Kladitis [45]).

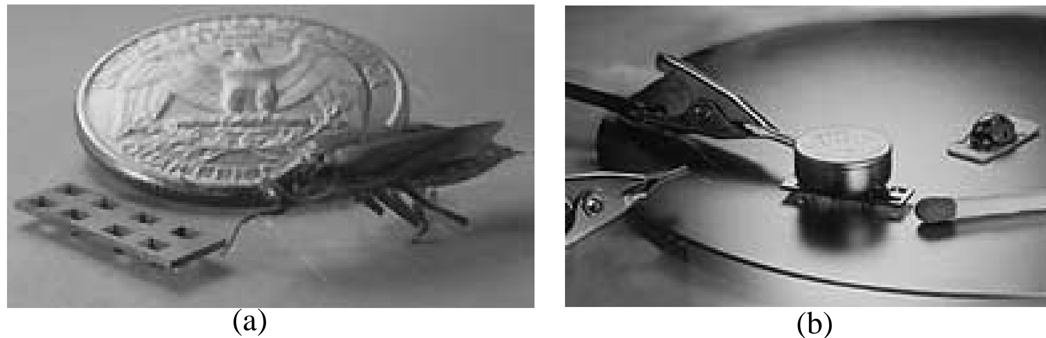

Fig. 1-5. The first walking microrobot made from polyimide thermal actuators (From Ebefors [24]).

LIGA process [36] and later popularized by Comtois et al. in the commercial MUMPs[1] process [21]. Pister-style hinges are used to enable arrays of thermal actuators to rotate 90° out of plane of the substrate (Fig. 1-4). These actuators serve as the microrobot legs. Another design is the first walking MEMS microrobot by Ebefors et al. [24]. This microrobot has two arrays of four legs each. Each leg has one degree-of-freedom (DOF)

[1] Multi-User MEMS Projects (MUMPs) is a commercial MEMS polysilicon process with one electrical layer, two polysilicon layers and a metal layer. See http://www.memsrus.com/cronos/svcsmumps.html.

and thermally actuated by polyimide joints (Fig. 1-5). This design is very robust because the legs are made from ~30μm-thick slabs of single crystalline silicon and the monolithic actuators work by thermal expansion and thus has no moving parts or mechanical couplings. Both thermal-actuator designs require from tens to hundreds of milliwatts to operate and has a very low power efficiency (power out divided by power in).

These robot designs demonstrate MEMS as a potential technology for building microrobots. To realize an autonomous microrobot, we propose a systems level approach which considers power, actuation, sensing, communications, controls and integration of these components into a microrobot.

1.4 Concept

To achieve our goal, there are two projects working in parallel. The first project, described in this dissertation, is the creation of microrobot legs and actuators [90-94]. The second project, called Smart Dust [85], aims to exploit silicon device miniaturization by packing autonomous computing, sensing, communicating, and energy-storage devices into a 1mm^3 volume. Such nodes form the building block of massive distributed sensor networks that can provide more information in a less intrusive way than current methods. Autonomous microrobots can be thought of as Smart Dust with legs.

Fig. 1-6 shows our microrobot concept. The minimum set of components required to make silicon walk on its own are a power source, controller, actuators and legs. Additionally, sensors and communications devices would improve the functionality of microrobot.

1.4.1. Power

Solar cells will be used as a power source for the microrobot. Solar cells can be scaled in size more easily than current battery technologies and it is compatible with silicon fabrication processes that allow it to be integrated more easily into a MEMS microrobot. In addition, solar radiation is a good source of power. Full sunlight (air mass 1) has a power density of 1mW/mm^2 and room lighting has 1-10μW/mm^2. The conversion efficiency limit of silicon solar cells is around 21% [57] and in-house fabrication of solar cells [9] has yielded up to 15%. A 1cm^2 solar array with a modest 10% conversion efficiency will generate 10mW of power for the microrobot. Fig. 1-7 shows a picture of an in-house fabricated solar cell next to a MUMPs chip with robot legs. In addition, power from solar cells can be used to trickle-charge a capacitor or battery. The stored energy can then be used at a much higher rate than the charging power [5].

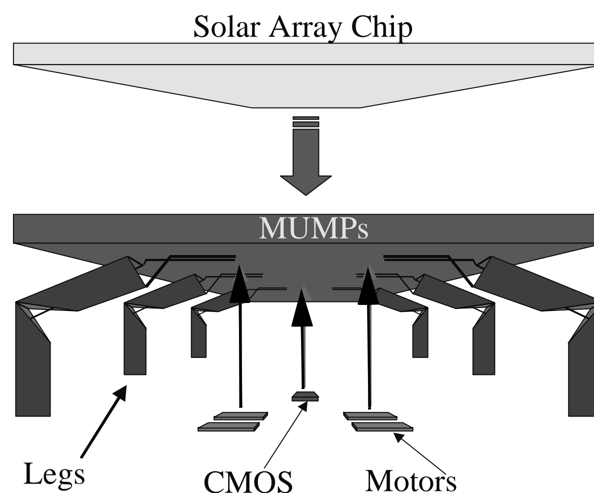

Fig. 1-6. Concept of microrobot component. The robot consists of six 2-DOF legs, motors for every link of each leg, a CMOS controller, and a solar array chip.

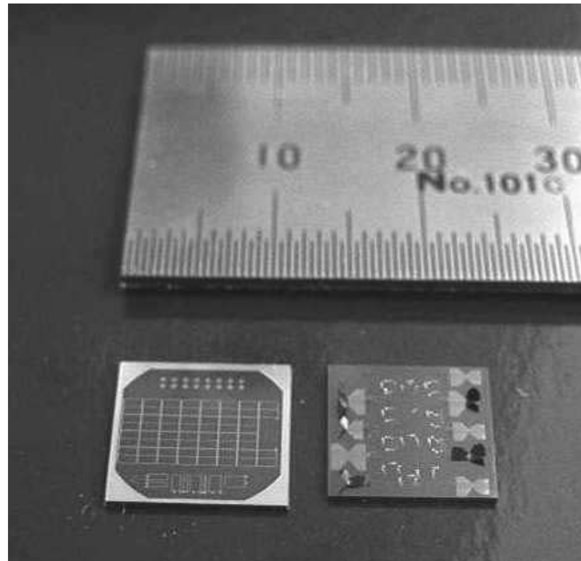

Fig. 1-7. Photo of an in-house fabricated solar cell (left) and a MUMPs chip with microrobot legs (right). There are legs that are not assembled, partially assembled and fully assembled. Solar cell by Colby Bellew [9].

1.4.2. Controller

Low-power CMOS controllers from the Smart Dust Project [85] will be used to coordinate the robot locomotion. A finite-state machine could be implemented where each state describes the discretized end-point positions of each leg and the output of each state would be the corresponding control signals. The control signals are amplified by 30V transistors (fabricated by the in-house solar cell process [9]) to control the motors.

A preliminary Smart Dust controller is shown in Fig. 1-8. The controller was fabricated in the National Semiconductors 0.25µm CMOS process and has a photodiode, pseudo-random sequence generator and charge pump. This circuit is designed to consume only 17µW of power.

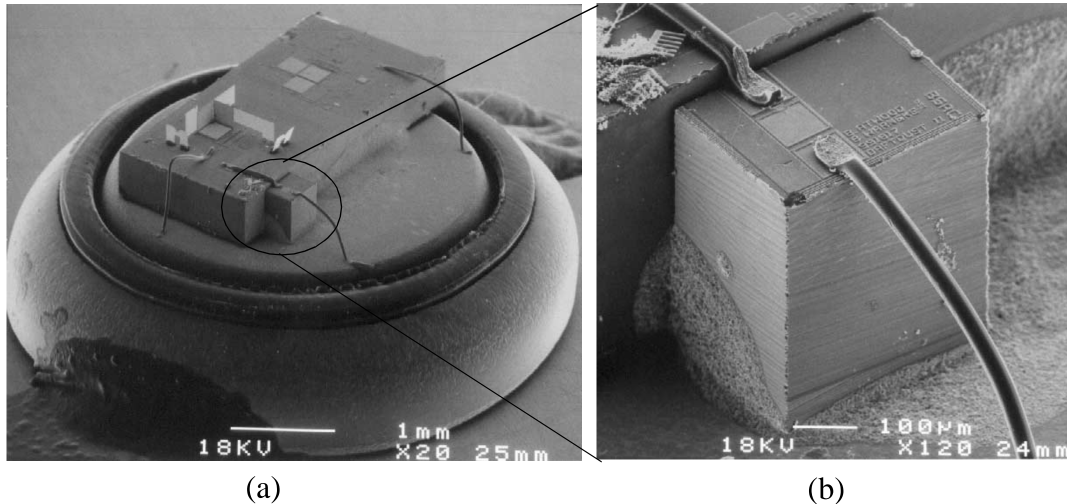

(a) (b)

Fig. 1-8. SEM of a preliminary Smart Dust circuit designed to control an optical communications device (Corner Cube Reflector). (a) The Smart Dust node with a hearing aid battery. (b) Close-up of the CMOS controller. (From Warneke [85]).

1.4.3. Articulated Legs and Mechanical Couplings

The microrobot will have articulated legs such as the ones shown in Fig. 1-1. Technique has been developed to create legs with multiple degrees-of-freedom (DOF). Pister-style hinges enable polysilicon films to be folded into rigid shapes used as robot links and hinges also are used as revolute joints to achieve articulation. Using this technique, a new class of articulated structures can be realized. Microrobots could be outfitted with varying DOF-legs and link sizes. Fig. 1-9 shows an example of a leg design with 2 DOF having parallel axis of rotation. Each link has mechanical couplings that are to be integrated with motors on the substrate. The mechanical couplings are created from a combination of hinges, lever arms, and polysilicon "tendons."

1.4.4. Actuation

Actuators are one of the toughest components to build. The requirements are low-power consumption, high efficiency and compatibility with the leg components. Cur-

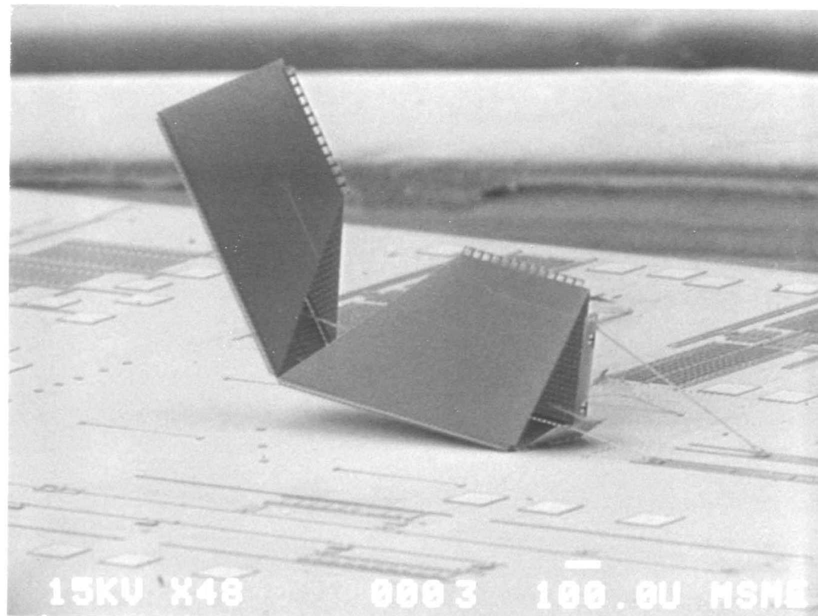

Fig. 1-9. SEM of a 2-DOF robot leg. The axis of rotations are parallel. The legs also have mechanical couplings coupling each link to sliding shuttles on the substrate.

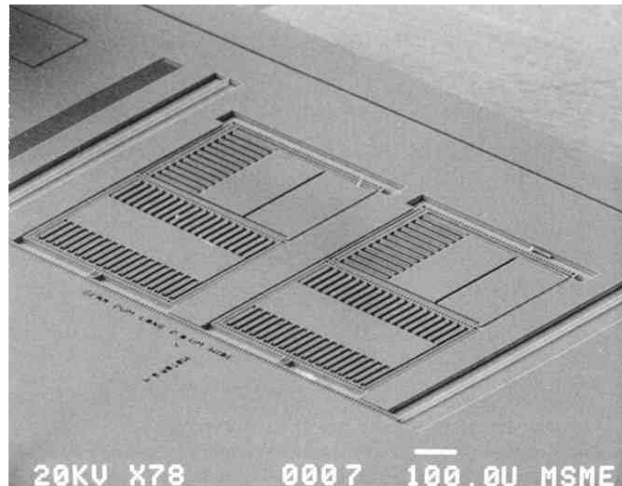

Fig. 1-10. SEM of an electrostatic linear inchworm motor fabricated in-house using a deep reactive ion etch Bosch Process. These motors can produce hundreds of microNewtons with moderate voltages and high power efficiency.

rently, the best actuator for autonomous microrobots is the electrostatic linear inchworm motor described in Chapter 4 (Fig. 1-10). These motors can produce hundreds of μN of force using moderate voltages and have efficiency of tens of percent, which is orders of

magnitude higher than the efficiency of other motors with comparable force densities. In addition, these inchworm motors scale favorably in the microscale and are fabricated in a silicon process for better compatibility with the leg components. As described in Chapter 4, a motor with 1mN of usable force operating at 1kHz would consume ~27μW of power.

1.4.5. Sensors

Future microrobots would gather environmental information through micro-sized sensors. Among the micro-sized sensors available today are accelerometers, magnetometers, temperature sensors, microphones, light sensors, hygrometers, and chemical/gas sensors. These sensors could enable microrobots to gather data in hostile environments or implement path planning such as object avoidance, finding heat sources, finding the brightest light sources in an area, etc. For the controller to interface with most sensors, supporting components such as amplifiers and analog-to-digital converters (ADC) would be required. Power consumption of sensors, amplifiers, and ADC's have been considered in [23]. Power consumption depends on the resolution required. From [23], the energy per sample for a 1V-supply voltage and 10-bit accuracy is ~1μJ for an input resolution of ΔV=1μV (typical for acceleration transducers) and 1pJ for ΔV=1mV (typical for temperature transducers). The ADXL202, a commercial two-axis accelerometer by Analog Devices, dissipates 800μW per axis from a 2.7V supply. From [23], the amplifier would consume ~27μW and the analog-to-digital conversion would cost ~1nJ per sample for an 8-10 bit sample.

1.4.6. Communication

In addition to sensing, future microrobots would also be able to communicate with other microrobots or with a base station. Since data can be transmitted at a low rate to accommodate power restrictions, the key figure of merit is the *energy per bit* of data transmitted or received. Low-power communications for autonomous sensing nodes is one of the research thrusts of Smart Dust and the results would be integrated into the microrobot.

The early Smart Dust nodes employed passive optical communications through the use of MEMS corner cube reflectors (CCR) [85] (Fig. 1-11). Light incident on the CCR is reflected back in the same angle. A MEMS CCR has actuated base plate which could break the orthogonality of the cube and change the reflection angle [16, 37, 40]. Using this technique, an on-off-modulated signal could be transmitted from the node. This system requires an interrogator with a laser source and an optical receiver while the node transmits data with the CCR. Because the CCR is actuated electrostatically, the energy cost of transmission is only ~100pJ/bit but line-of-sight is required. The communications range depends on the laser intensity but is expected to be ~100 meters [5].

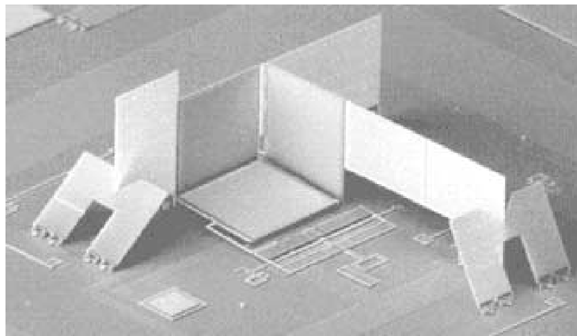

Fig. 1-11. SEM of a corner cube reflector fabricated in MUMPs. The base plate can be electrostatically actuated to modulate the reflection angle. (From Hsu [40]).

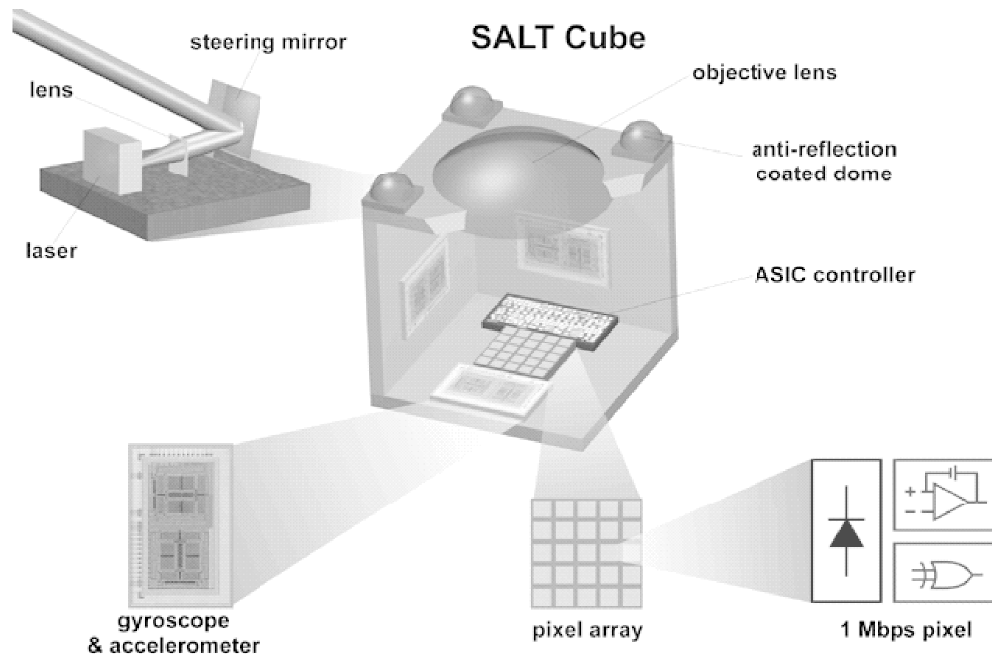

Fig. 1-12. Concept of the Steerable Agile Laser Transmitter (SALT) and receiver. In a volume of less than one cubic centimeter, the SALT cube would contain a steerable laser source, optical lens, CMOS imaging receiver, low-power controller and sensors. Courtesy of Matthew Last, Brian Leibowitz, and Gabe Matus [53].

The next generation of Smart Dust will have active optical communications by a steerable laser beam [60] and a low-power CMOS imaging receiver that is capable of receiving data at a rate of 2.5Mbps [53] (Fig. 1-12). This system should improve the capability of peer-to-peer communication due to beam steering. In addition, higher signal-to-noise ratio from the CMOS imaging receiver would increase the range of communications to the order of 1km. The power consumption of the image receiver is ~50µW/pixel so the energy cost for receiving is ~50µW/2.5Mbps = 20pJ/bit per pixel. The energy cost of transmission is 10mW with a range of ~1km. In comparison, RF communications requires ~100nJ/bit in the 2.4GHz band with a range on the order of 10 meters.

1.4.7. Gait

An articulated microrobot can have several gaits depending on the configuration of legs and leg designs. The larger number of DOF, the more agile the robot will be. However, the legs would be more difficult to build. The number of links are related to the number of DOF and the type of joint. If each joint on a leg has one degree of freedom, then the number of links equals the number of DOF. The most basic microrobot would have two 2-DOF legs. This allows for a crawling gait (Fig. 1-13). If both legs move synchronously, then the robot moves straight. If one of the legs move while the other stays stationary, then the robot turns toward the side with the stationary leg.

The two-legged robot described above will have to overcome the friction of the dragging body. In addition, the legs will need to have a greater contact friction with the crawling surface than the body's contact friction in order to crawl forward. One way to

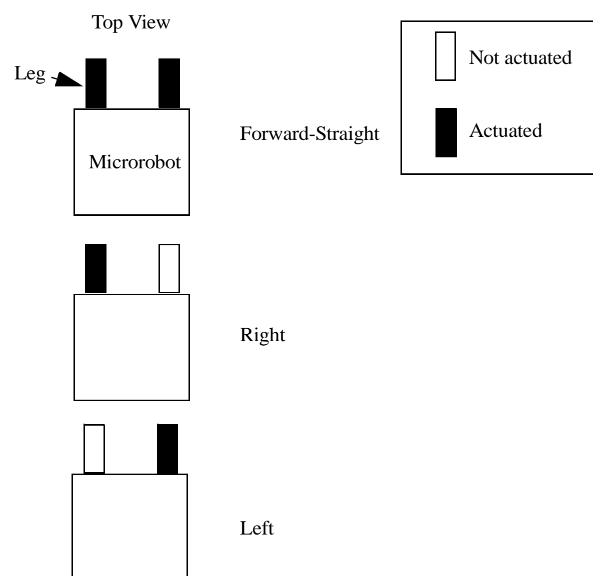

Fig. 1-13. A crawling microrobot with two legs. To go straight, both legs are moving synchronously. To turn left, the right leg moves while the left leg remains stationary. Vice versa to turn right.

achieve this is to design the body to have a smaller contact area. To avoid the friction involved in dragging the robot along a surface, the robot can be designed with six legs. Such a robot would use a double tripod gait for static stability. This gait achieve static stability by moving three legs at a time while another set of three are stationary and supporting the body. This stability comes at a cost of greater complexity and required yield as the robot would need at least 12 motors for six 2-dof legs. The robot would also require a larger volume and weigh more. A robot with a lower power requirement could have three actuated legs and three non-actuated legs. The three actuated legs move in synchrony just like in the previous example. The three non-actuatored legs only serve to support the weight of the body between the forward phases of the locomotion. They could be simple legs with one DOF for assembly into a 90 degree position. Once in position, the legs could be locked into this position using latch mechanisms [68]. This microrobot would require only six motors for three 2-dof legs. The following Chapter describes how such legs are built.

CHAPTER 2. ARTICULATED MECHANISM

2.1 Introduction

Unlike macro-sized robots where components are readily available off-the-shelf, all the components of a micro robot have to be designed and built. Whereas macro robot designers concentrate on controls and optimization, a micro robot designer has to first consider how the mechanisms can be fabricated before optimization. In this chapter, we will describe the techniques used to create the mechanism.

2.2 Legs or Wheels

Although mini-robots use wheeled locomotion, microrobots typically use legged locomotion because fabrication and assembly of wheels on the microscale is problematic. In addition, micro wheels would suffer from friction in the axel. Instead of wheels, microrobots are designed with legs and articulated joints, similar to insects, natures' "microrobots." In 1992, Suzuki et al., introduced the concept of creating insect-like microrobots with exoskeletons made from polysilicon plates and flexible polyimide joints [79]. We continue in that direction by proposing a class of articulated microrobots using hollow triangular beams (HTB's) as links, microhinges (Fig. 2-1) [93] as revolute joints, and linear electrostatic stepper motors for actuation [91]. Figure 2-2 shows a SEM photo of the micromachined components that can be used to create an articulated microrobot. All the components in this chapter are fabricated from the commercial MUMPs process unless otherwise indicated.

2.3 Rigid Links

A surface micromachined link, made from thin film polysilicon, must be rigid and strong enough to at least support the weight of the microrobot. HTB's have been designed

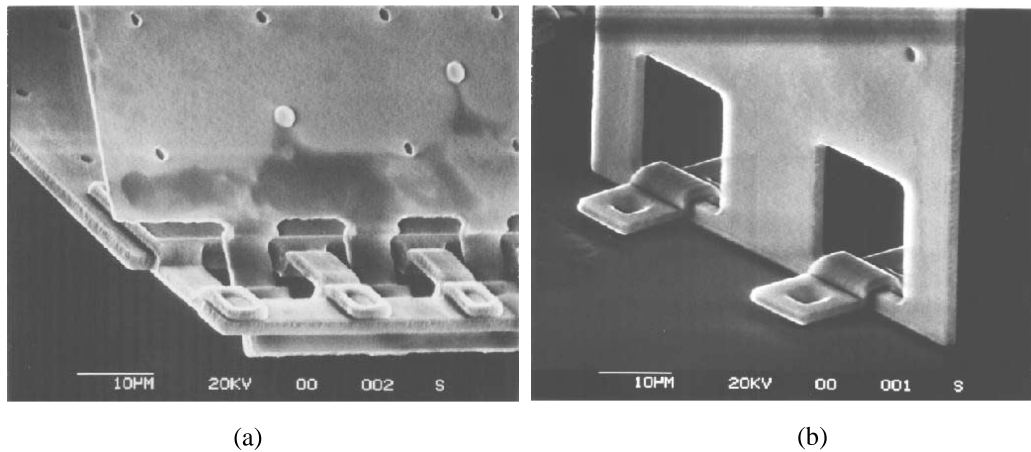

(a) (b)

Fig. 2-1. Two versions of microhinges. (a) Scissor hinges allow two released structures to rotate with respect to each other. (b) Substrate hinges allow a released structure to rotate out of the plane of the substrate.

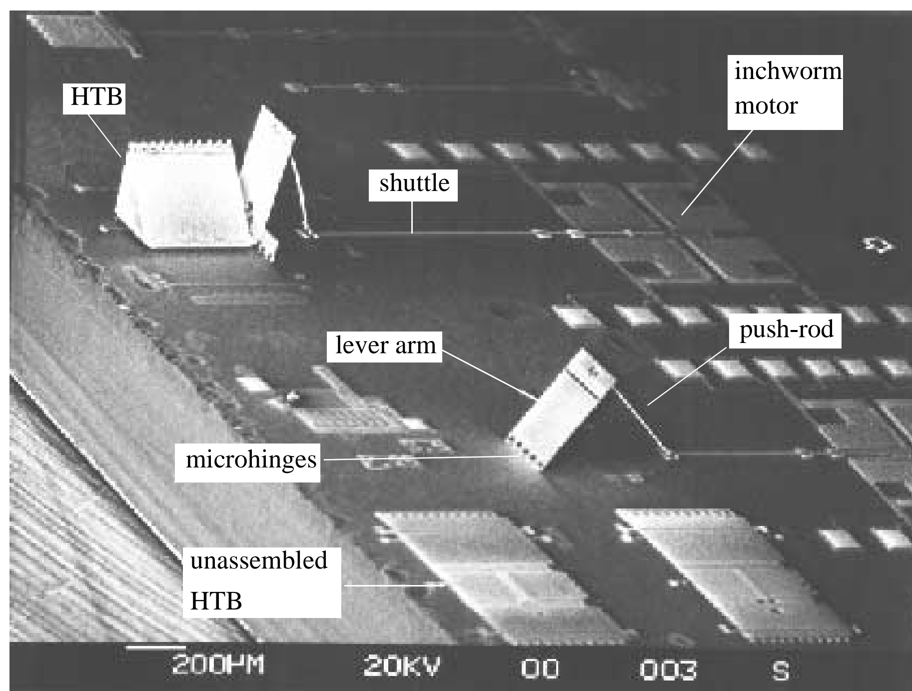

Fig. 2-2. SEM picture of various surface micromachined components for articulated microrobots. Included are inchworm motors, mechanical couplings, and rigid links.

and tested to satisfy these conditions. Figure 2-3a shows the CAD layout of one version of an HTB. The HTB is designed with three plates connected with scissor hinges (Fig. 2-1a), which allow two plates to rotate with respect to one another. The hinged plates are

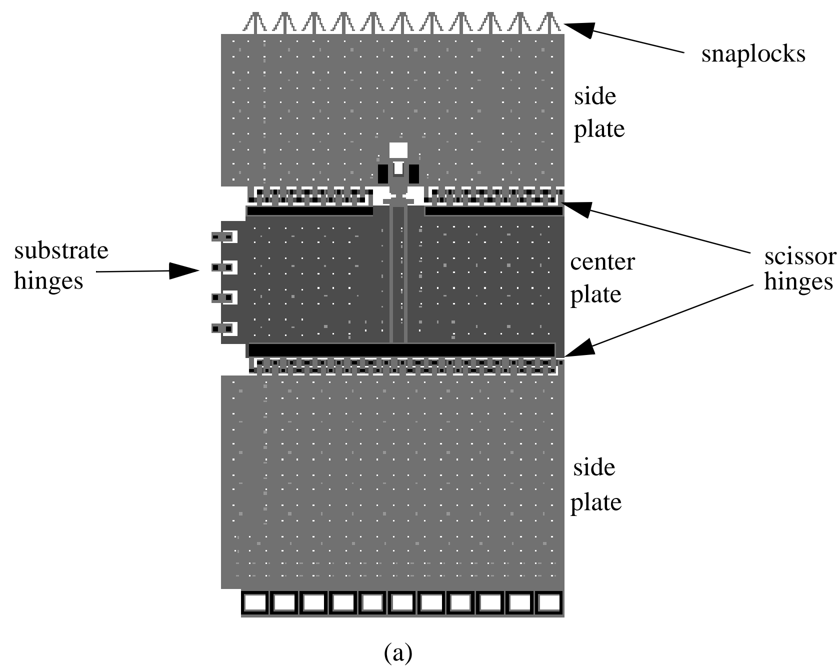

(a)

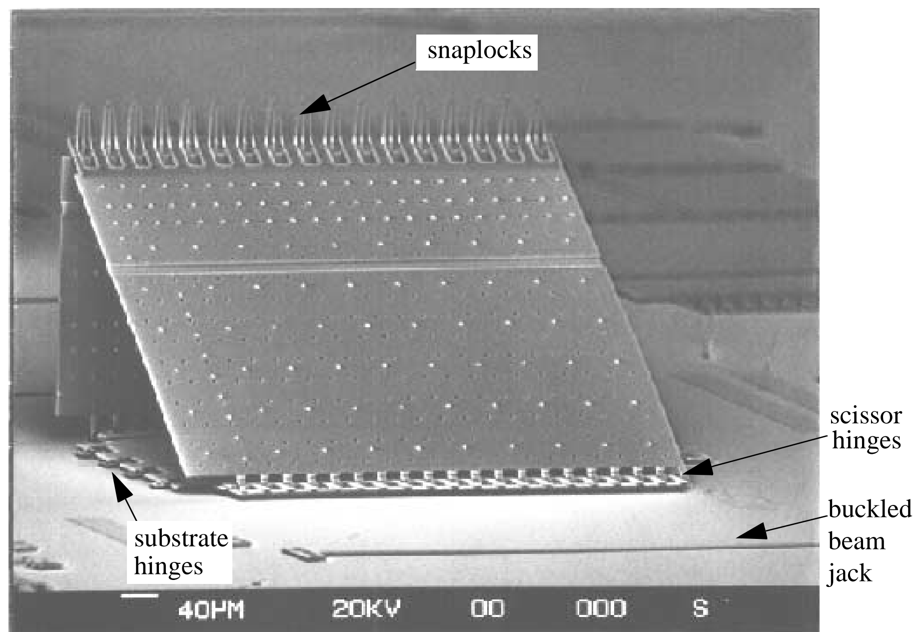

(b)

Fig. 2-3. HTB's. (a) CAD layout of an HTB with scissor hinges, substrate hinges, snaplocks, center plate, and side plates. This version has a right triangular cross-section. (b) SEM picture of an HTB. A buckled beam jack [18] is used as an assembly aid.

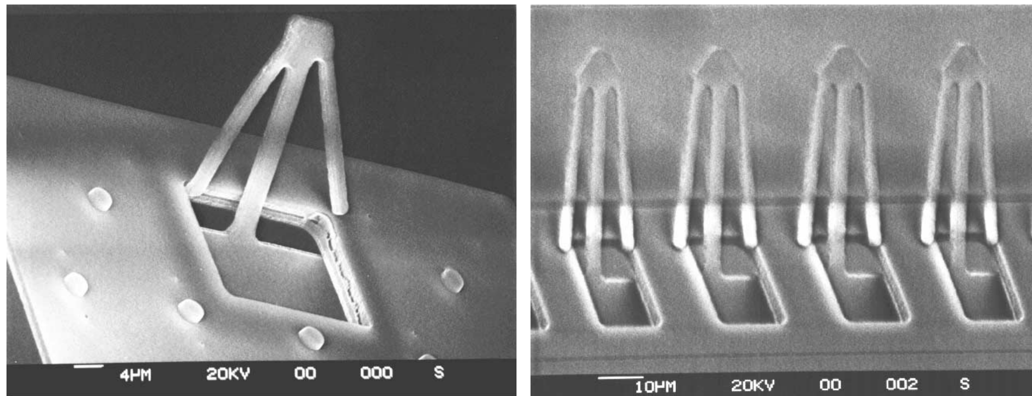

Fig. 2-4. Two versions of snaplocks which fasten the HTB plates.

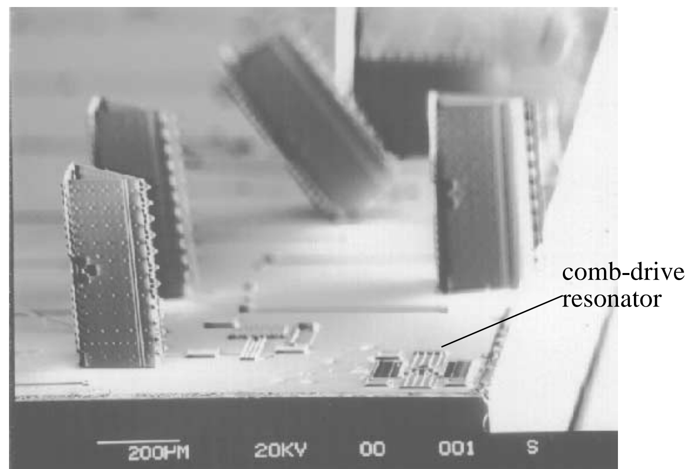

Fig. 2-5. HTB's rotated by 90° (foreground) with respect to the substrate. A comb-drive resonator is located at the lower right corner of the picture for size comparison.

assembled at a probe station using tri-axial micromanipulators with probe tips. The two side plates are folded up and over the center plate, creating a hollow triangular beam. The two side plates have snaplocks (Fig. 2-4) along the top edges to fasten the hinged plates in position after rotation into the desired angle. Figure 2-3b shows a SEM picture of an assembled HTB with substrate hinges (Fig. 2-1b) that allow the HTB to be rotated off of the substrate. This HTB has a right-triangular cross-section. Figure 2-5 shows HTB's that have been rotated out of the plane of the substrate after assembly.

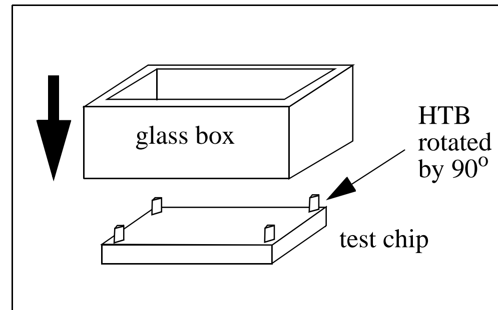

Fig. 2-6. Loading test on four corner HTB's.

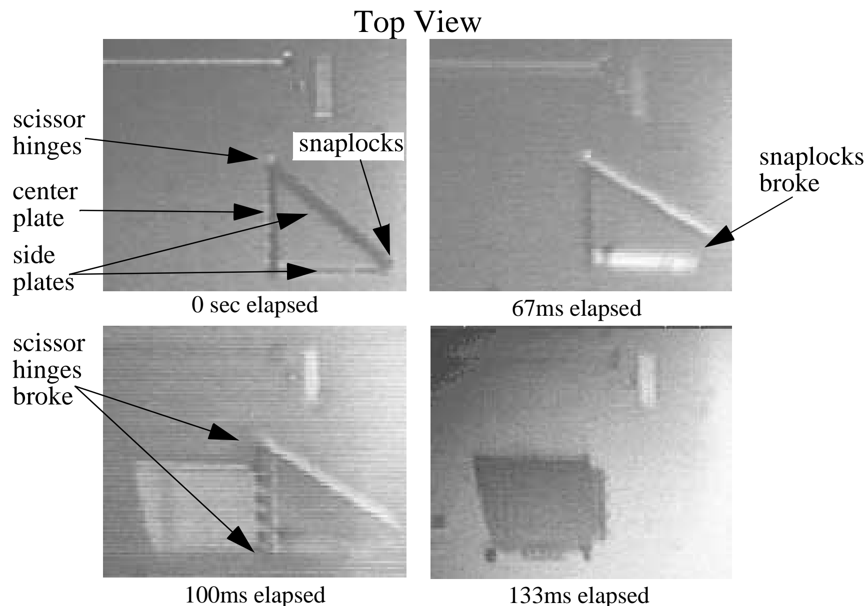

Fig. 2-7. Stop-motion pictures of HTB collapsing under a load.

2.4 Stiffness

To find the strength of HTB's in the axial direction, a glass box was placed on top of four 432μm tall, rotated HTB's (Fig. 2-6). A loaded HTB was viewed and video-recorded from the top view through the glass box with a microscope and TV/VCR setup. Water was then injected slowly from a syringe into the glass box until the HTB's collapsed. Videotape of the collapse indicated that when the critical load was reached, the snaplocks broke first (Fig. 2-7). Next, the scissor hinges broke, freeing the side plates from the center plate. Figure 2-8 shows the remains of the four center plates after a loading test. All

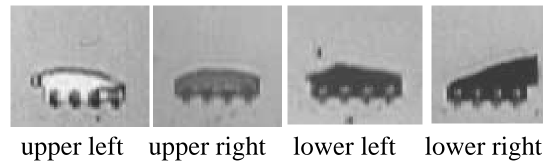

Fig. 2-8. Pictures of the remains of four corner HTB's

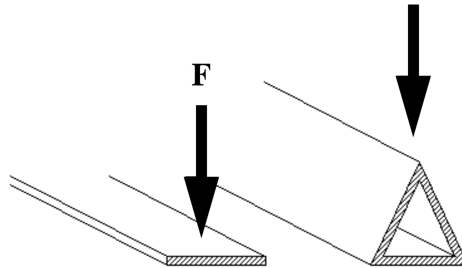

Fig. 2-9. Force being applied to both a flat beam and a hollow triangular beam. For the dimensions given in the text, the hollow triangular beam is 5 orders of magnitude stiffer than the flat beam.

polysilicon plates broke in approximately the same place, while all the substrate hinges remained intact. Total loads from 8.7 to 10.5gm have been observed at failure. If all twelve plates that made up these four HTB's were independent, the plates would fail by buckling at a calculated total critical load of only 0.4gm.

Similarly, we expect the HTB to have a higher stiffness compared to flat beams (Fig. 2-9). A clamped-free flat polysilicon beam 1mm long, 100μm wide, and 2μm thick has a spring constant of approximately 0.04N/m under small deflections. However, if we could create an HTB with rigid corners, the spring constant would be increased to 1,400N/m. Since, in reality, the HTB does not have rigid corners due to the snaplocks and scissor hinges, we expect the HTB to be stiffer than a flat beam though not as stiff as an HTB with rigid corners.

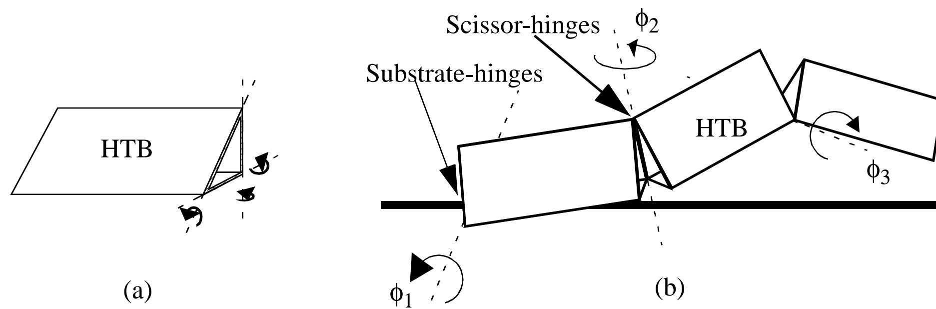

Fig. 2-10. Multiple DOF links. (a) A hollow triangular beam (HTB) has 3 different edges at each end where a joint may be placed. (b) Diagram of a 3-DOF articulated structure with 3 HTB's.

2.5 Articulated Joints and Multiple DOF

HTB's can be connected in series with scissor hinges as revolute joints to create multiple degree of freedom (DOF) structure (Fig. 2-10). Fig. 2-11 shows a 3-DOF articulated leg created from two rigid links. The leg has a pin-joint and two scissor hinges.

Since scissor hinges are used as revolute joints, their maximum angles of rotation affect the workspace of the manipulator. Various versions of hinge designs have measured maximum angles of rotation ranging from 111° to 146°. Deflection past the maximum angles of rotation is still possible as the two polysilicon plates connected by the scissor hinges bend elastically.

To give an estimate of the critical load on these scissor hinges, HTB's were tested on a standard probe station to failure. In these tests, unassembled HTB's (with right triangular cross-sections) were rotated 90° from the substrate. The center plate was held in position by two probe tips while the longer of the two side plates was rotated to the maximum angle then deflected slowly until failure (Fig. 2-12). Force was applied to the free edge of the side plate. By measuring the deflection of the side plate (assuming the center plate deflection at the hinge is small), a maximum force of roughly 1,000μN

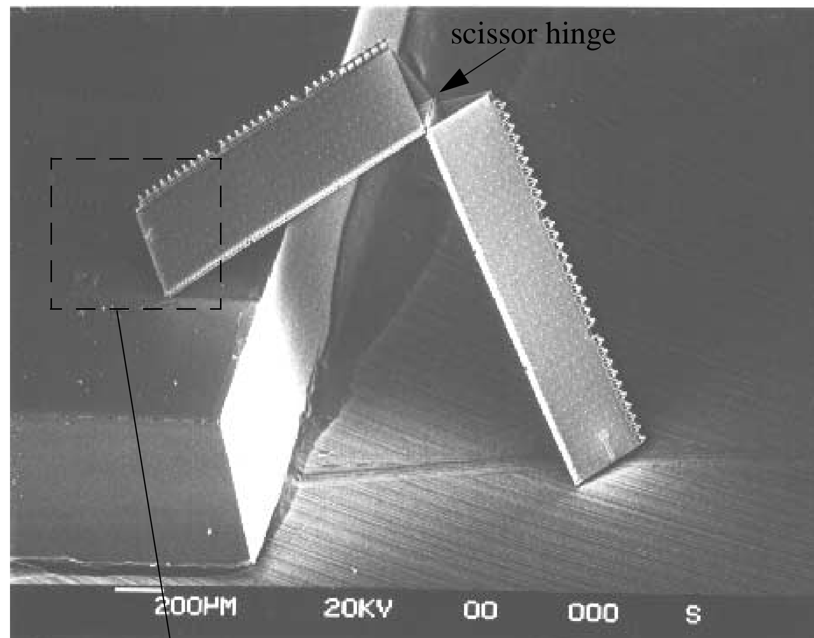

(a)

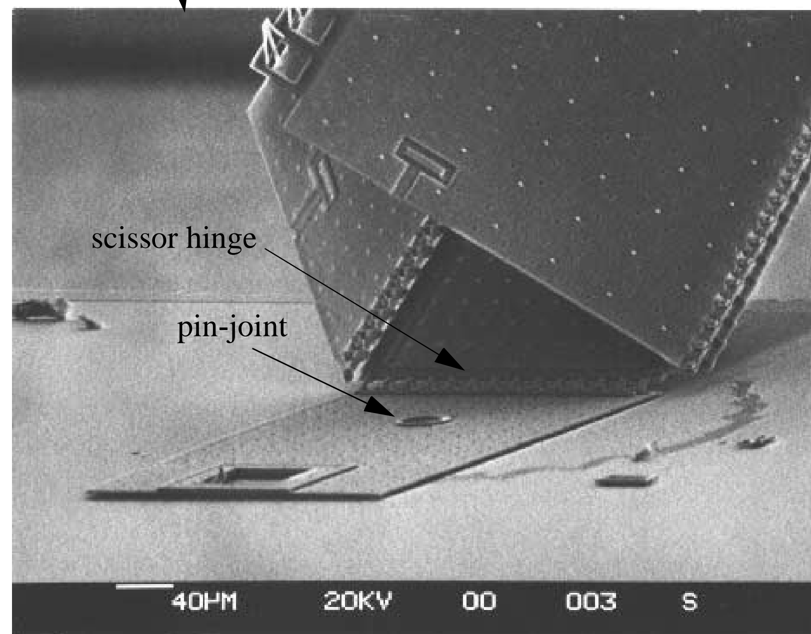

(b)

Fig. 2-11. (a) SEM of a 3-DOF leg with two links fabricated in the MUMPs process. Each link is 1.2mm long. The leg was assembled and rotated off the edge of the chip. (b) Close-up SEM of where the first link connects to the substrate via a scissor hinge and pin-joint.

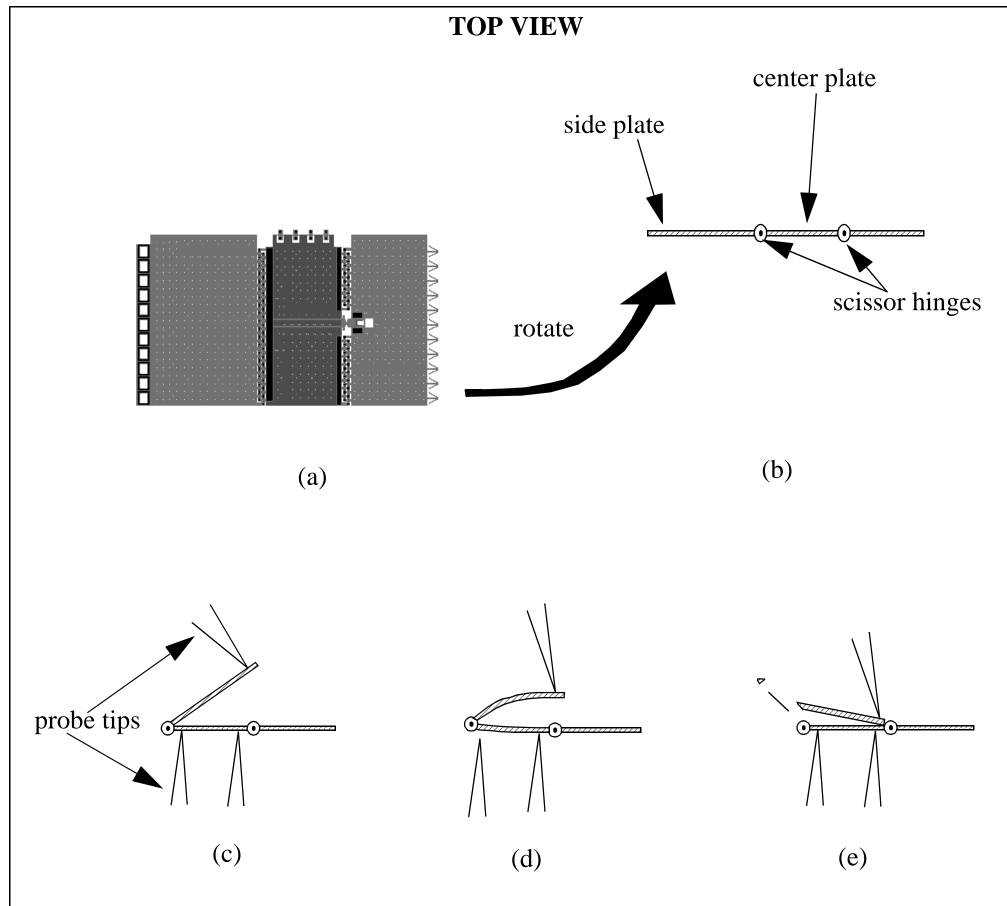

Fig. 2-12. Test procedure of scissor hinges. (a) Unassembled HTB. (b) Rotate HTB plates to 90° off the substrate. (c) Rotate side plate until maximum deflection is reached. (d) Deflect side plate slowly. (e) Scissor hinges break.

(equivalent to the weight of a $1cm^2$ silicon die) was estimated before the hinges broke.

2.6 Mechanical Coupling

Mechanical couplings connect rigid links to motors and convert linear force to torque at the joints. Each link requires its own mechanical coupling and motor. Surface-micromachined mechanical couplings are constructed from sliders, lever arms, and connecting-rods [92]. For a robot with substrate motors, the mechanical couplings require *n* degrees-of-freedom for the *n-th* link from the substrate. For example, a simple 1-DOF

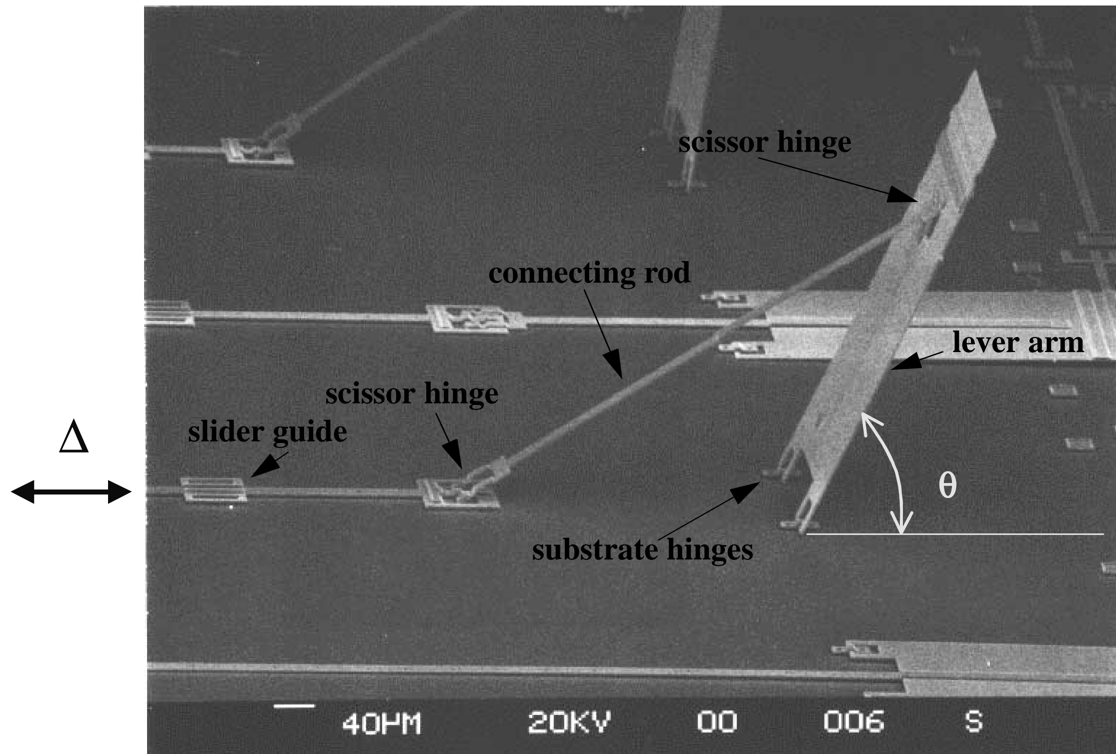

Fig. 2-13. SEM of a slider crank created from a hinged plate, connecting rod, and slider.

sliding crank such as the one shown in Fig. 2-13 can be used to couple the first link. To couple the second link of the leg, we would need a 2-DOF mechanical coupling. A five-bar linkage with a sliding crank (Fig. 2-14) can be used to provide this additional degree of freedom. Fig. 2-15 shows a 2-DOF test structure with two serial links and two mechanical couplings. The first mechanical coupling rotates the entire two-link structure while the second mechanical coupling rotates the polysilicon plate (second link). Fig. 2-15b shows how the second mechanical coupling can go through the first link and couple to the second link. Links, joints, and mechanical couplings together create an articulated leg. Fig. shows 2-DOF articulated leg with two links, two revolute joints, and two mechanical couplings.

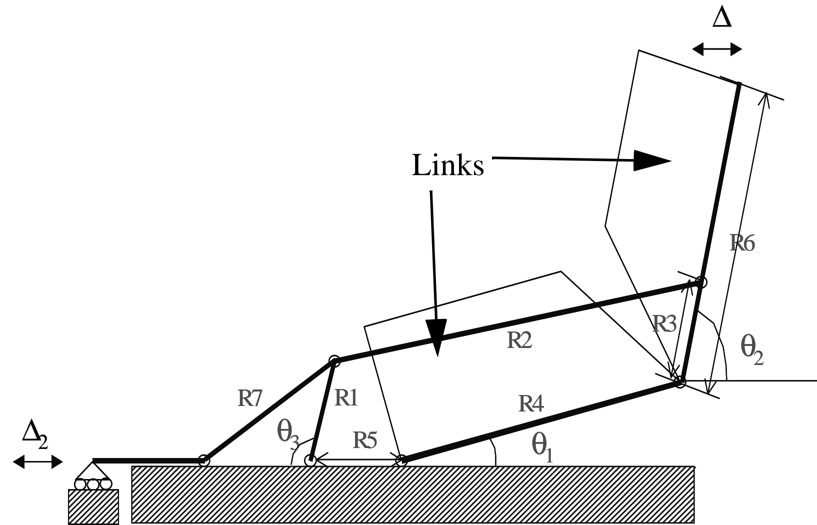

Fig. 2-14. Diagram of a slider crank coupled to a five-bar linkage. The lighter lines indicate the outline of the rigid links. Note that the rigid links and the substrate form part of the five-bar linkage.

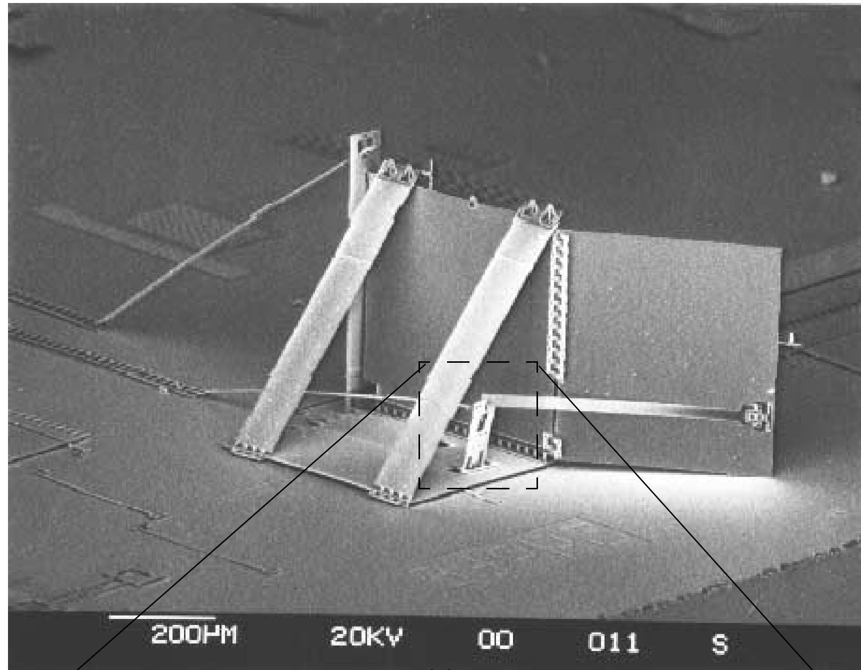

(a)

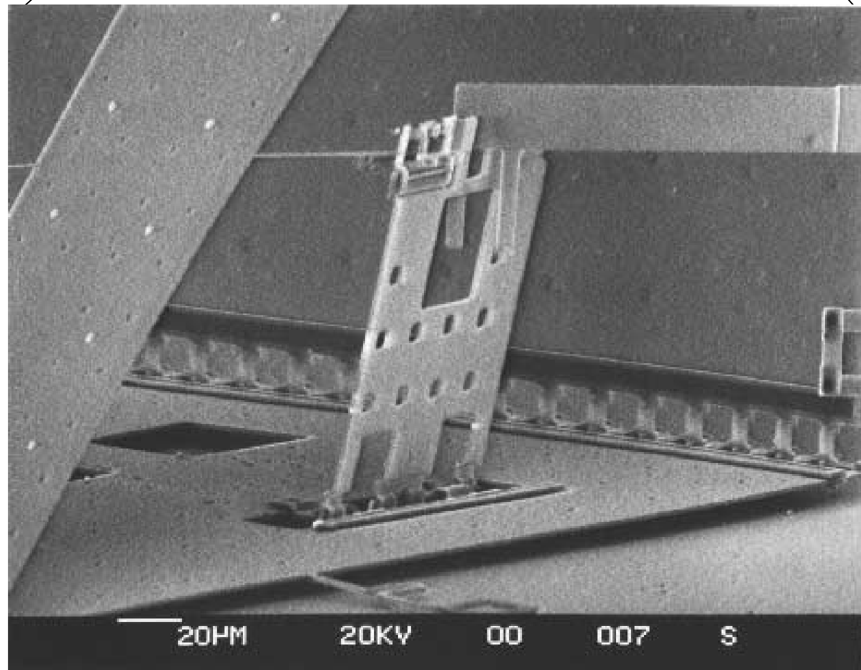

(b)

Fig. 2-15. Mechanical coupling for 2-link structure. (a) SEM of a 1-DOF and 2-DOF mechanical coupling test structure. (b) Close-up SEM of a lever arm inside the first link.

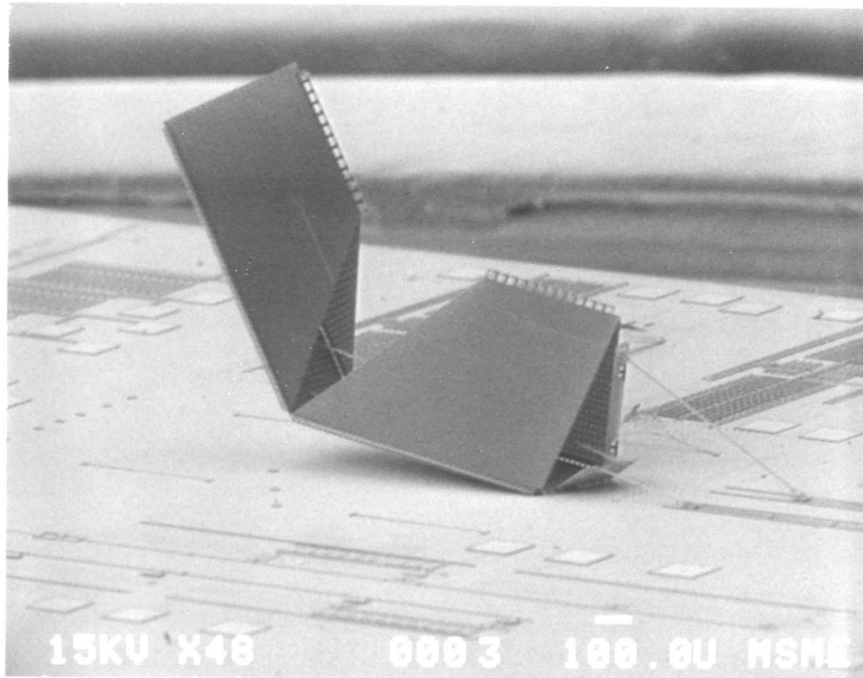

(a)

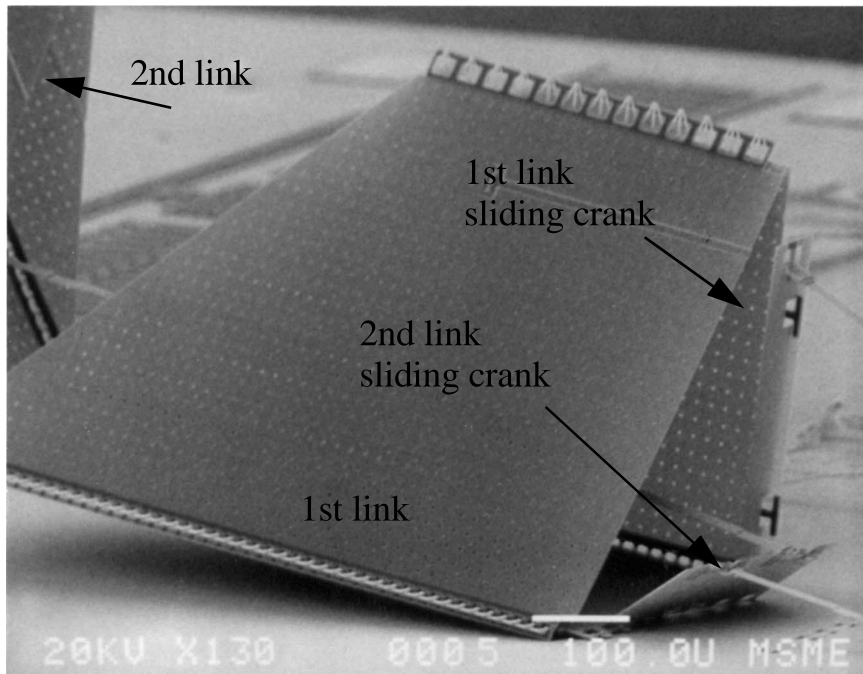

(b)

Fig. 2-16. 2-DOF legs and mechanical coupling. (a) SEM of a 2-DOF leg with two links and two sets of mechanical couplings. (b) Close up SEM of the first link of the 2-DOF leg with the mechanical couplings in view.

CHAPTER 3. ACTUATION

3.1 Introduction

Actuation is one of the biggest challenges in building a microrobot. Actuators are also a key building block. Unlike macro-sized robots where off-the-shelf actuators are available, microrobot actuators are not. Instead, microrobots require micro actuators that are specifically designed and fabricated for the purpose. Although there are plenty of papers in literature on MEMS actuators, few provide a complete set of performance metrics from which to compare the actuators with. In this chapter, we will propose a set of actuator figures of merit for autonomous microrobots. Using these figures of merit, we will show that electrostatic actuation is the most appropriate for autonomous microrobots compared to other alternatives. Next, the theory, design, fabrication and performance of electrostatic gap-closing actuators would be presented.

3.2 Figures of merit

3.2.1. Output Power Density

Since microrobots have extremely limited volume by definition, appropriate actuators must produce adequate power in a small volume. The output power density ($\frac{W}{m^3}$) is the amount of power produced by the actuator per unit volume.

$$\rho_P = \frac{1}{\text{volume}}\left(\frac{\text{work}}{\text{cycle}} \cdot \frac{\text{cycles}}{\text{sec}}\right) = \frac{\text{force} \cdot \text{stroke} \cdot \text{freq}}{\text{volume}} \tag{3-1}$$

The minimum force and maximum frequency should be used in the calculation. The output power density takes into account of the force, actuator stroke, speed, and size of the actuator.

3.2.2. Force density and force coefficient

In theory, output power density is the only issue when finding the right actuator. In practice, actuators must generate the minimum force required with a limited actuator volume regardless of output power density. For example, an actuator with low force, large stroke and high drive frequency may produce high power but would require large lever arms to lift a robot leg. The limitation in this case would be the total volume available on the microrobot. On the other hand, a low power actuator with high force but a small stroke and low maximum frequency may still be usable. A small stroke can be repeated and accumulated with an stepping action [2, 21, 80, 92] and low frequency would simply mean the microrobot will move slower which may not matter.

To compare different actuators, the force density should be normalized to the input power. We define this ratio as the force coefficient (γ):

$$\frac{\text{force}}{\text{volume}} = \gamma \cdot (\text{input power}) \rightarrow \gamma = \frac{\text{force}}{\text{volume} \cdot (\text{input power})} \tag{3-2}$$

3.2.3. Efficiency

Even if an actuator meets the output power density and force coefficient requirements, it may still not be practical for autonomous microrobots if the power efficiency is low. The efficiency is defined as:

$$\eta = \frac{\text{Output Power}}{\text{Input Power}} = \frac{\text{Output Energy}}{\text{Input Energy}} \tag{3-3}$$

As shown in Eqn. 3-3, inefficient actuators require high input power which the on-chip energy source may not be able to provide. For example, a 1cm^2 solar cell with 10% conversion efficiency can only provide ~10mW of power in full sunlight so for a robot with 10 motors, each motor can only have consume 1mW. With a power efficiency of 1%, each motor would only generate 10μW of power.

3.2.4. Integration

Though not a quantifiable figure, integration of the actuator with the rest of the robot (legs, power supply, control circuits, etc.) is non-trivial and should be considered when evaluating an actuator. Since our microrobot is fabricated in silicon, it would simplify integration if the motors were also fabricated in the same process along with the microrobot mechanisms such as legs and mechanical coupling. Alternatively, motors could be fabricated separately and then transferred to the microrobot by techniques such as gold bump flip-chip transfer [72]. This will be discussed in further detail in Chapter 6.

3.3 Comparison of Actuation Methods

MEMS actuators fall mostly into four categories: magnetic, thermal, piezoelectric and electrostatic. A good review of some of these actuators can be found in [25, 47]. In this section, we will briefly describe the each method and consider its figures of merit.

3.3.1. Thermal Actuation

Several types of actuation based on the thermal expansion have been demonstrated in MEMS including “unimorphs,” bimorphs, and shape memory alloys (SMA). In “unimorphs”, the actuator is heated by running a current through a single material such as silicon and the expansion is:

$$\Delta L = \alpha L(\Delta T) \tag{3-4}$$

where α is the thermal coefficient of expansion, L is the original dimension, and ΔT is the temperature change. Asymmetry in the geometry of the actuator causes the expansion of the actuator to one direction. A popular example is an actuator that has a wide arm coupled to a thin arm [21, 36]. Force and displacement are geometry dependent and have been analyzed in [22, 48]. The microrobot proposed by Kladitis et al. [45] are based on

arrays of these actuators. The power efficiency of these actuators are on the order of 10^{-4}% due to thermal dissipation from the actuator into the surrounding air and substrate. Another example is the microgripper by Keller et al. [44]. This gripper was fabricated in HEXSIL, a silicon mold process, and was able to pick and place 1 x 4 x 40μm silicon dioxide pegs into 4 x 4μm holes in silicon using 75mW of power. Thermal expansion of other materials such as polyimides has also been exploited. The first walking microrobot (non-autonomous) used polyimide-filled v-groove (PVG) joints [24]. When heated with resistive heaters, the wider surface of the PVG joint expands more than the narrower bottom, which rotates the connected silicon plates. A 30μm deep x 70μm wide x 600μm long polyimide-filled v-groove joint/actuators generates a force of ~1mN, a stroke of up to 150μm with a 200mW input power at an efficiency of 0.001% [24].

Another method to achieve differential expansion between two coupled structures are thermal bimorphs. In this method, the difference in expansion is between two mechanically-coupled materials with different thermal expansion coefficients. A heating element is typically sandwiched between the two materials. An example is the ciliary motion bimorphs by Ataka et al. [3] where a 2.4mg mass is moved at a velocity of up to 500μm/s by an array of 512 polyimide bimorph cantilevers with an input power of 4mW per cantilever.

Shape memory alloys (SMA) can produce large force and displacement when it undergoes a thermally-induced phase change. Good reviews of microfabricated SMA can be found in [41, 49]. A SMA microgripper was demonstrated with an opening of 110μm when heated to 70°C with an input power of 30mW at 100Hz [51]. With a power density on the order of 10^7W/m^3 [49], SMA's have attracted some attention as a potential microro-

bot actuator [13, 50]. However, an efficiency limit of less than 10% [33] is a drawback for autonomous systems.

Overall, thermal actuators are mechanically robust and can produce large force and displacement. However, the low power efficiency due to heat dissipation makes thermal actuators an impractical choice for autonomous microrobots.

3.3.2. Magnetic Actuation

Magnetic actuation is typically based on generating Lorentz force, which is given by:

$$\vec{F} = \oint I d\vec{l} \times \vec{B} \qquad (3\text{-}5)$$

where I is the current on a conductor, $d\vec{l}$ is the differential conductor element and $\vec{B}$ is the magnetic flux density. Implementation usually involves putting a suspended movable coil in a constant magnetic field or a suspended magnet in a modulated electromagnetic field. Magnetic actuators can produce large force and displacement. Chang et al. created surface micromachined magnetic actuators with 100μm of throw and forces on the order of 1-10μN with an input current amplitude of ~50mA [15]. To generate large forces, current on the order of 0.01-1A are needed. Unfortunately, high current is difficult to provide using on-chip energy sources. Miki et al. bypassed this problem by using an external magnetic source (100 Gauss, 100Hz) to actuate a mechanical flying insect with 900μm-long nickel rotors [61]. However, the insect can only operate inside the field-generating coil. In addition, heat loss due to finite coil resistance reduces the efficiency of magnetic actuators. For example, a rotational magnetic motor by Teshigaraha et al. has an efficiency of 0.002% [83].

3.3.3. Piezoelectric actuation

Piezoelectric materials produce a potential difference when strained and produce a strain when a potential difference is applied. These actuators can generate large forces/torques, consume low power with high efficiency, can be driven with low voltages, and is mechanically robust, making them a potential candidate for autonomous microrobots. In fact, several proposals can be found in literature about piezoelectric microrobots [28, 74]. However, fabrication and integration with silicon devices is difficult. When integration issues are resolved, then piezoelectric actuators could be the best solution for autonomous microrobots.

3.3.4. Electrostatic Actuation

Electrostatic actuators generate force by accelerating electrically-charged conductor(s) in an electric field. Depending on the suspension design, the conductor(s) can move perpendicular to the primary electric field flux as in a resonator [82], in the direction of the electric field flux as in a gap-closing actuator [2, 16, 93], or in a non-orthogonal direction as in the tangential drives [10]. Compared to the previously-mentioned actuation methods, electrostatic actuation is the most practical option for autonomous microrobots at this time. As we will describe in this section, electrostatic actuators have a high power efficiency, a high force density and an energy density which scales favorably in the microscale. In addition, electrostatic actuators only need insulating and conducting materials which integrates well with silicon processes without requiring special materials, magnetizing step or annealing steps. One disadvantage compared to thermal and magnetic actuation is the force-displacement trade-off. However, in general, this problem has been

solved by using an inchworm or stepping cycle to accumulate large displacements over time. Examples can be found in [2, 21, 80, 92].

3.3.4.1. Efficiency of electrostatic actuators.

The energy stored in a parallel-plate capacitor is:

$$U_c = \frac{1}{2}CV_c^{\,2} \tag{3-6}$$

where C is the capacitance and V_c is the voltage across the capacitor. This is the energy used to produce work in an electrostatic actuator. Efficiency depends on the charging technique. For a step-input voltage source, the energy required to charge the capacitor is:

$$U_i = P_i \cdot T = IV_i \cdot T = V_i\int_0^T C\frac{\mathrm{d}V_c(t)}{\mathrm{d}t}\mathrm{d}t = V_i\int_o^{V_i} C \cdot dV_c = CV_i^2 \tag{3-7}$$

where P_i is the input power, T is the time to charge the capacitor from zero to V_i, the input voltage. The efficiency limit (Eqn. 3-3) is then:

$$\eta = \frac{U_c}{U_i} = 50\% \tag{3-8}$$

Twice the stored energy must be supplied to charge the capacitor regardless of the magnitude of the series resistance (from the capacitor, switch, etc.). Half of the power is lost in thermal dissipation from the series resistance in the charging path (switching dynamics).

Power loss can be reduced by pseudo-adiabatic charging [4, 66, 67], which is a process with little thermal dissipation. The basic idea is to charge the capacitor with an input voltage signal that varies linearly from 0 to V over a period T >> RC [67]. The energy loss is then:

$$_L = P \cdot T \approx \frac{(RC)}{T}CV^2 \tag{3-9}$$

Assuming the capacitors are similarly discharged, the efficiency is then:

$$\eta = \frac{U_c}{2U_L + U_c} = \frac{\frac{1}{2}CV^2}{2\frac{RC}{T}CV^2 + \frac{1}{2}CV^2} = \frac{T}{RC+T} \tag{3-10}$$

This means the slower the input voltage is ramped, the more efficient the charging becomes. The cost is a slower switching frequency. This is a disadvantage for systems such as microprocessors where speed is a major concern. However, for autonomous microrobots, power is a major consideration rather than speed. In addition, for electrostatic actuators, the RC time constant is likely to be much faster than the mechanical time constant. For example, an array of electrostatic actuators with a maximum capacitance of 10pF and a series resistance of 100kΩ would need a charge time of >> 10µs to increase efficiency. A charge/discharge cycle of >> 20µs corresponds to a switching frequency of << 50kHz. In comparison, a large actuator array modelled as a mass-spring system with a mass of 25µg and a suspension spring constant of 1µN/µm has a resonant frequency of ~1kHz. If the actuators are switched at the 1kHz, the efficiency would be 92%. The theoretical limit of the efficiency would then depend on the mechanical speed of the actuator.

Several implementations of adiabatic charging has been proposed and demonstrated in low-power circuits [4, 42, 67, 96]. One implementation is inductive charging [96] shown in Fig. 3-1 .Suppose the initial voltage across the capacitor is zero. When the switch is closed, the inductor sees a potential difference of $V_f/2$. This causes current to

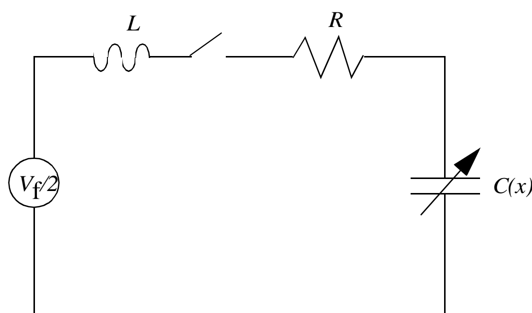

Fig. 3-1. Circuit model for adiabatic charging of a capacitor using inductor.

build up in the inductor as the potential difference across the capacitor swings towards V_f. When the $V_c=V_f$, then the switch is opened. The energy dissipated is [42]:

$$U_L = \frac{1}{2}C(\Delta V)\left(1 - e^{\left(\frac{-\pi\alpha}{\omega_d}\right)}\right) \tag{3-11}$$

where $\alpha=R/2L$ and ω_d is the drive frequency.

3.3.4.2. Force density of electrostatic actuators

Electrostatic actuators also scale favorably due to Paschen's Law (Fig. 3-2) which states that the breakdown electric field increases with decreasing electrode separation in the microscale [34, 65]. The breakdown voltage at a separation of 2μm and a pressure of 1 atm is about 300 V which, as the next section shows, can generate force densities on the order of 10mN/mm^3.

3.4 Comparison of Electrostatic Actuators

There are three common types of electrostatic actuators: gap-closing, comb-drive [82], and scratch-drive [2]. All three types are based on applying a voltage between a movable electrode and a stationary electrode. The force generated depends on the direction of motion of the movable electrode with respect to the electric field:

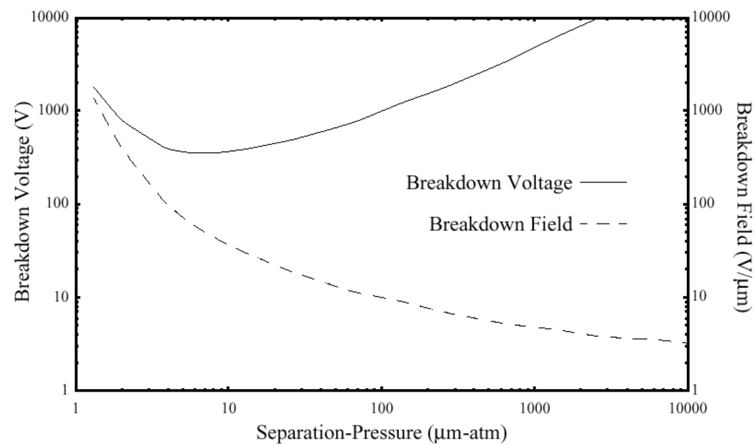

Fig. 3-2. A plot of the Paschen Curve-- breakdown field as a function of the electrode separation and pressure. (Judy [43]).

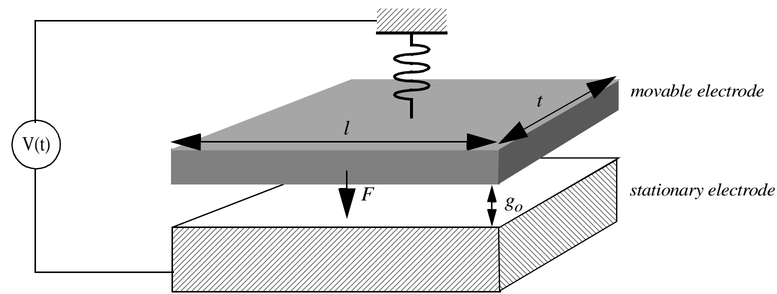

Fig. 3-3. Diagram of a gap-closing actuator. The movable electrode is separated from the stationary electrode by an initial gap (g_o). An applied voltage pulls the movable electrode towards the

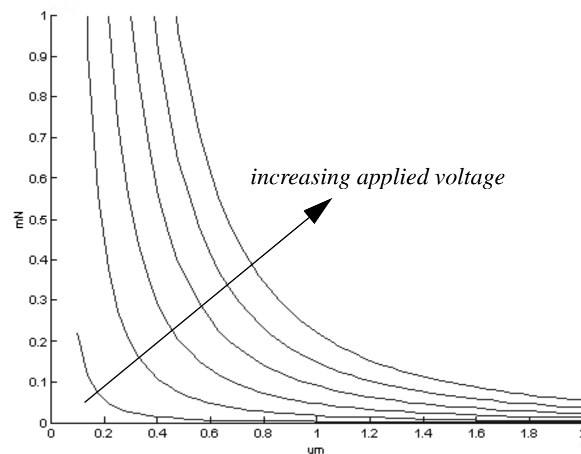

Fig. 3-3. Plot of force vs. electrode position for a gap-closing actuator with t=50µm, l=100µm and initial gap of 2µm.

$$F = -\frac{\partial U}{\partial \zeta} = \frac{1}{2} \cdot \frac{\partial C}{\partial \zeta} \cdot V^2 \tag{3-12}$$

where ζ is the direction of motion. The capacitance is:

$$C = \frac{\varepsilon t l}{g} \tag{3-13}$$

where g is the gap between the two electrodes, ε is the permittivity of the gap, t and l define the area of the electrodes. For the basic gap-closing actuator (GCA) shown in Fig.

3-3, the direction of motion is along the electric field so the force is inversely proportional to the gap squared:

$$F_{gca} = -\frac{1}{2}\varepsilon_o \frac{tl}{g^2} V^2 \tag{3-14}$$

The force-stroke curve is shown in Fig. 3-3 at different voltages. The force-stroke curve shows a high clamping force at the end of a stroke which could be useful in certain situations. Eqn. 3-14 can be rearranged as:

$$F_{gca} = -\frac{1}{2}\varepsilon_o l \cdot \left(\frac{1}{g}\right) \cdot \left(\frac{t}{g}\right) \cdot V^2 = -\left(\frac{1}{2}\varepsilon_o l\right) \cdot \left(\frac{1}{g}\right) \cdot \lambda \cdot V^2 \tag{3-15}$$

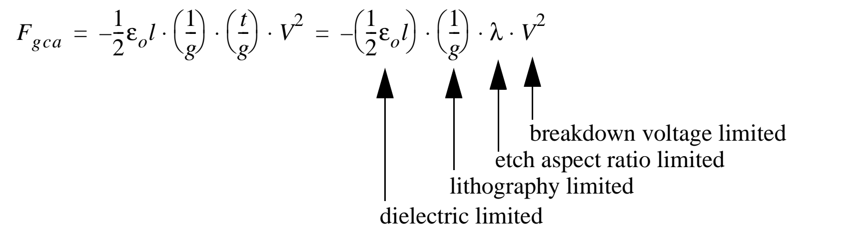

where λ=t/g is the aspect ratio of the electrodes. From the above equation, it is apparent that the force limit of GCA's are due to the permittivity of the dielectric between the electrodes (usually air or vacuum), the lithographic feature size (typically ~2µm), the electrode aspect ratio (~20:1 using DRIE silicon etching) and the breakdown voltage (~300V). Using the numbers just provided, the limit is 0.4mN per GCA unit cell with electrode length of 100µm. To create more force, a parrellel array of GCA unit cells can be created.

For comb-drive actuators (Fig. 3-4), the direction of motion is perpendicular to the electric field so the electrostatic force is inversely proportional to the gap:

$$F_{comb} = \frac{1}{2}\varepsilon_o \frac{t}{g} V^2 \tag{3-16}$$

Since the electrode moves parallel to each other, the force remains constant throughout the stroke. As the gap is on the order of 10^{-6}µm, GCA's generate more force than the comb-drives at the same voltage. We have demonstrated a 1mm x 0.6mm x 50µm array of 86

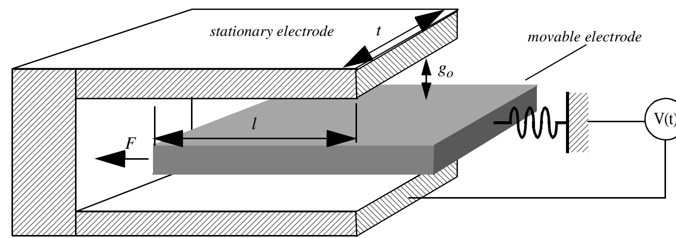

Fig. 3-4. Diagram of a comb-drive actuator. An applied voltage pulls the movable electrode parallel with the stationary electrodes in a direction that increases the overlap (l) between the electrodes.

GCA's which generated a measured force of ~260μN with 33V ($\sim 8 \frac{\mu N}{V^2 \cdot mm^3}$) with an estimated 8% efficiency [91]. Comb-drive actuators can also generate large forces at a slightly lower force density per voltage squared. Saif et al. designed a 4mm x 5mm x 12.5μm array of 9000 comb drive actuators that could generate ~1.5mN of force at 50V ($\sim 2.4 \frac{\mu N}{V^2 \cdot mm^3}$) with an estimated 25% efficiency [70].

The scratch-drive actuator (SDA), invented by Akiyama et al. [2], is another popular electrostatic actuator with high force densities, simple geometry, and can be fabricated in the commercial MUMPs process. The main component is a polysilicon plate with a bushing (Fig. 3-5). A 75μm x 60μm x 3μm SDA generated a measured force of 63μN with ±112V ($\sim 20 \frac{\mu N}{V^2 \cdot mm^3}$) [2]. The force density is much higher than both the GCA's and comb-drive actuators and the total displacement is essentially unlimited with step sizes on the order of 10nm. However, the SDA requires an electrode (at the SDA potential) the length of the total displacement. This electrode is separated from the opposing electrode (substrate) by a 0.5μm nitride, forming a potentially large parasitic capacitance which reduces efficiency (on the order of 0.01% for a travel of 100μm).

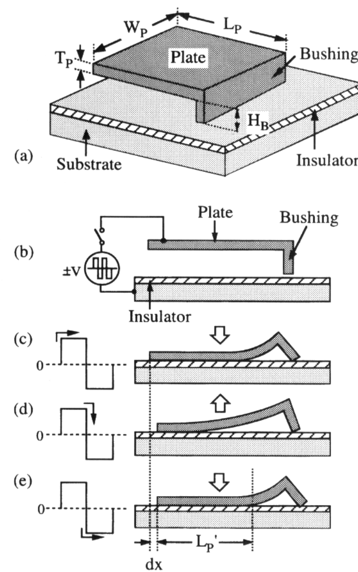

Fig. 3-5. The scratch-drive actuator (SDA). (a) Schematic of the main components. (b)-(e) cross-sectional view of the SDA in step motion by electrostatic pull-down of the plate. (From Akiyama [2]).

Overall, though scratch-drive actuators are not efficient, they evidently generate a much higher force density compared to gap-closing actuators and comb-drive actuators. SDA's are thus useful in applications where power consumption is not a major consideration. For example, they have been used in the assembly of hinged structures [1, 2, 46], micropositioning [55] and actuating micro-optical devices [20, 52, 54, 78]. For autonomous systems, the efficient gap-closing actuators and comb-drive actuators are both attractive options. With a high force density and a high clamping force at the end of a stroke, the GCA's are currently the best choice for autonomous microrobots at least until integration issues of piezoelectric actuation are resolved.

3.5 Gap-Closing Actuator Design

The basic GCA consists of two parallel beams of length, l, and thickness, t, separated by an initial gap, g_o (Fig. a). One beam is anchored to the substrate while the other is

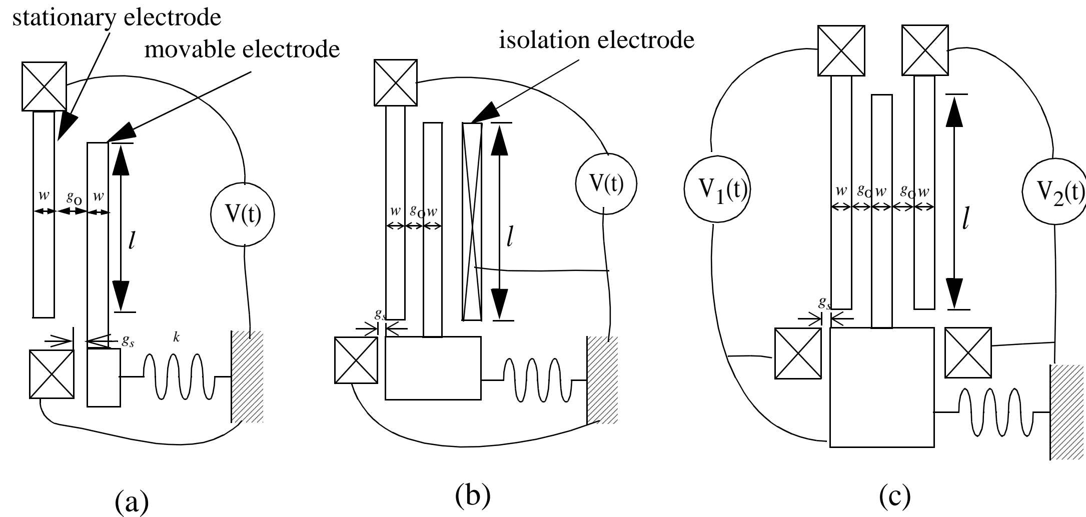

Fig. 3-6. Different gap-closing actuator topologies. (a) unit cell of simple one-directional GCA. (b) unit cell of one-directional GCA with an additional electrode to isolate the electrical field lines from the movable electrode to the stationary electrode of the next GCA unit. (c) unit cell of bi-directional GCA.

supported by a spring. To prevent shorting between the two beams, an anchored gap-stop biased at the same potential as the supported beam is used. The gap between the gap-stop and the supported beam, g_s is less than g. This gap, g_s, defines the actuator stroke. To generate more force, parallel arrays of GCA unit cells can be formed. Fig. 3-7 shows an example of a one-directional GCA array with two unit cells separated a gap of zg_o.

3.6 Static Model

3.6.1. Forces

In static equilibrium, the forces acting on the movable electrode in Fig. 3-7 are:

$$F_{e1} + F_{e2} + F_s = 0 \tag{3-17}$$

where F_{e1}, F_{e2} are the electrostatic forces acting from the left and right sides of the beam, respectively, and F_s, is the spring restoring force. The main electrostatic force, F_{e1} is:

$${}_{e1} = -\alpha\frac{1}{2}\varepsilon_o N V^2 \frac{tl}{(g_o - x)^2} \tag{3-18}$$

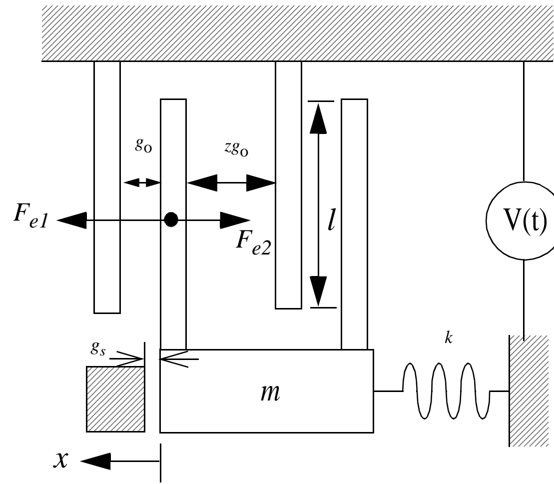

Fig. 3-7. An array of two gap-closing actuators.

where α is the fringe field factor [12], g is the gap between the electrodes in a GCA unit, N is the number of GCA's in the array and x is the position of the movable electrode as shown in Fig. 3-7. Note that α is a factor of the aspect ratio t/g and approaches unity for aspect ratio > 5 [12]. F_{e2} is given by a similar equation:

$$F_{e2} = -\alpha\frac{1}{2}\varepsilon_o N V^2 \frac{tl}{(zg_o + x)^2} \tag{3-19}$$

where $z \times g_o$ is the distance between GCA unit cells. Note that this is a parasitic electrostatic force that acts against F_{e1}. F_s is given by Hooke's Law:

$$F_s = -kx \tag{3-20}$$

3.6.2. Pull-in Voltage and pull-in gap

In quasi static equilibrium, the total energy in the GCA system is stored in the capacitor and spring:

$$U(g, V) = \frac{1}{2}k(g_o - g)^2 - \frac{1}{2}\varepsilon_o\frac{tl}{g}V^2 \tag{3-21}$$

where g is the moving electrode position, V is the applied voltage between the electrodes and k is the spring constant of the electrode suspension. Fig. 3-8 shows a plot of the total

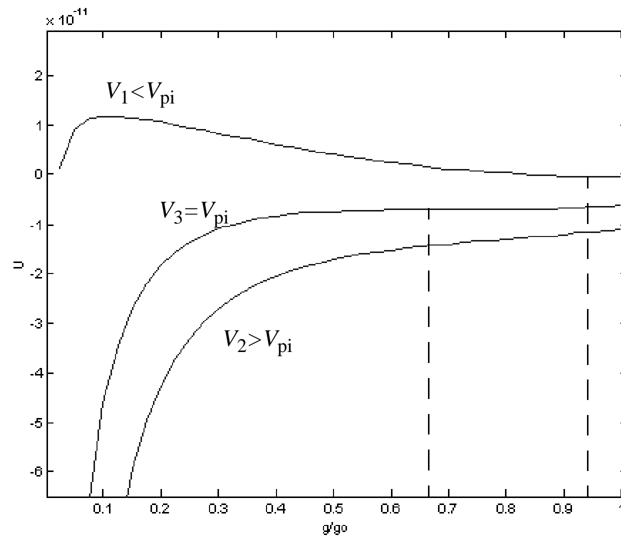

Fig. 3-8. Total energy of the GCA system as a function of the gap and applied voltage.

energy as a function of the gap for several applied voltages. The stable equilibrium point, g_{eq}, is where the total force is zero:

$$F = \frac{\partial}{\partial g} U(g, V)\big|_{g = g_{eq}} = 0 \tag{3-22}$$

and the effective spring constant is > 0:

$$k_{eff} = \frac{\partial F}{\partial g} = \frac{\partial^2 U(g, V)}{\partial^2 g} > 0 \tag{3-23}$$

At an applied voltage of V_i, the equilibrium position is ~$0.95g_o$. As the voltage is raised, the equilibrium point shifts and the gap is reduced. There exists a pull-in voltage, V_{pi}, where the system becomes unstable ($F=0$, $k_{ef} < 0$) and the gap is snapped closed [18]. The point where this occurs is the pull-in point, g_{pi}. By using the two conditions for instability ($F=0$, $k_{ef} < 0$) and Eqn. 3-22 & 3-23, we derive the pull-in voltage and pull-in point to be:

$$V_{pi} = \frac{8}{27} \cdot \frac{k g_o^3}{\varepsilon_o t l} \tag{3-24}$$

$$g_{pi} = \frac{2}{3} g_o \tag{3-25}$$

All voltages above V_{pi} would cause the gap to snap closed without any equilibrium points.

With a load of F_L, the energy function becomes:

$$U = \frac{1}{2}k(g_o - g)^2 - \frac{1}{2}\varepsilon\frac{tl}{g}V^2 + F_L(g_o - g) \tag{3-26}$$

Using the conditions at the onset of instability given by Eqns. 3-22 & 3-23, the pull-in voltage and point are:

$$V_{pi} = \frac{8}{27} \cdot \frac{k\left(g_o + \frac{F_L}{k}\right)^3}{\varepsilon_o tl} \tag{3-27}$$

$$g_{pi} = \frac{2}{3}\left(g_o + \frac{F_L}{k}\right) \tag{3-28}$$

3.6.3. Failure Voltage

The pull-in voltage, V_{pi}, gives the lower voltage limit for GCA operation. The upper voltage limit depends on the GCA design. When a voltage greater than V_{pi} is applied, the GCA movable electrode moves to and stops on the gap stop. However, if the voltage is high enough, the gap stop will not prevent the two electrodes from making a catastrophic contact. Depending on the gap stop location and electrode design, the contact can be made by the movable electrode bending either as a clamped-clamped beam or a cantilever towards the stationary electrode, or the movable electrode and the stationary

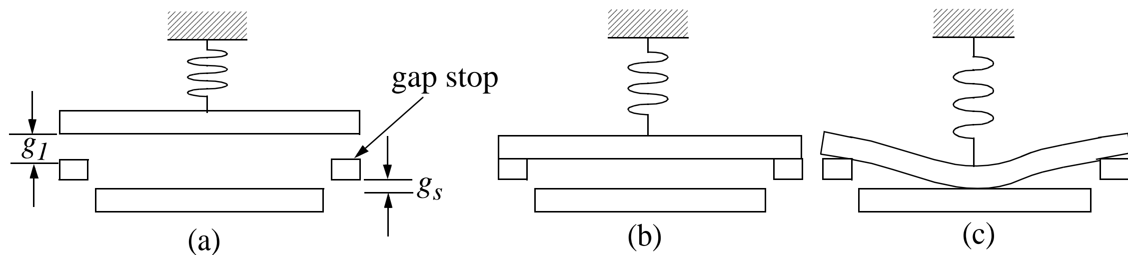

Fig. 3-9. Maximum voltage allowed is limited by non-rigid behavior of the electrode. Above is one of the examples of such behavior. (a) Initial position. (b) After voltage is applied, the movable electrode makes contact with the gap-stop. (c) Movable electrode bends towards the other electrode and makes contact.

electrode can bend towards each other. Deriving the closed-form solution for these non-linear problems is still an open problem. However, for the case where the movable electrode bends in cantilever fashion toward a rigid stationary electrode, the maximum voltage is approximated by [64]:

$$V_{max} = \sqrt{\frac{0.28Ew^3d^3}{\varepsilon l^4\left(1 + 0.42\frac{d}{t}\right)}} \tag{3-29}$$

3.6.4. Force Density

The force density of the GCA array at the initial gap is a good metric to compare different GCA designs. The force density is defined as the maximum usable force in a given volume. The usable force is defined at the initial gap when *x=0* because that force must be high enough to overcome the load. The maximum force is generated when the applied voltage equals the failure voltage (Eqn. 3-29). The calculations are different for each GCA topology (Fig.). This section will derive the force density of the basic GCA topology in Fig. 3-7. The unit cell volume is:

$$Volume = area \times thickness = (2w + g + zg) \times l \times t \tag{3-30}$$

The force density then can be derived by substituting x=0 and V=V_{max} (Eqn. 3-29) into the total force (Eqn. 3-17) and dividing it by the volume:

$$FD = \left(\frac{1}{g(z+1) + 2w}\right)\left(\frac{1}{g^2} - \frac{1}{(zg)^2}\right)\left(\frac{0.28Ew^3g^3}{l^4\left(1 + 0.42\frac{g}{t}\right)}\right) \tag{3-31}$$

where E is the Young's Modulus of Silicon. From Eqn. 3-31, we can determine the upper limit of the force density of a GCA array purely by it's geometrical design. The actual force density would be lower than given in Eqn. 3-31 if areas used for non-force generat-

ing structures such as bond pads, springs, trusses, etc. are included. A good metric to evaluate GCA array design would be the area efficiency:

$$\eta = \frac{\text{actuator area}}{\text{total area}} \tag{3-32}$$

where *area* is the area of the unit cell.

3.7 Dynamic Model

Next, we examine the one dimensional dynamic analysis of the moving GCA array. We consider the following forces in our model:

$$m\ddot{x} + b\dot{x} + kx = F_{e1} + F_{e2} + F_L \tag{3-33}$$

where F_{e1}, F_{e2}, were given in Eqn. 3-18, 3-19, respectively, and F_L is the load. We assume damping is dominated by the squeeze film effect, which becomes significant at high speeds or when the gap between the beams becomes small compared to the length and thickness of the beams. The following damping force is based on Starr [76]:

$$F_{sq} = -\frac{N\left(1 - 0.6\frac{t}{l}\right)t^3 l\mu}{(g_1 - x)^3}\dot{x} = \frac{-b\dot{x}}{(g_1 - x)^3} \tag{3-34}$$

where μ is the viscosity of air and $t < l$. Substituting Eqn. 3-18, 3-19, and 3-34 into Eqn. 3-33, we arrive at the 1-D dynamics equation for the supported beam:

$$m\ddot{x} + \frac{b\dot{x}}{(g_1 - x)^3} + k_s x = k_e\left(\frac{1}{(g_1 - x)^2} - \frac{1}{(g_2 - x)^2}\right) + F_L \tag{3-35}$$

where $k_e = \frac{1}{2}N\varepsilon_o t l V^2$.

At high drive frequencies, squeeze film damping dominates and Eqn. 3-35 can be rewritten as (assuming F_L=0):

$$\frac{b}{(g - x)^3} \cdot \frac{dx}{dt} \approx \frac{k_e}{(g - x)^2} \tag{3-36}$$

Solving t as a function of position, x, we get:

$$t = \int_{x_1}^{x_2} \frac{b}{k_e(g - x)} dx \tag{3-37}$$

where x_1 and x_2 are the initial and final electrode positions.

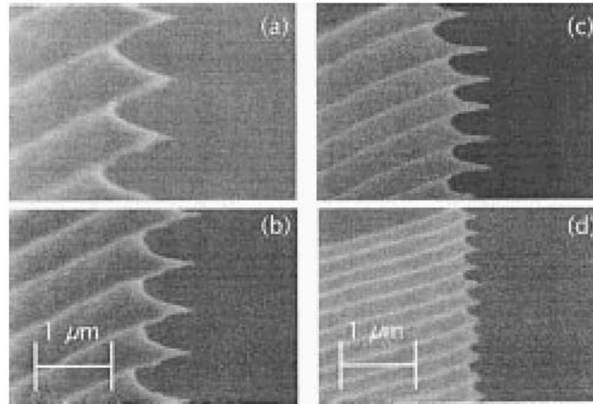

Fig. 3-10. Four SEM photos of a DRIE etched SOI sidewall. (a)-(d) shows the various tip densities possible by varying the passivation/etch cycle times. (From Milanovic [59]).

3.8 Optimization

Optimizing the GCA array for the highest force density depends on the specific topology of the array. The parameters to designing a GCA topology as shown in Fig. 3-7 are: electrode gap (g), gap between gap-stop and electrode (g_s), electrode thickness (t), electrode width (w), electrode length (l), and surface roughness of the electrode sidewalls (R_a). The effect of each parameter on the GCA force density (Eqn. 3-31) is discussed in this section.

3.8.1. Initial gap (g)

The smaller the gap the higher the force density. The lower limit of the initial gap is determined by the surface roughness of the electrode sidewalls and field emission. If the electrodes are fabricated from deep-reactive-ion-etched SOI wafers, they will have scalloped tips on the sidewalls as shown in Fig. due to passivation/etch cycling. To prevent shorting, the final gap must be greater than the surface roughness or tip height of the electrode sidewalls:

$$\text{Final Gap} = g - g_s > 2R_a \tag{3-38}$$

Field emission from the scalloped tips is a function of the radius of curvature of the sidewall features, the gap and the voltage between the gap. From [59], STS-etched SOI wafers with 22µm-thick device layer silicon tips separated by 2.2µm conducts a current of ~0.2mA at 40V at lowered pressures in the millitorr range.

3.8.2. Actuator stroke (g_s)

Larger stroke results in lower force (Eqn. 3-18). This gap is determined by the maximum aspect ratio λ achievable and the thickness of the device. The aspect-ratio is defined by the deepest and most narrow trench etchable:

$$\lambda = \frac{\text{trench depth}}{\text{trench width}} = \frac{t}{g_s} \tag{3-39}$$

3.8.3. Electrode thickness (t)

The thicker the electrode the higher the force density until $t > \lambda \times g_s$. After that point, the force density would decrease as the gap would have to be increased in order for the GCA to be fabricated.

3.8.4. Maximum voltage (V)

The maximum GCA voltage allowable may be limited by the buffer transisters. The current buffers are made in the solar cell process and has significant leakage current through the channel when the drain-source voltage is ~30V. There is also a voltage limit imposed by the ionization of gas between the electrodes as mentioned in Section 3.4. From the Paschen Curve, if the final gap (g-g_s) is 2µm and the pressure is 1atm, then the breakdown voltage is approximately 300V.

3.8.5. Electrode length (l)

The longer the electrode, the higher the area efficiency because there will be less percentage of the area spent on support structures. In addition, from Eqn 3-18, the force increases linearly with length. However, the failure voltage (Eqn. 3-29) is proportional to $1/l^2$ and the electrostatic force is proportional to the voltage squared ($F_e \propto 1/l^4$) so the shorter the electrode, the higher the force density achievable.

3.8.6. Electrode width (w)

The larger the width, the larger the unit cell (*Volume* ~ *w*) becomes which would decrease the force density. However, since the failure voltage is proportional to $w^{3/2}$ (Eqn. 3-29), the force density increases instead as this effect dominates.

3.8.7. Unit cell separation (z)

The larger the unit cell separation the lower the parasitic electrostatic forces (Eqn. 3-19) which increases the force density. However, as the separation increases so does the total actuator area which decreases the force density.

3.8.8. Optimization for high force density

All of the above parameters except for length, width and separation should be chosen first. Length, width, and unit cell separation have coupled effects and should be optimized simultaneously. Optimum values can be determined by plotting the force densities (Eqn. 3-31) using the values for predetermined parameters shown in Table 3-1. For example, given the input parameters shown in Table 3-1 the optimum values for the length,

width ,and separation are listed in Table 3-2. A matlab script (Appendix A) was written to

Table 3-1: Input

Parameter	Value
g_s	2μm
g	4μm
t	50μm
V	35V

Table 3-2: Optimized Output

Parameter	Value
width	2.1μm
length	128μm
separation	$2.4 \times gap$
force density	$0.7\frac{mN}{mm^2}$

determine theses values automatically and provide the graph of the force density as shown in Fig. 3-11.

3.9 Fabrication

3.9.1. Polysilicon Process

Initial GCA arrays were fabricated in the MUMPs process. A quick description of the process layers is as follows:

- Silicon substrate
- 0.5μm thick silicon nitride
- 0.5μm thick polysilicon electrode layer
- 2μm thick PSG
- 2μm thick polysilicon structural layer

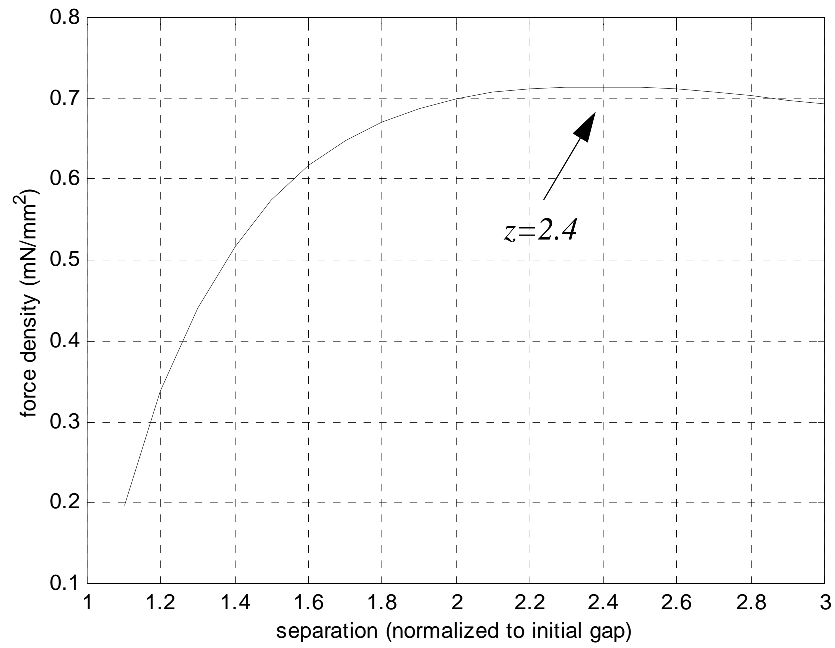

(a)

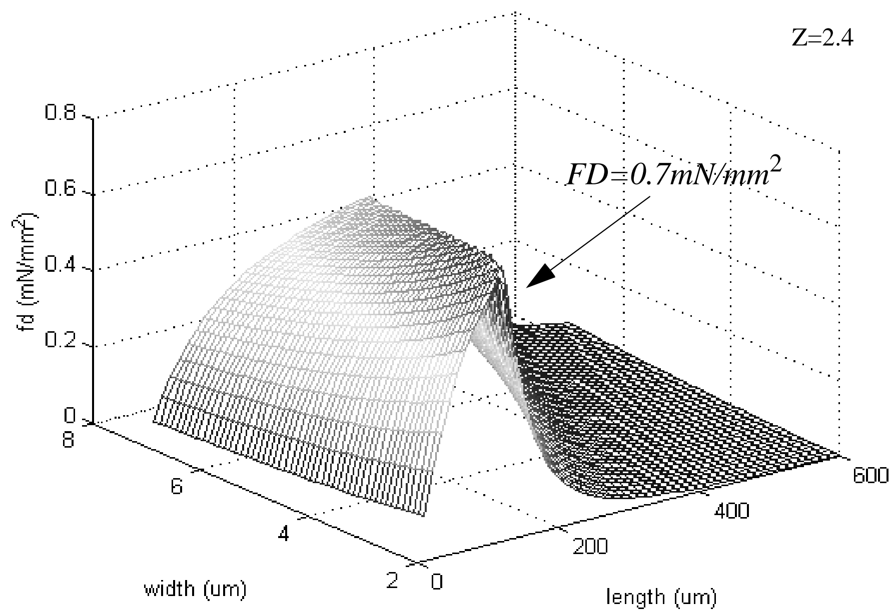

(b)

Fig. 3-11. Output of GCA optimizer. (a) Force Density as a function of unit cell separation. (b) Force density as a function of width and length at the optimized unit cell separation.

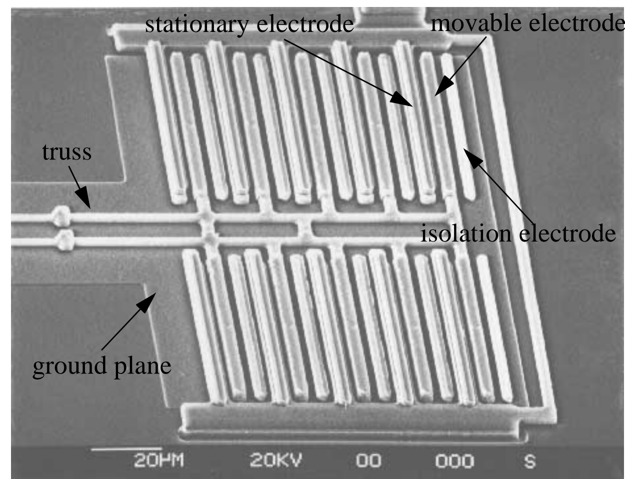

Fig. 3-12. SEM of a gap-closing actuator array fabricated in MUMPs. The gap-stop is not in view.

- 0.5μm thick PSG
- 1.5μm thick polysilicon structural layer
- 0.5μm thick gold

After fabrication, the chips are etched in 49% hydrofluoric acid to remove the sacrificial oxides. To reduce release stiction between the polysilicon structures and the substrate, the dice are dried in supercritical carbon dioxide after the sacrificial etch [62]. Fig. 3-12 shows one of the GCA arrays fabricated in MUMPs. The actuators were functional (the one shown in the figure had a V_{pi} of 35V) but the low aspect ratio (3.5:2) and polysilicon stress gradient caused stiction problems between the movable structures and the substrate. In addition, there was a stiction between the movable electrode and gap-stop during operation. This may be due to contact between the smooth polysilicon sidewalls. Self-Assembled Monolayers [39], which reduce release stiction, were tried but did not alleviate the problem.

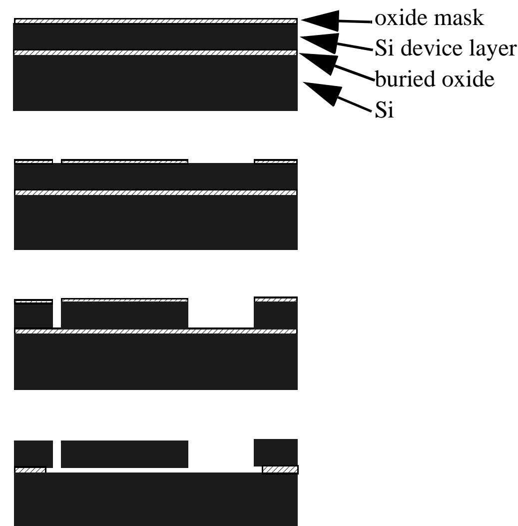

Fig. 3-13. Single-Mask fabrication process. (a) Oxidize wafer to create mask layer. (b) pattern oxide. (d) etch Si. (e) HF etch of Si.

3.9.2. Single Crytalline Silicon Process

Because of the problems associated with polysilicon GCA's, we switched to a single mask, custom SOI process. The process flow is shown in Fig. 3-13. and detailed in Appendix B. We start with a SOI wafer that has a top layer silicon thickness of 15 - 50µm, a buried oxide layer of 2µm, and a silicon handle wafer. A 0.5µm-thick oxide masking layer is thermally grown on the wafer. The masking layer is patterned by the single mask and then photoresist (PR) is removed to prevent PR from being hardened in the silicon etch. The exposed silicon areas are etched down to the buried oxide using the Surface Technology Systems Limited (STS) Advanced Silicon Etch (ASE) process. The wafer is diced and then the buried oxide is removed in a timed etch that allows narrow structures to be released while wider structures are anchored by remaining oxide underneath. To reduce release stiction, the wafer is dried in a critical point dryer (CPD). After mounting the chip to a package, aluminum wires are bonded directly to bare silicon pads on the chip

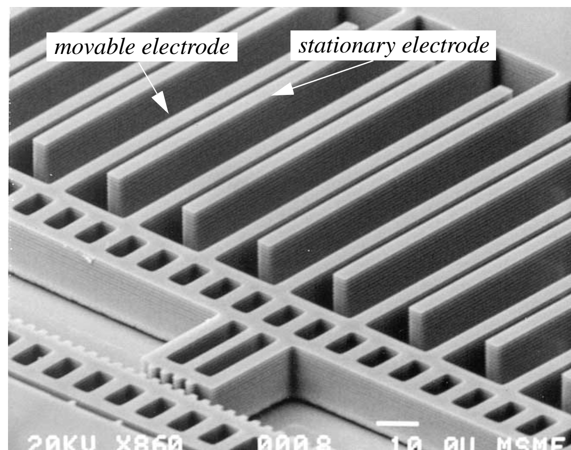

Fig. 3-14. SEM of a gap-closing actuator fabricated in the SOI process. Device layer is 15μm thick.

for testing at a probe station. Fig.3-14 shows an SEM of a GCA array fabricated in this process.

CHAPTER 4. LINEAR ELECTROSTATIC INCHWORM MOTORS

4.1 Introduction

As described in Chapter 1, microrobots require displacements on the order of tens to hundreds of microns and the forces on the order 0.1-1mN for locomotion. Due to the force-displacement trade-off for GCA actuators (Eqn. 3-14), it is not possible meet both the force and displacement requirements simultaneously using those actuators alone. Fortunately, GCA arrays can be used in an inchworm motor where small GCA displacements can be accumulated over time to generate large displacements without trading off the force.

A handful of good MEMS motors has been demonstrated in the past few years. An expression for force is:

$$F = fV^2A \tag{4-1}$$

where f is a force coefficient relating the motor force to the applied voltage (V) and motor area (A). The force coefficient can be used to to compare different motors as shown in Fig. 4-1. In 1995, Ezekiel Kruglick demonstrated the first MEMS electrostatic linear inchworm motor [93]. This motor, using GCA's, generated approximately 6.5μN of force with 35V and accumulated 40μm displacement in 2μm increments. The first inchworm motor was fabricated in MUMPS which limited the force density of the motor due to the low aspect ratio of the features. In addition, the stress gradient inherent in LPCVD polysilicon films limited the overall size of the motors. In 1997, Baltzer et. al. [8] reported a GCA

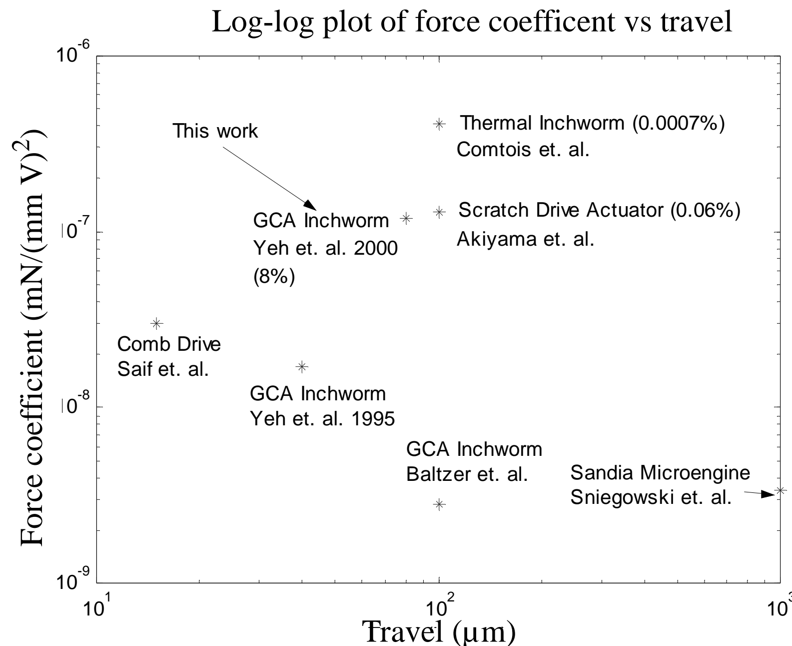

Fig. 4-1. A log-log plot of the force densities normalized to the voltage squared vs. the stroke of several motors [2,8,21,31,70,92]. Note the Sandia microengine is a rotary motor which produces large torque and travel. Its force coefficient is estimated from its comb-drive actuators. Energy efficiency are noted in parenthesis.

inchworm motor fabricated in a similar process. It had a larger travel but the force density was still low. Saif et. al. [70] demonstrated a high aspect-ratio millimeter-sized comb-drive actuator which produced a high force density but had limited travel. The Sandia Microengine [31] used a low aspect ratio comb-drive actuator which produced a low force density but, with its gear trains, achieved large travel and large torque. The motors presented here were fabricated in Silicon-on-Insulator (SOI) wafers with an aspect ratio of up to 25:1. This enables us to achieve a theoretical force density of approximately 1mN/mm^2 at 30V. Other MEMS motors with similar force densities are the thermal inchworm motor [21] and the scratch drive actuator [2]. However, both of these motors are extremely inefficient and thus would not be appropriate for autonomous microrobots. In 2001, we pub-

lished on improved linear inchworm motors with up to 80µm of travel (limited by stops not by force density), up to 260µN of force, and velocity of up to 4mm/sec [91]. In this chapter, we will describe this class of motors.

4.2 Design

The idea of the inchworm motor is to generate large travel by accumulating incremental displacements. The incremental displacements are produced by a clutch that attaches to a shuttle, pulls the shuttle, detaches from the shuttle and return to its initial position. The clutch and shuttle both have gear teeth to reduce slipping between the clutch and shuttle during the pulling action. For an *n*-phase motor, there are *n* number of clutches that sequentially attach, pull, and release from the shuttle. A minimum of two clutches that operate 180° out of phase on the same shuttle can generate a large travel over time. At least one of the clutches in a motor needs to have 2 dimensional (x-y) motion to attach and pull. The clutch motion is provided by GCA arrays. With this basic concept, several versions of inchworms motors can be realized as shown in Fig. 4-2. Fig. 4-2a shows a motor

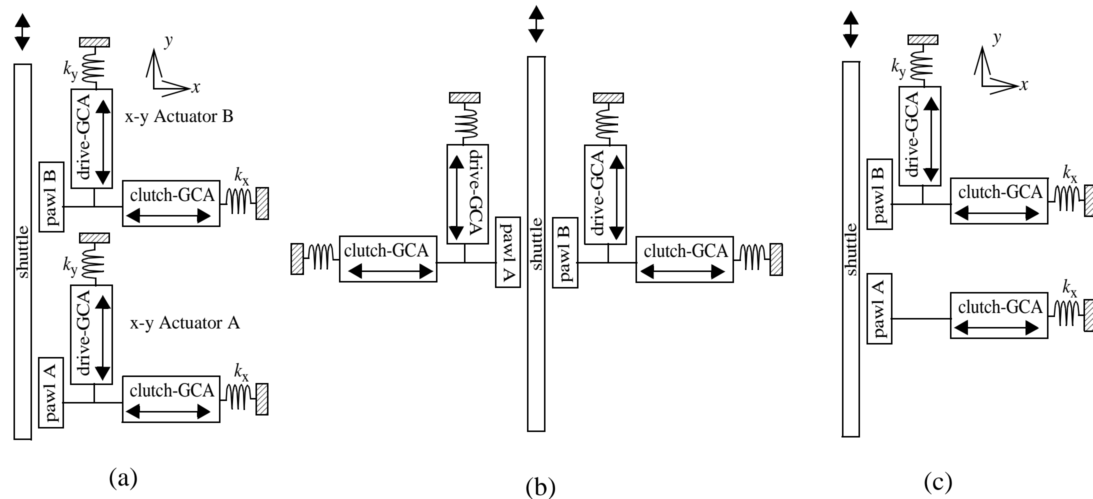

Fig. 4-2. Examples of various inchworm motor layouts. (a) A two-phase single-sided motor for narrow footprints. (b) two-phase, double-sided motor. (c) A single-phase, single-sided motor with extra clutch to hold shuttle position between cycles.

designed with a narrow footprint. Two clutches are lined up on one side of the shuttle. Each clutch is attached to an x-y actuator which is created by two orthogonally oriented GCA arrays. To move the shuttle, the two x-y actuators alternately move the shuttle as shown in Fig. 4-3. A full inchworm cycle is completed after both clutches have displaced the shuttle once. The step displacement (Δ) is defined by the GCA actuator stroke, which is typically minimized for high force density.

4.2.1. Attachment Force

The attachment force must be high enough so that the clutch does not slip from the shuttle during the pulling step. Earlier motors [93] used electrostatic attraction or friction from the smooth sidewalls of the pawl and shuttle as an engagement force. In the former case, a potential difference is applied between the clutch and the shuttle, causing the clutch to attach to the shuttle. A current-limiting resistor was used to limit currents to tens of

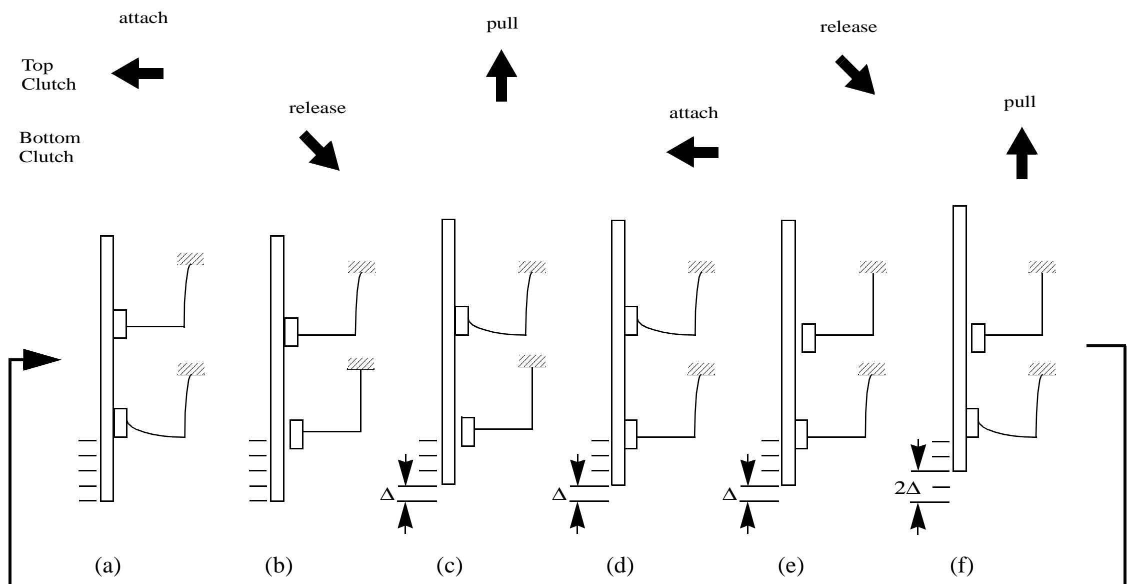

Fig. 4-3. Diagram of an inchworm cycle for motor configuration in Fig. 4-2a. Top half of the figure shows the direction of motion of the clutches. (a) top clutch attaches to shuttle. (b) bottom clutch detaches from shuttle and returns to initial position. (c) top clutch pulls shuttle. (d) bottom clutch attaches to shuttle. (e) top clutch detaches from shuttle and returns to initial position. (f) bottom clutch pulls the shuttle.

nanoamperes but the clutch still had problems releasing from the shuttle after the applied voltage was turned off. In the friction approach, a GCA array pushed the clutch against the shuttle. The shuttle acted as a gap stop to prevent the clutch GCA from shorting. The GCA gap is larger than the initial gap between the clutch and shuttle. The clutch and the shuttle were both grounded to prevent shorting and sticking. However, the clutch often slipped during the pulling step. When the attachment force was increased to reduce slipping, the electrostatic levitation force [82] of the clutch GCA electrodes increased, causing the clutch to slip *over* the top of the shuttle. In our current approach, gear teeth are added onto the clutch and shuttle to prevent slipping along the length of the shuttle. Also, creating high aspect ratio springs increases the spring constant in the z-direction which prevents the clutch from slipping over the top of the shuttle. The attachment force is provided by the clutch GCA array. From Chapter 3, the attachment force is given by:

$$F_c = \alpha\frac{1}{2}\varepsilon_o N c V_c^2 \frac{t l_c}{(g_c - x_c)^2} \tag{4-2}$$

which only needs to be large enough to push the clutch into the shuttle. The gear teeth provide the gripping, passively. This allows us to save area by needing smaller clutch GCA arrays. Detachment of the clutch is achieved passively by clutch supporting spring.

4.2.2. Pulling Force

The drive GCA array provides the pulling force, which is given by:

$$F_d = \alpha\frac{1}{2}\varepsilon_o N c V_d^2 \frac{t l_d}{(g_d - x_d)^2} \tag{4-3}$$

Although the force increases quadratically with a closing gap, the *usable* force is the force at the initial gap, which is also the minimum force. If this minimum force is too low for a given load, then the gap will not close.

4.2.3. Gear Teeth

To ensure that the clutch and shuttle gear teeth will always mesh, the gear period (one tooth + space) must be a multiple of the drive GCA stroke:

$$T_g = n \times Stroke \tag{4-4}$$

where *n* is the number of clutches that attach at unique times. For example, for a two-phase motor (two clutches) as shown in Fig. *4-3*, the gear period must be $2 \times stroke$ of the drive GCA. The minimum period is limited not only by the stroke and number of clutches but also by the lithography and etch aspect ratio. Small gear teeth are difficult to fabricate in thick SOI device layers. Larger gear teeth can be made by employing more clutches. The trade off is that more area is used for additional clutches and GCA arrays but the motor does not output more force.

4.2.4. Speed

The maximum frequency of operation for the GCA inchworm motors is limited by the time it takes to close (pull-in) and open (pull-out) the gap. Fig. 4-4 shows the clutch positions as a function of time for pull-in and pull-out. The timing diagram can be separated into four parts:

T_1 - Engage top clutch GCA
T_2 - Engage top drive GCA and disengage bottom drive and clutch GCA's
T_3 - Engage bottom Clutch
T_4 - Engage top drive GCA and disengage bottom drive and clutch GCA's

T_1 and T_3 are both determined by the pull-in times of the clutch arrays. T_2 and T_4 depend on the top drive pull-in time, bottom drive release time, or the bottom clutch release time. The longest of the three determines T_2 and T_4. Assuming both clutches and drives use indentical GCA arrays, then T_1=T_3 and T_2=T_4 and the cycle time is then given by:

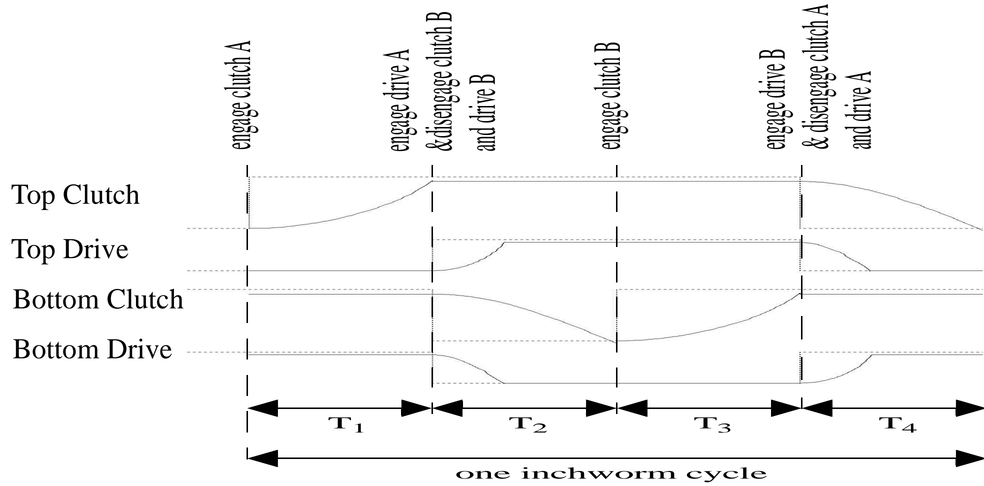

Fig. 4-4. Timing diagram for the inchworm motor through one cycle. The dotted lines indicate the drive signals and the solid lines indicate simulated responses of the beam positions.

$$T = 2(T_1 + T_2) \tag{4-5}$$

The analysis of the inchworm motors has shown that the minimum times, T_1 and T_2, depend on the clutch engagement (pull-in) and disengagement (pull-out) times, respectively. According to the model described in section 3.7, the pull-in time can be decreased by increasing the applied voltage as it is proportional to $1/V^2$ and the pull-out time can be decreased by increasing the spring constant as it is proportional to $\sqrt{1/k}$ according to the model.

4.2.5. Power

Power consumed is given by:

$$P_{in} = n(C_c + C_{pc})V_c f + m(C_d + C_{pd})V_d f \tag{4-6}$$

The variables are:

n - number of clutch GCA arrays
m - number of drive GCA arrays

C_c - total capacitance of clutch GCA array
C_d- total capacitance of drive GCA array
C_{pc} - total parasitic capacitance of clutch GCA array
C_{pd} - total parasitic capacitance of clutch GCA array
f - frequency of operation of clutch and drive GCA

The capacitances of the GCA arrays are a function of the gaps. To take the worst case, the maximum capacitances should be used in Eqn. 4-6, which occurs at the final (minimum) gap. The parasitic capacitances are between the bond pads and the substrate. To reduce parasitic capacitances, we use SOI wafers with the thickest buried oxide layer available (~2μm) and minimize the bond pad areas.

The usable output power is produced only by the drive GCA:

$$P_{out} = work \times f = force \times stroke \times freq = \frac{1}{2} N_d \varepsilon_o \frac{C_d}{g} V \times (g - g_s) \times f_d \tag{4-7}$$

The above equation uses C_d at the initial gap, which is the minimum C_d. This corresponds to the usable force described in Section 4.2.2.

The power efficiency is given by the ratio of Eqns. 4-6 and 4-7:

$$\frac{P_{out}}{P_{in}} = \frac{m \times \frac{1}{2} N_d \varepsilon_o \frac{C_d}{g} V \times (g - g_s) \times f_d}{n(C_c + C_{pc}) V_c f_c + m(C_d + C_{pd}) V_d f_d} \tag{4-8}$$

In the ideal case where C_d is much greater than all other capacitances and the stroke equals the initial gap (g_s=0), the power efficiency is 50%.

4.3 Scaling Effects

We next examine the effects of scaling on the electrostatic actuator. If the dimensions of the actuator are scaled isometrically, how do the relevant forces scale? Let all dimensions of the actuator be defined as a multiple of the critical dimension, λ.

A. Actuator Force

The dimensions of the GCA cancel out leaving the electrostatic force to be proportional to the voltage squared:

$$F_e = -\frac{1}{2}\varepsilon\frac{tl}{d^2}V^2 \propto V^2 \tag{4-9}$$

The maximum voltage we can apply is the failure voltage (Eqn. 3-29) scales linearly:

$$V_{pull-in} \sim \sqrt{\frac{0.28Ew^3d^3}{\varepsilon l^4\left(1+0.42\frac{d}{t}\right)}} \propto \lambda \tag{4-10}$$

Substituting Eqn. 4-10 back into eqn. 4-9, we find that force scales as:

$$F_e \propto \lambda^2 \tag{4-11}$$

4.3.6. Dissipative Forces

The actuator has to overcome the forces of gravity (weight of the robot), squeeze-film damping in the gap, and the restoring forces from the spring supports. The gravitational force scales as:

$$F_w = mass \times gravity \propto \lambda^3 \tag{4-12}$$

The squeeze-film damping forces scales as [76]:

$$F_{sq} = \frac{16\left(1-0.6\frac{t}{l}\right)t^3 l\mu}{d^3}\dot{d} \propto \lambda \tag{4-13}$$

where μ is the viscosity of air. The resistance of the spring supports is given by:

$$F_{sp} = k\frac{\Delta}{3} = \left(\frac{3EI}{l^3}\cdot\frac{\Delta}{3}\right) \propto \lambda^2 \tag{4-14}$$

Note that all of the dissipative forces scale favorably as λ decreases.

4.3.7. Output Power Density

The Output power density is given by:

$$\frac{P}{Vol} = \frac{Force \times Stroke \times Freq}{m^3} \tag{4-15}$$

The maximum frequency of operation is related to the resonant frequency of the GCA, which is approximated by:

$$f = \sqrt{\frac{k}{m}} = \sqrt{\frac{(3EI)/l^3}{m}} \propto \frac{1}{\lambda} \tag{4-16}$$

Substituting Eqn. 4-16 into Eqn. 4-15, we find that the power density increases inversely with decreasing dimensions:

$$\frac{P}{Vol} \propto \frac{\lambda^2 \times \lambda \times \frac{1}{\lambda}}{\lambda^3} = \frac{1}{\lambda} \tag{4-17}$$

Table lists the scaling effects discussed in this section. In summary, we find it favorable

Table 4-1: Scaling Effects

Unit	**Scaling**
Electrostatic Force	λ^2
Natural Frequency	$1/\lambda$
Power Density	$1/\lambda$
Gravitational Force	λ^3
Squeeze film damping Force	λ
Spring Restoring Force	λ^2

to scale down the size of the robot for higher power densities and lower dissipative forces.

4.4 Results

The first electrostatic inchworm motor was made in the MUMPs process (Fig. 4-5). It is cycled manually and displaced the shuttle by 28μm. The estimated force generated was 6.5μN with 35V. The force was estimated by the displacement of the shuttle's supporting springs. However, MUMPs motors suffered from substrate stiction, gap-stop stiction and electrostatic levitation [82]. These problems were addressed by going to a silicon-on-insulator (SOI) process. It is not clear why these problems disappeared when we switched to thicker single-crystal silicon. The surface roughness of the sidewalls due to a DRIE etch may decrease the adhesion force, or the adhesion force may be relatively inde-

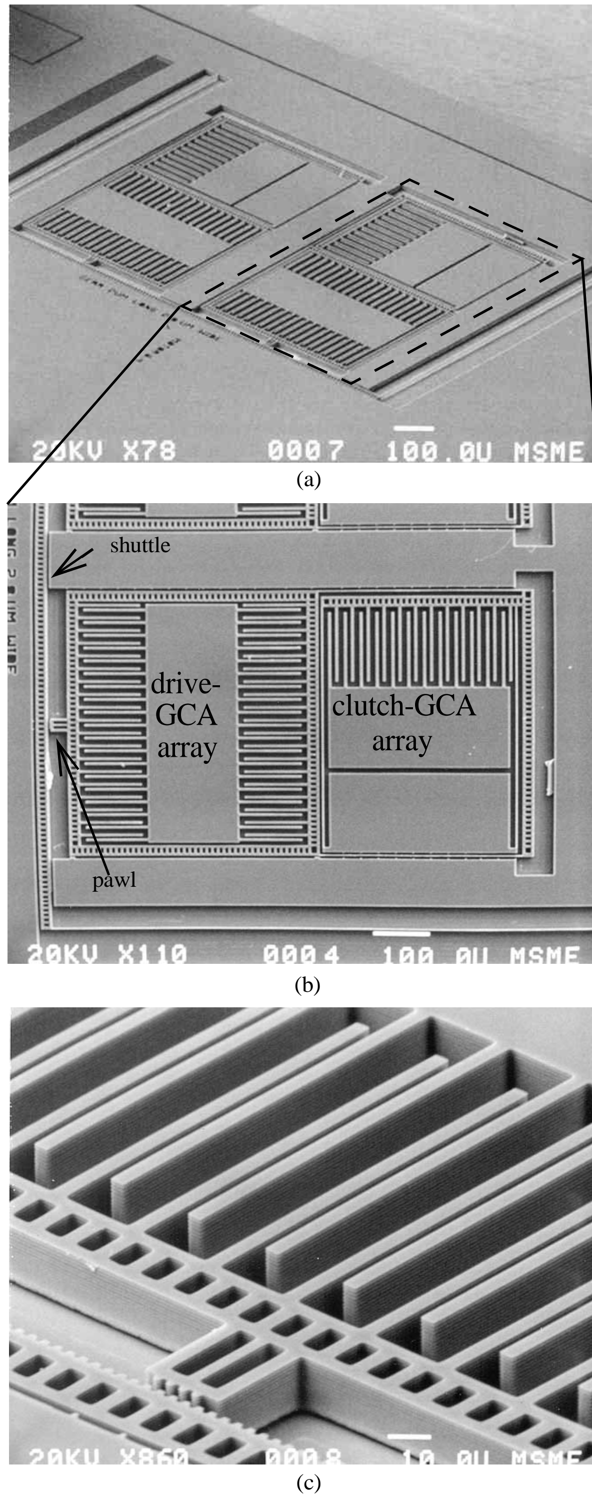

Fig. 4-5. (a) SEM of an inchworm motor fabricated on an SOI wafer. This motor displaced the shuttle by 48μm in 12 cycles. The displacement was limited only by this particular shuttle design (not force-limited). (b) SEM close-up of the x-y actuator and pawl. Note the arrays of gap-closing actuators.(c) SEM close-up of the clutch-GCA array, pawl, and shuttle.

pendent of film thickness, while the restoring force due to the support springs increases linearly with thickness.

Using the single mask, SOI process described in Section 3.9, large force, large displacement electrostatic inchworm motors were made. Fig. 4-5 shows the first working SOI motor made. The motor measured 1mm x 1.5mm in area and was fabricated on a 15µm-thick device layer. It displaced the shuttle by 36µm in 9 cycles and generated an estimated force of 6.5µN. Using an Atmel programmable microprocessor to control the motor, the motor operated at a maximum frequency of 300Hz or an average linear shuttle velocity of 1.2mm/sec in air. Seth Hollar improved upon that with a similar motor that displaced the shuttle by an average velocity of 4mm/sec. At higher speeds, the clutch begins to slip from the shuttle during the pulling step of the inchworm cycle. The theoretical frequency limit according to our model from Section 3.7 is 1.4kHz. Experimentally, we measured the minimum timing T_1 as 0.16 milliseconds and T_2 as 0.35 milliseconds. Our theoretical results predict 0.17 milliseconds and 0.18 milliseconds for T_1 and T_2, respectively. While the data matches well for T_1, T_2 differs by about a factor of two. Possible reasons for the extended cycle period could include extra time to disengage from the shuttle and actuator bouncing against gap stops. At this frequency, the power density of this motor is estimated at 190 W/m^3.

Another version of the motor with dimensions of 1.5mm x 2mm x 50µm was demonstrated with a travel of 80µm and exerted a force of over 50µN in *excess* of the friction it overcame. Fig. 4-6 shows the measured force vs. V_{pi} as the shuttle is displaced by 80µm in 2µm step sizes. During operation, the shuttle was displaced laterally by the force of the clutch and subsequently pushed against the silicon side wall on the other side of the shuttle

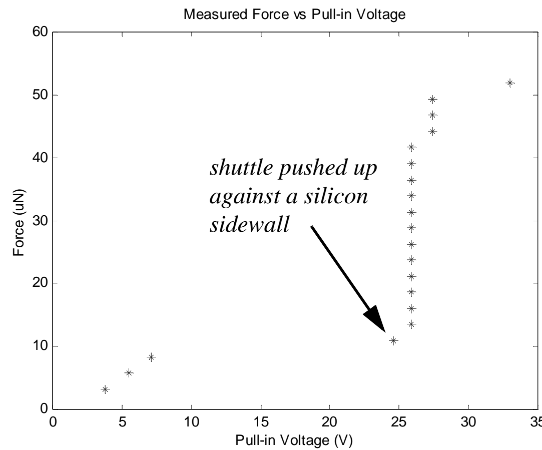

Fig. 4-6. Measured force vs. pull-in voltage as the shuttle is displaced by 80µm in 2µm increments. The discontinuity occurred when the shuttle was pushed laterally against a silicon sidewall by the clutch-GCA.

(Fig. 4-5c). The drive-GCA was nevertheless able to overcome the sidewall friction and pull the shuttle forward. The force generated, estimated by the *Vpi* required to displace the shuttle to 80µm was 260µN at 33V. The force density achieved is 87µN/mm^2. The theoretical upper limit of the force density at 33V and an aspect ratio of 25:1 is approximately 1mN/mm^2. This implies our motors have a fill factor of around 11% as the rest of the area is occupied by support structures, bonding pads, etc. Motors were operated for over 13.5 hours for a total of 23.6 million cycles without stiction.

Chapter 5. Mechanical Digital-To-Analog Converters

5.1 Introduction

Another actuator configuration is the mechanical digital-to-analog converter (DAC). The mechanical DAC takes n bits of digital electrical inputs and produces 2^n analog mechanical output states (displacement positions). With a digital input and a high output mechanical resistance, the mechanical DAC enjoys high immunity to input noise and a low loading effect. Such devices could provide reliable and accurate open-loop positioning in systems where sensors are difficult to implement, as in the case of microrobots.

Two different mechanical DAC designs were simultaneously realized in 1999 [84, 90]. Both designs used different mechanical devices to realize a R-2R ladder. The design by Toshiyoshi et al. [84] was a 4-bit DAC with comb drives. The design by Yeh et al. [90] was based on cascaded lever arms driven by thermal or electrostatic actuators. Both designs were immune to input noise but the lever arm design has a higher output resistance (low loading effect).

5.2 Design

The DAC uses a modular design that creates an n-bit DAC from n building blocks. The building block is a node that *mechanically* averages two input values (Fig. 5-1a). By cascading n building blocks where the output of one node is connected to one of the inputs of another node, an n-bit DAC is created (Fig. 5-1b). An electrical equivalent of this node is the two-resister circuit shown in Fig. 5-2. A cascade of this circuit creates the familiar

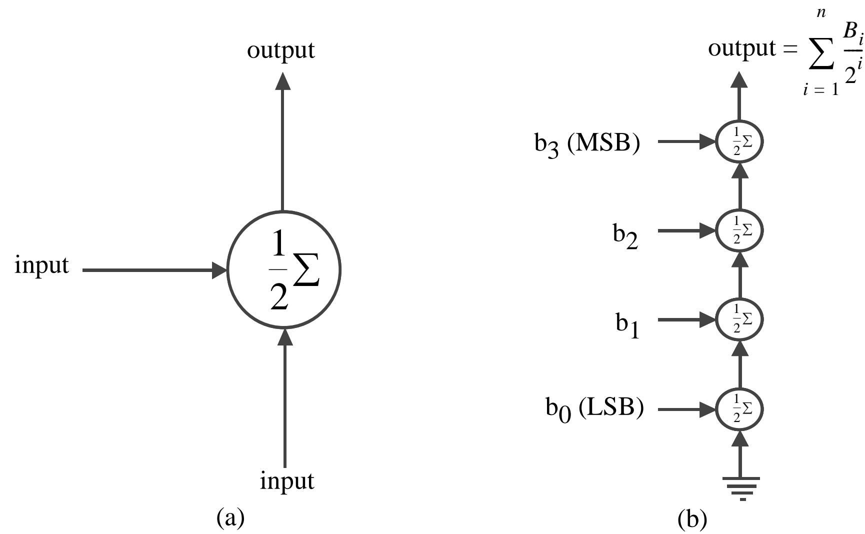

Fig. 5-1. The DAC concept. (a) An averaging node is the building block of the DAC. (b) By cascading four nodes, a 4-bit DAC is created. Note that one of the bottom node is grounded to make it the LSB.

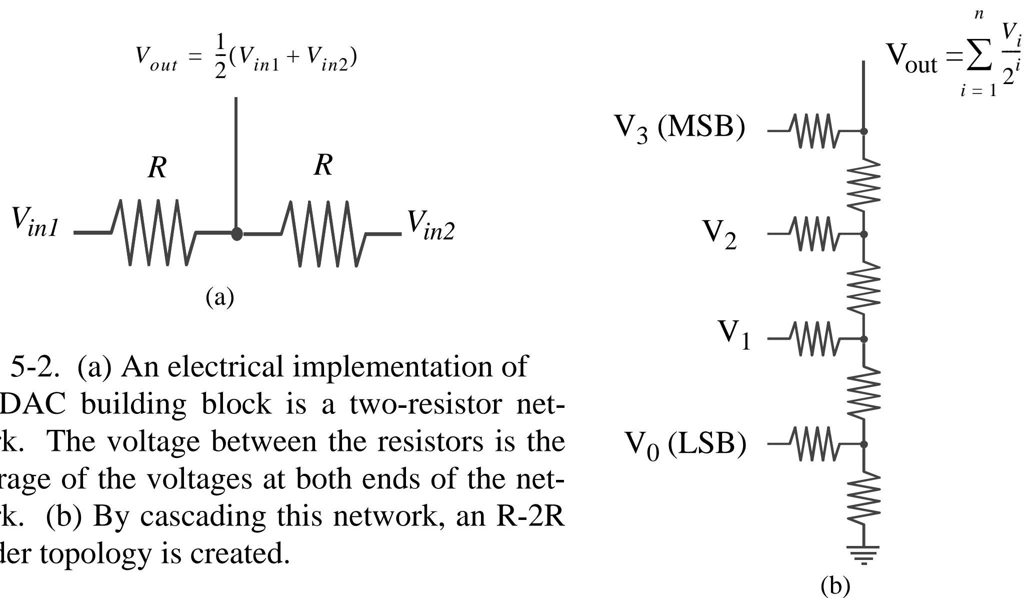

Fig. 5-2. (a) An electrical implementation of the DAC building block is a two-resistor network. The voltage between the resistors is the average of the voltages at both ends of the network. (b) By cascading this network, an R-2R ladder topology is created.

R-2R ladder topology used in simple electrical DAC circuits. A macro-mechanical example of this averaging node is a spring-supported pulley and rope, where the pulley deflection equals the average displacements of the two ends of the rope (Fig. 5-3).

A MEMS implementation of this averaging node, created from flexural and rigid beams, is shown in Fig. 5-4a. It is constructed from a spring-supported lever arm with two input beams and an output beam. This lever arm can rotate about either end when one of

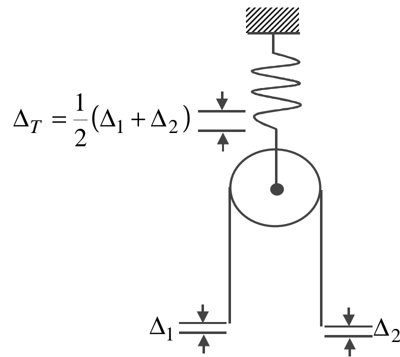

Fig. 5-3. A mechanical implementation of the DAC building block is a rope on a spring-supported pulley. The spring deflection is the average of the change in position of the two ends of the rope.

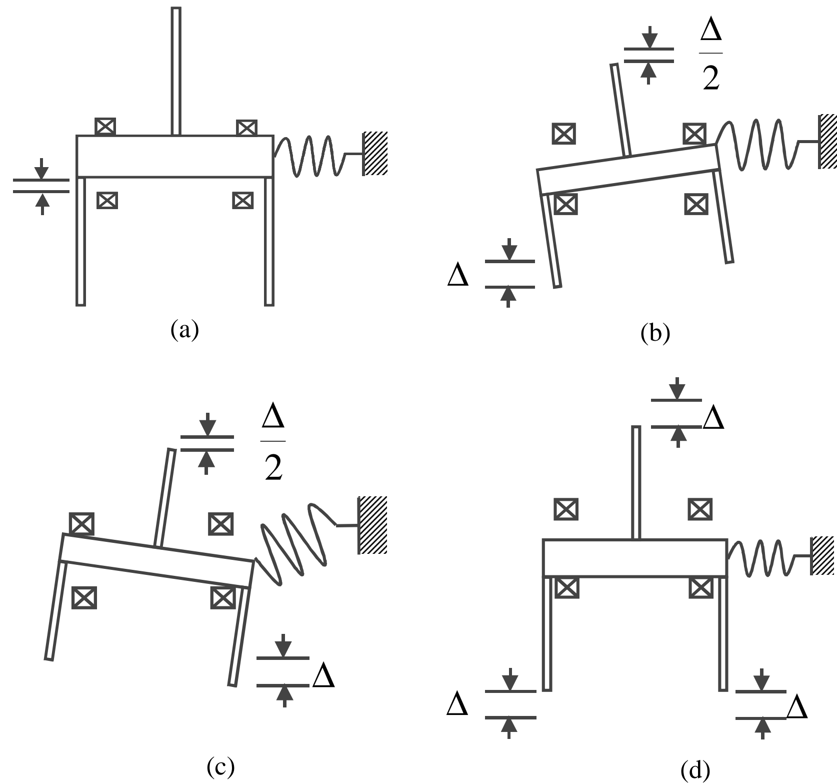

Fig. 5-4. A MEMS implementation of the DAC building block is a lever arm with two input beams and an output beam at mid length. The lever arm is supported by a spring at one end so that it is allowed to rotate about either end. The vertical deflection of the lever arm at the output beam is the average of the deflections at both ends of the lever arm. (a) Both inputs are low. (b) Left input is high and right input is low. (c) Right input is high and left input is low. (d) Both inputs are high.

the input beams is deflected (Fig. 5-5b,c) or translate when both of the input beams are deflected (Fig. 5-4d). The rotation at each end of the lever arm is limited by gap stops. Because the output beam is located in the middle of the lever arm, the vertical displacement at the output beam is the sum of half of the vertical displacements at either ends of the lever arm. Therefore, the lever arm works as the averaging node shown in Fig. 5-1a. Moreover, these lever arms can be cascaded in the method illustrated in Fig. 5-1b to create a DAC. An example of the topology for a 2-bit DAC is shown in Fig. 5-5. To create a

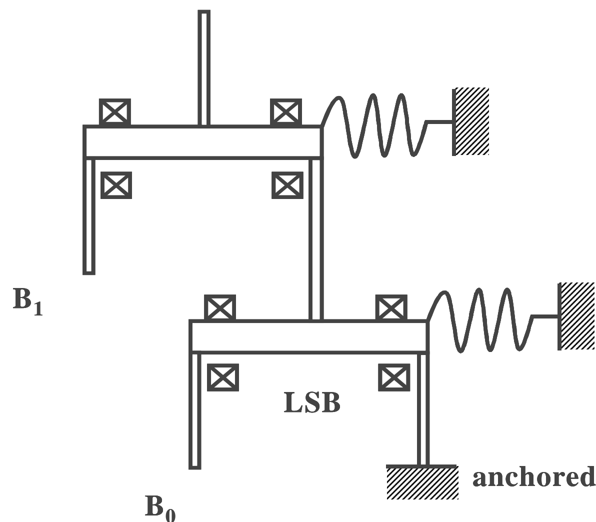

Fig. 5-5. Example of a 2-bit DAC created by cascading two lever arm stages.

DAC, one input beam of the lever arm is connected to the output beam of the previous stage and the remaining input beam is connected to an actuator which transforms electrical input signals into mechanical signals (force and displacement). At the LSB stage, the input beam not coupled to the actuator is anchored to the substrate (zero displacement). In the 2-bit DAC example shown in Fig. 5-5, the LSB input (B_o) is divided by two by the first lever arm and divided by two again by the 2nd lever arm (MSB) so that the displacement at the output stage is 1/4 of the input. The MSB input (B_1) is divided by two as it

goes through just one stage. The total vertical displacement at the output beam of this 2-bit DAC is the sum of one quarter of the LSB input and one half of the MSB input. With two input states (low and high) at each input, there are four (2^2) possible states for the output displacement. Thus, a 2-bit DAC is created. Similarly, we can create an n-bit DAC by cascading n lever arm stages in this fashion. The resulting output is then:

$$\Delta = \sum_{i=1}^{n} \frac{\delta_i}{2^i} \tag{5-1}$$

where δ_i is the input for the i-th bit.

5.2.1. Input Noise Immunity and Resolution

One of the key components of the lever arm implementation (Fig. 5-4) is the gap stop. These gap stops enable the DAC to be insensitive to the input noise and also define the resolution of the output. As shown in Fig. 5-4, there is one gap stop near each of the four corners of the lever arm. The two gap stops near the top corners of the lever arm are used during the low input state and the two gap stops near the bottom corners of the gap stop are used during the high input state. Ideally, the lever arm is always pushed against either the top gap stops or the bottom gap stops. The input voltage required to rotate the lever arm to a stop defines the threshold voltage for the digital high or low input. As long as the input voltage (signal and noise) exceeds the high threshold (V_{IH}) or is below the low threshold (V_{IL}), the lever arm would be pushed against a gap stop and output would not be affected by the input noise.

The resolution or step size of the output is defined by the gap between the gap stops and the lever arm and also by the number of bits:

$$LSB = \frac{Gap}{2^n} \tag{5-2}$$

where n is the number of bits in the DAC. Because the LSB is inversely proportional to 2^n, submicron resolution is easily achievable. For example, a 6-bit DAC with a gap of 6μm will have an LSB of only 90nm. The maximum number of bits is likely limited by non-uniformity in lithography and silicon etch of the gaps.

5.2.2. Low loading effect and force magnification

A major advantage of the lever arm implementation is the high output stiffness. Because the input signal acts on the ends of the lever arm and the output is taken at the middle of the lever arm, the force acting through one input beam is doubled at the output beam (Fig. 5-6). Conversely, an output force acting through the output beam is divided by

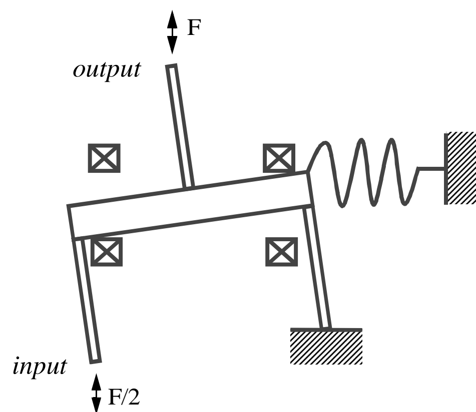

Fig. 5-6. Low loading effect of DAC's due to the lever arm force to torque-arm relation. Force is amplified going from input to output and, likewise, force is attenuated going from output to input. This attenuation of output loads gives rise to a low loading effect.

two as seen from one of the input beams (Fig. 5-6). In an n-bit DAC (which would have n building blocks), the output force would be divided by two at each stage as it travels down from the MSB to the LSB. For example, an output load of 1μN would be reduced to 0.5μN at the MSB input beam and to 0.25μN at the next input beam. Because of this attenuation, the loading effect is minimized.

5.2.3. Actuation

This mechanical DAC design can use various input bit actuators. We have demonstrated both thermal and electrostatic DAC's. The thermal and electrostatic designs are shown in Figs. 5-7 and 5-8, respectively. In both designs, actuator arrays are coupled to the input beams of the DAC.

The thermal actuator arrays can operate at frequencies of more than 1kHz but consume 30mW per array with a 6µm displacement. These actuators are driven at 5V. A

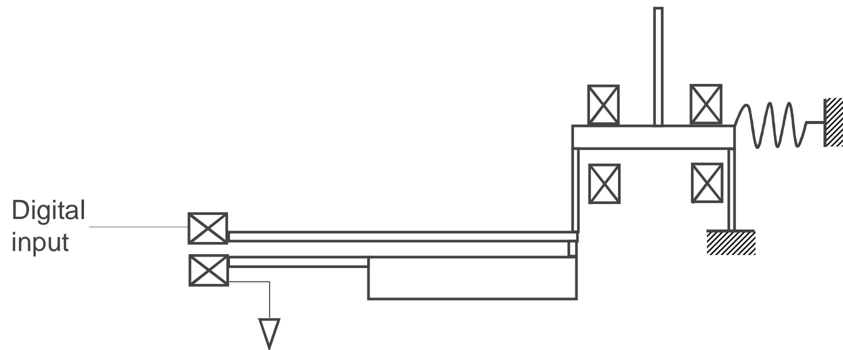

Fig. 5-7. Diagram of a DAC using thermal actuators.

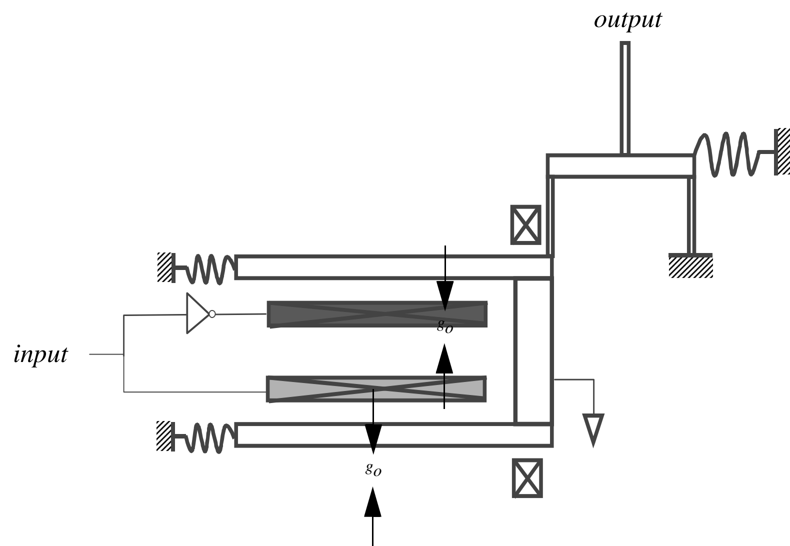

Fig. 5-8. Diagram of a DAC using electrostatic gap-closing actuators.

drawback of these actuators is the sensitivity to input noise when the bits are low. This is because in the low state, the thermal actuators are not pushed against a stop.

The electrostatic GCA's do not suffer from input noise in the low input state. In this design, two opposing GCA arrays are coupled to the input beam (Fig. 5-8). The input to one GCA array is inverted to the other so that only one GCA array per input beam is turned on while the other is turned off. The threshold voltage for a high state, V_{IH}, must be greater than V_{pi} for $2g_o$. The GCA gap stops also double as the DAC gap stop and the input is always pushed against the GCA gap stop of the activated GCA array. The drawback of this design is the need for complementary inputs and potentially higher voltage of operation.

5.3 Results

To date, 4- and 6-bit thermally-driven DAC's using the MCNC MUMPs foundry process and 4-bit electrostatically-driven DAC's from the GCA SOI process (described in Chapter 3) have been demonstrated. Fig. 5-9 shows an SEM pictures of a MUMPs and

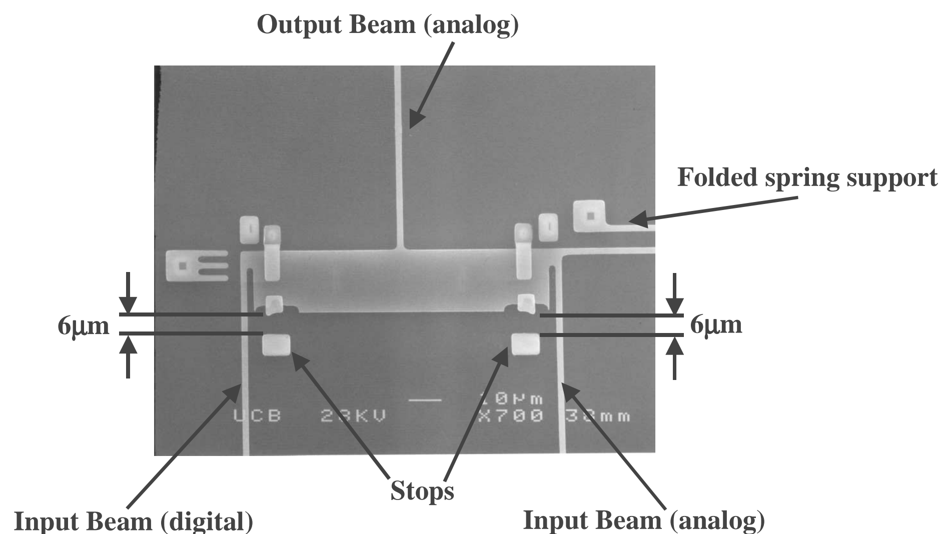

Fig. 5-9. SEM picture of a lever arm fabricated from the MUMPs process. The lever arm is 20µm wide and 100µm long with two input beams on either end and an output beam in the middle. There are gap stops to limit the rotation of the lever arm to 6µm.

SOI lever arm with two input beams, an output beam, spring support, and gap stops. Fig. 5-10 shows an SEM picture of a 4-bit thermally-driven DAC made from 4 cascaded lever

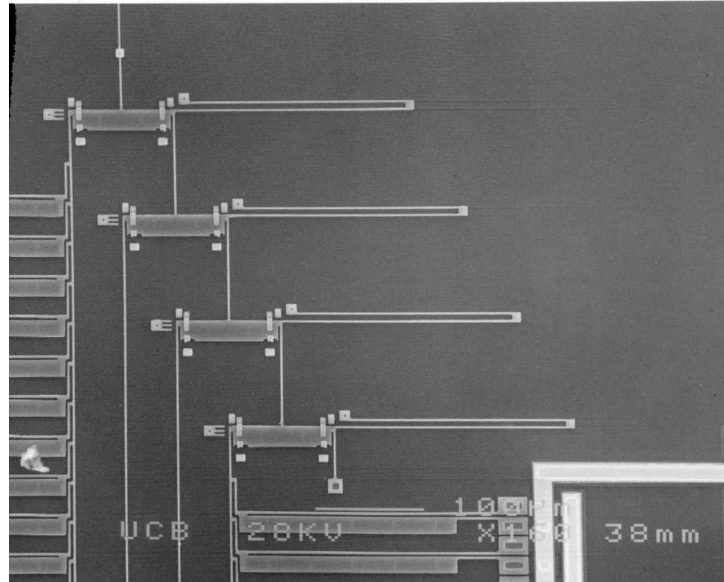

Fig. 5-10. SEM picture of four cascaded lever arms made in the MUMPs process.

arms. From equation 5-1, the displacement from an *n*-bit DAC at the output beam is given by:

$$\Delta = gap \sum_{i=1}^{n} \frac{1}{2^i} \tag{5-3}$$

where the *gap* is defined by the distance from the gap stop to the lever arm. A gap of 6µm was chosen based on the travel of the thermal actuators. This gives us an output resolution of 0.37µm for the 4-bit version and 90nm for the 6-bit version.

Fig. 5-11, shows an SEM of a 4-bit DAC with GCA arrays. The DAC was fabricated in a 50µm-thick silicon layer and the GCA arrays have a V_{pi} of 12V. The gap was 10µm which gave the 4-bit DAC an output resolution of 0.6µm.

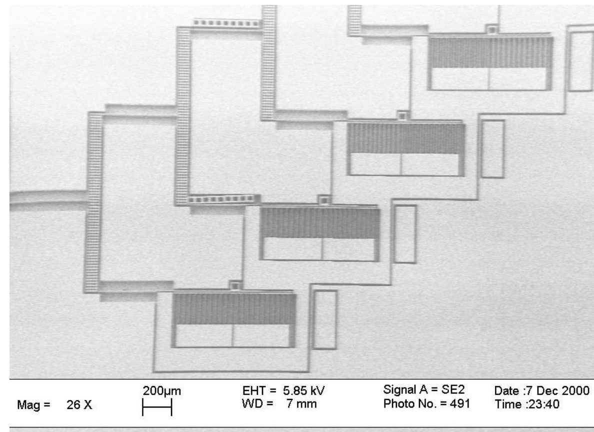

Fig. 5-11. SEM of 4-bit DAC with electrostatic gap-closing actuator arrays.

5.3.1. Transfer Function

We used optical methods to accurately measure the output of the 6-bit thermally-driven DAC. A hinged micromirror was coupled to the output beam of the DAC as shown in Fig. . When the output beam displaces, the hinged mirror rotates. By projecting a HeNe laser onto the mirror and measuring the reflected beam position with a position-sensitive diode (PSD) as shown in Fig. 5-13, we were able to characterize the dynamics of the DAC/micromirror system. A 6-bit counter was used to cycle the 6-bit DAC through all 64 output states. Power MOSFET's were used to provide the current needed by the thermal actuators. During testing, the mirror hinges have been observed to slip along the surface of the substrate, producing non-repeatable beam positions but when the input signal slew rate was decreased by an RC network, the hinges stopped slipping.

Fig. 5-14 shows the output beam displacement (normalized to full-scale) of a 6-bit DAC cycling through its 64 output states. We observed 8 output transitions which exhibited a marked delay in settling time (seen as downward spikes in the plot). These delays occur whenever the three lower bits switch from high to low and the 4th-bit from low to

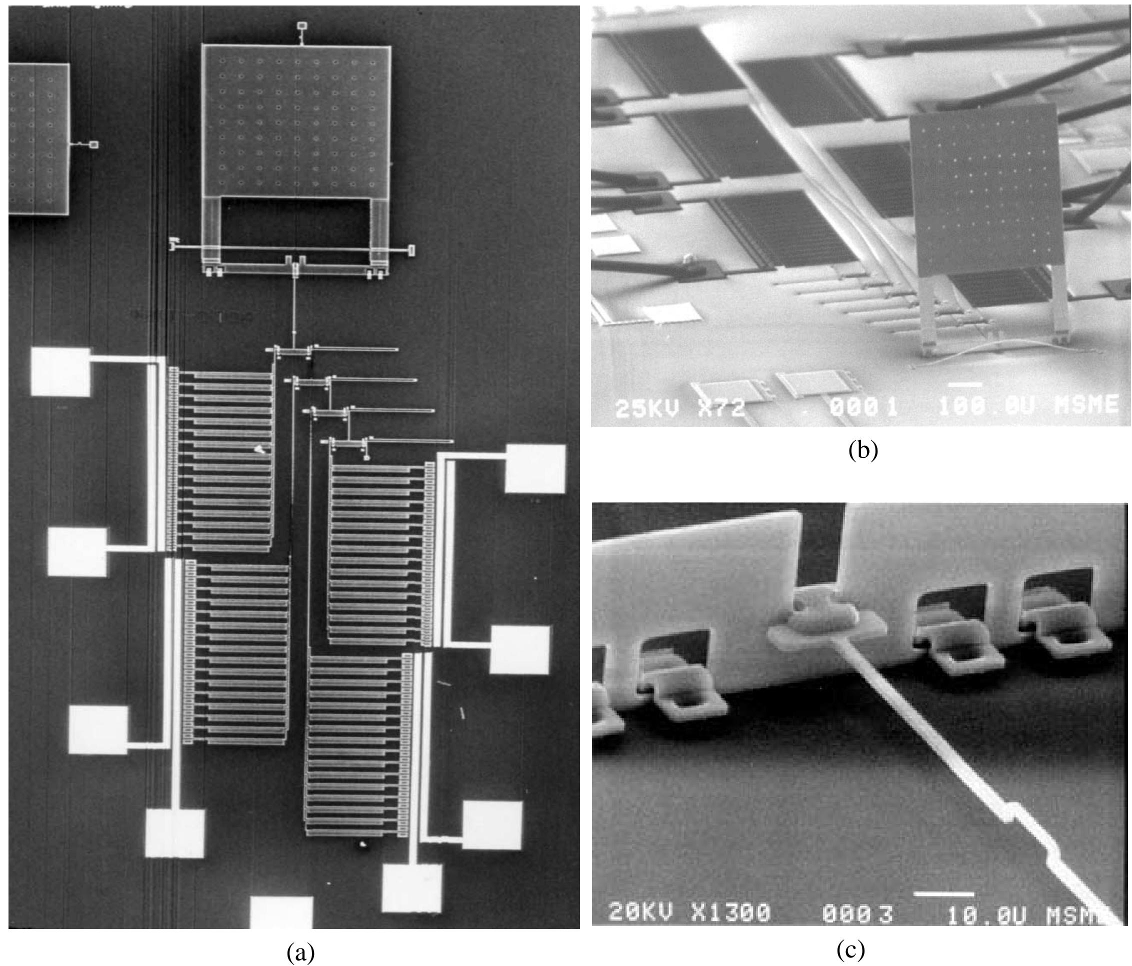

Fig. 5-12. DAC-driven mirrors. (a) SEM picture of a 4-bit DAC coupled with an unassembled hinged mirror. (b) SEM picture of a 6-bit DAC driving an assembled hinged micromirror. As the DAC output state changes, the mirror rotates. (c) A close up of a mirror coupling mechanism (courtesy of Matt Last).

high. Fig. 5-14 shows a plot of the reflected laser beam position through 19 cycles. Note the repeatability of the output. Fig. 5-15 shows the output position of each position averaged from 19 cycles. The straight line indicates the ideal output position. The output increases monotonically with an integral nonlinearity (INL) of ±3.2 LSB and a differential non-linearity (DNL) of ±0.7 LSB. The INL is defined as the maximum deviation of the output position from the ideal position and the DNL is defined as the maximum deviation of the state-to-state increment from the ideal increment of one LSB. Since the LSB of this

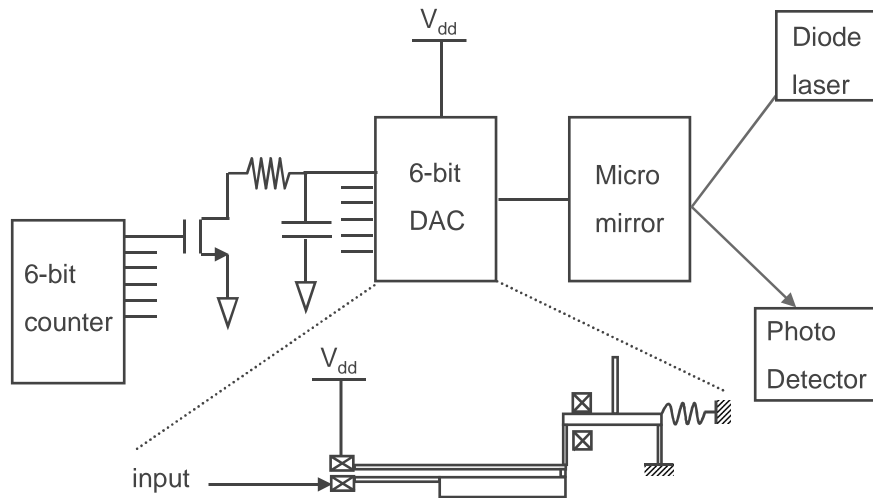

Fig. 5-13. Diagram of the optical method of characterization. A HeNe laser beam is deflected off of the DAC-driven micromirror and the position of the beam is detected on a photo-sensitive diode.

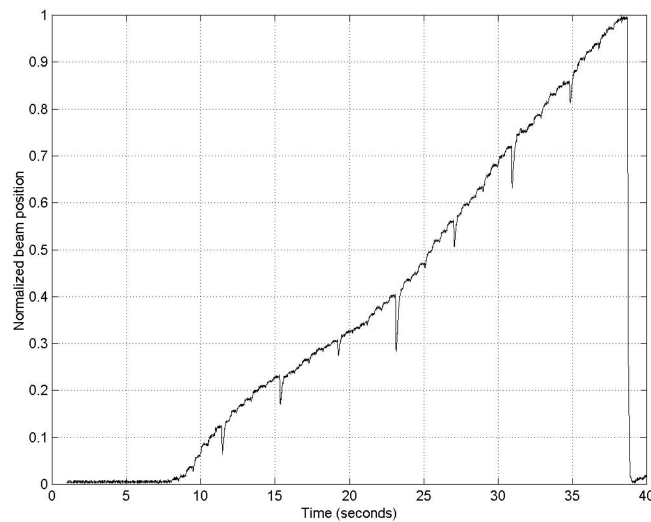

Fig. 5-14. Output beam position of the 6-bit DAC. The position is normalized to full-scale output.

6-bit DAC is only 90nm, the INL is less than 300nm at worst case. Fig. 5-15 shows the standard deviation of the output positions from ideality from 19 cycles. This demonstrates the output of the DAC is repeatable to submicron accuracy.

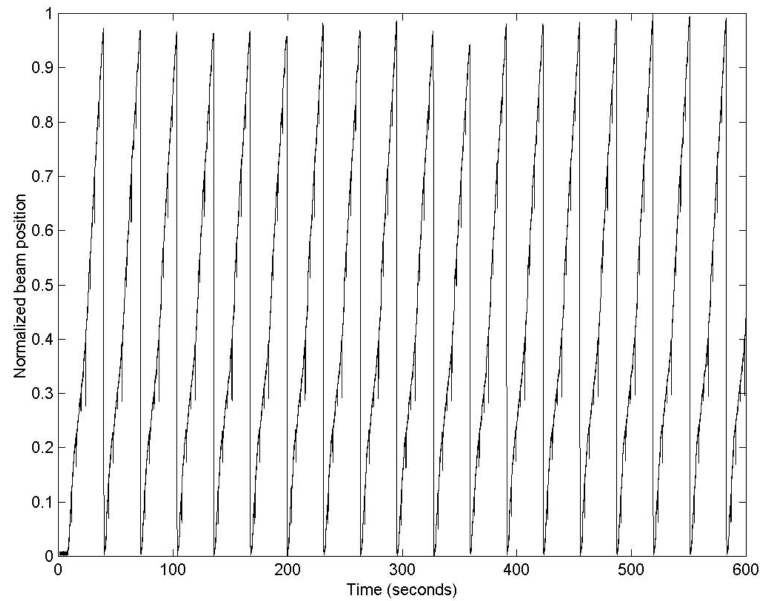

Fig. 5-15. Output beam position of the 6-bit DAC through 19 cycles.

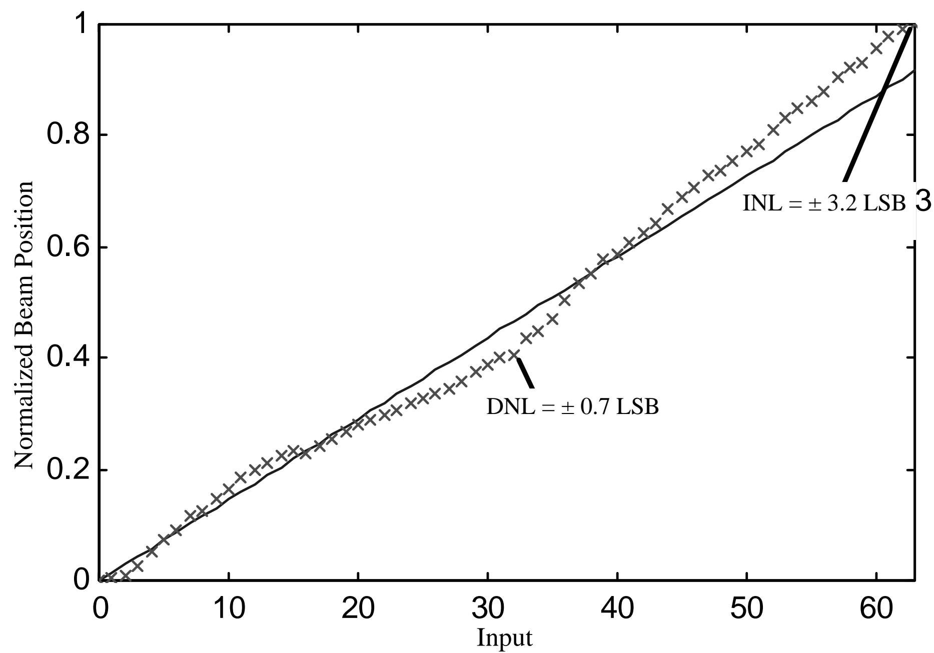

Fig. 5-15. The average beam position of each output state averaged through the 19 cycles shown in Fig. 5-15. The straight line shows the ideal output.

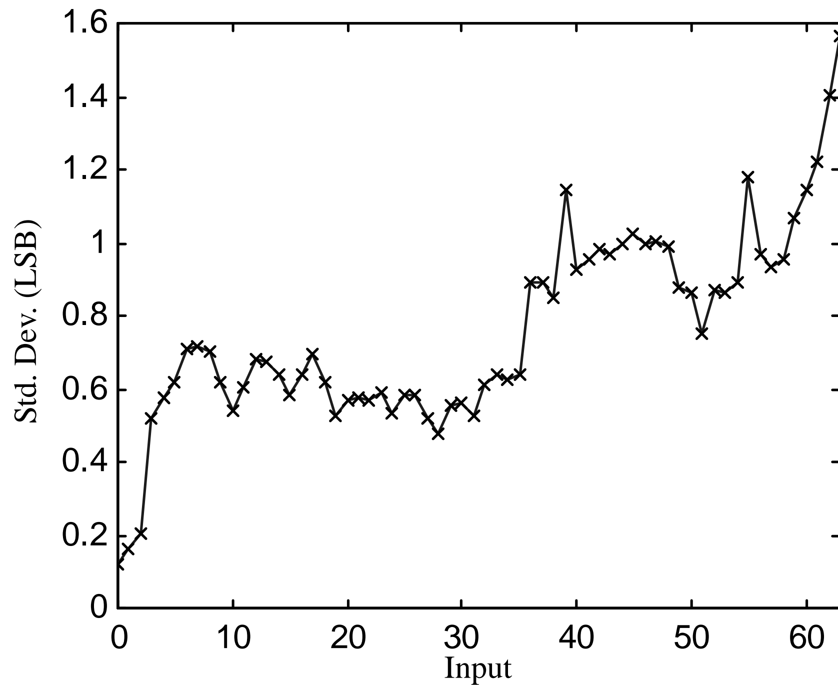

Fig. 5-16. The standard deviation of the beam positions through the 19 cycles shown in Fig. 5-15.

The output of the electrostatically-driven DAC was measured visually via a microscope/video-capture/matlab set-up. The visual resolution using the maximum resolution of 100x is 0.1µm. The measured output is shown in Fig. 5-17. The INL is ±0.38 LSB and the DNL is ±0.35 LSB. This DAC measured 3.8mm x 3.6mm.

5.3.2. Nonlinearity

The likely sources of positioning error (nonlinearity) are:

- mismatch between gaps due to process variations
- non-ideal pivots at the lever arms
- input beam bending

Gap variations would produce nonlinearity. The gaps in a DAC will be slightly different due to variations in the process. For example, gaps may be slightly different in size on the mask or the amount of undercutting of the silicon trenches would vary due to

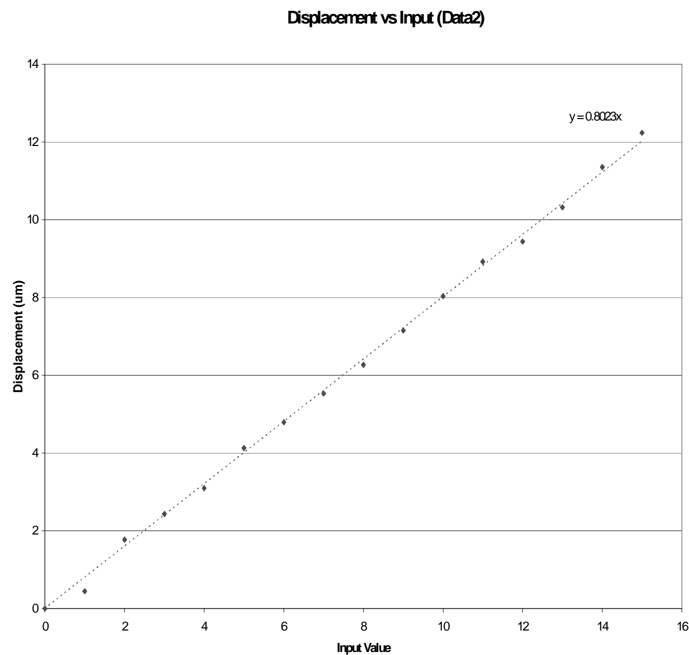

Fig. 5-17. Output of 4-bit electrostatically-driven DAC.

etch loading effects or localized silicon temperature differences. In a deep etched (Bosch Process) process used in the SOI process, the sidewalls will be scalloped (Fig. 5-18) and the contact point when two beams contact uncertain. In addition, the sidewall angles also determine the actual gap.

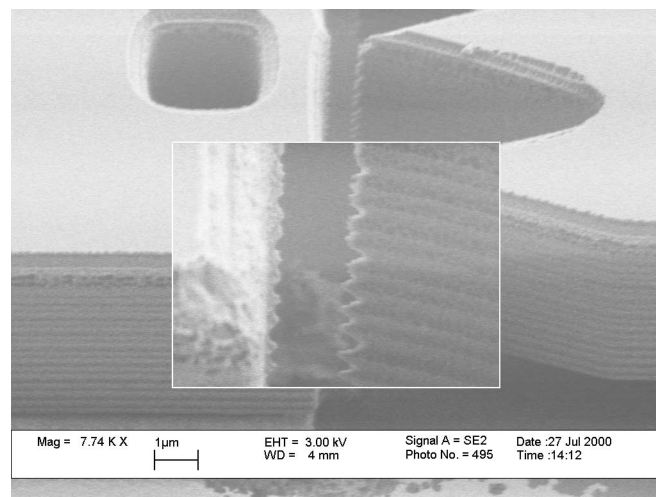

Fig. 5-18. SEM of STS etched silicon. Note the scalloped sidewalls. Courtesy of Veljko Milanovic.

Another likely source comes from the non-ideal lever arm supports. The ends of an ideal DAC lever arm should pivot when one of the lever arm inputs is high and translate when both lever arm inputs are high (Fig. 5-4). This requires a lever arm support which allows for pure pivots *or* translation depending on the input. In practice, the pivot is provided by one of the input beams which bends to accommodate the rotation in the lever arm. The bending has a rotational and a translational component and the translation becomes an unintended input. This unintended input causes the output to be higher than ideal (Fig. 5-19).

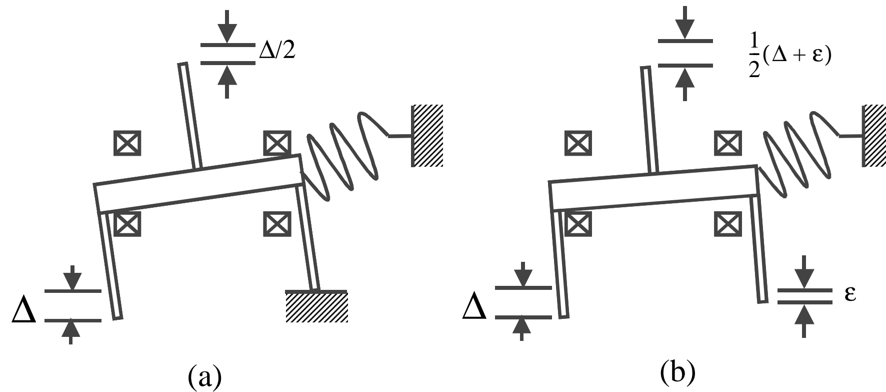

Fig. 5-19. Nonlinearity due to the finite mechanical resistance of the input beams. A force is distributed along the lever arm as the left input is switched on. (a) In an ideal DAC, there would be infinite mechanical resistance at the right input beam so deflection at the right end of the lever arm is zero. (b) In reality, the mechanical resistance as seem from the right input beam is finite so there is an additional deflection at the right input beam causing nonlinearity at the output.

Input beam bending is another likely source of nonlinearity. When the input to a lever arm is high, the lever arm pivots on the output beam of the preceding stage. The input force then is transmitted along the output beam of the preceding stage to the input beams. If the input beam bends, then this becomes an unintended input, which adds to the nonlinearity of the output.

Input beam bending will always cause the output to be higher than expected. The MUMPs DAC's probably suffer from this bending as evidenced in its measured output in Fig. 5-15. The SOI DAC's have stiffer input beams and show good linearity but probably have high gap variations due to the scalloped sidewalls (Fig. 5-18).

5.3.3. Maximum Resolution

The maximum resolution is limited by the nonlinearity of the DAC system. If we define the average of the gaps in the lever arm as $\bar{x}$, then the error at the output from all the nonlinearities can be calculated as:

$$\varepsilon = \sum_{i=1}^{n} \frac{(x_i - \bar{x})}{2^i} \cdot B_i \tag{5-4}$$

where x_i is the gap at the *i*-th lever arm stage and B_i is the digital input value (1 or 0) at the *i*-th bit.

If we define the maximum allowable error to be DNL < 1 LSB, then the error at any bit must be less than 1 LSB:

$$\frac{x_i - \bar{x}}{2^i} \equiv \frac{\delta_i}{2^i} < \frac{\bar{x}}{2^n} \tag{5-5}$$

where n is the total number of bits in the DAC. From the above equation, it is apparent that the worst error occurs at the MSB when i=1. Solving the above equation for the maximum number of bits possible, we get:

$$n = \frac{\log\bar{x} - \log\delta + \log 2}{\log 2} \tag{5-6}$$

For a gap ($\bar{x}$) of 6µm, an error (δ) of 0.01µm, the maximum number of bits would be 10.

5.3.4. Maximum Operating Frequency

The DAC conversion speed is limited by the actuator speed. For the electrostatic gap-closing actuator, the speed is limited by the pull-in and release times as described in Chapter 3. For the mechanically-driven DAC, which are fabricated in the MUMPs pro-

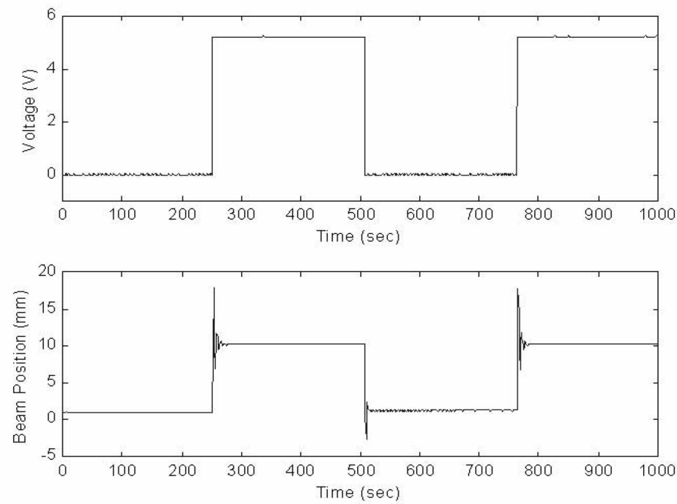

Fig. 5-20. Step Response of 4-bit DAC/mirror. (a) 5V, 0.2Hz square wave input. (b) Step response.

cess, we measured the resonant frequency of a 4-bit DAC/mirror system by observing the ringing in the step response of the DAC. The optical test set-up was described in Section 5.3.1. The ringing frequency in the output indicates the mechanical resonance of the system is at 390Hz (Fig. 5-20). Since the thermal actuators can be operated at 1kHz [22], the DAC/mirror system's resonant frequency is limited by the effective mass of the micro mirror and the mechanical compliance of the micro mirror and the DAC system.

CHAPTER 6. SYSTEM INTEGRATION

6.1 Introduction

Integrating a system of MEMS, optics, power, and electronics components is the next challenge in this microrobotics project. Ideally, the different microrobot components would be fabricated on the same process that would have optimal structural and electrical properties. There have been many efforts in the last decade to integrate microstructures and electronics in the same process. Some example are [11, 29, 73]. However, since there is no single process that can build all of the microrobotic components yet, both microrobotics and related Smart Dust components would be fabricated separately and assembled at the end. We are still in the early stages of this area and so in this section, an assembly method will be proposed and the power budget of these components would be considered in this chapter.

6.2 Proposed Assembly Process

A diagram of a leg, motors, controller and power source is shown in Fig. 6-1. Table 6-1 shows the different processes involved in making the components. The legs

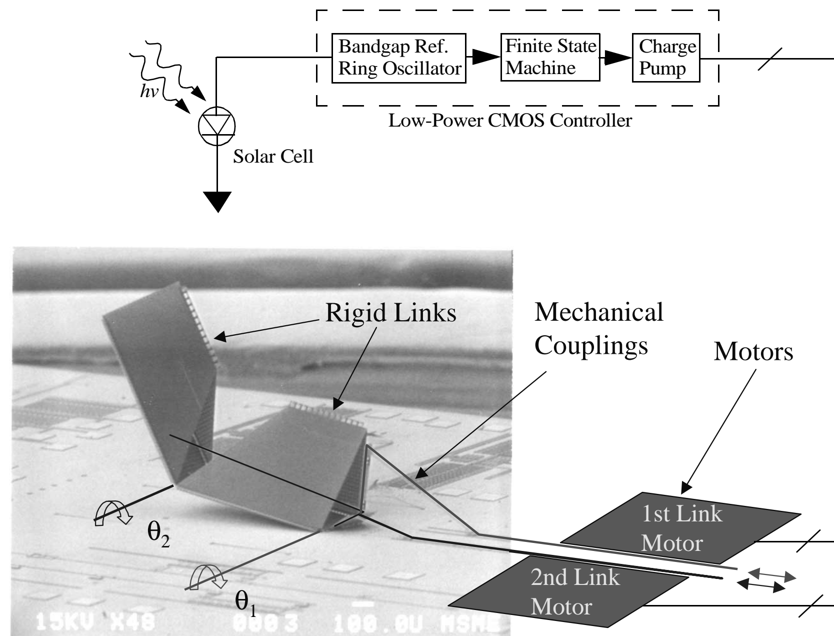

Fig. 6-1. System diagram. Leg is upside down in the SEM photo.

Table 6-1: Processes used for current Components

Component	Process
Articulated Legs	MUMPs
Mechanical Coupling	MUMPs
Motors	in-house SOI motor process
Solar Cells (Smart Dust)	in-house SOI solar cell process
Controller (Smart Dust)	National Semiconductors Jupiter Process (0.25µm CMOS)
Motor buffers (Smart Dust)	in-house SOI solar cell process

(including mechanical coupling), described in Chapter 2 and 3, were fabricated in the commercial MUMPs process with two polysilicon structural layers. MUMPs was chosen because it was a readily available process which allows the creation of hinged structures and sliders. The electrostatic inchworm motors, described in Chapter 4, were fabricated

in-house with Silicon-On-Insulator (SOI) wafers and a deep-reactive-ion-etch (DRIE) Bosch Process.

6.2.1. Proposed assembly process for legs and motors

To actuate the robotic links on the legs, motors need to be connected to sliders (part of the mechanical coupling) on the substrate. The proposed method is by gold bump flip-chip transfer [58] and the process is shown in Fig. 6-2. Transfers would be between a

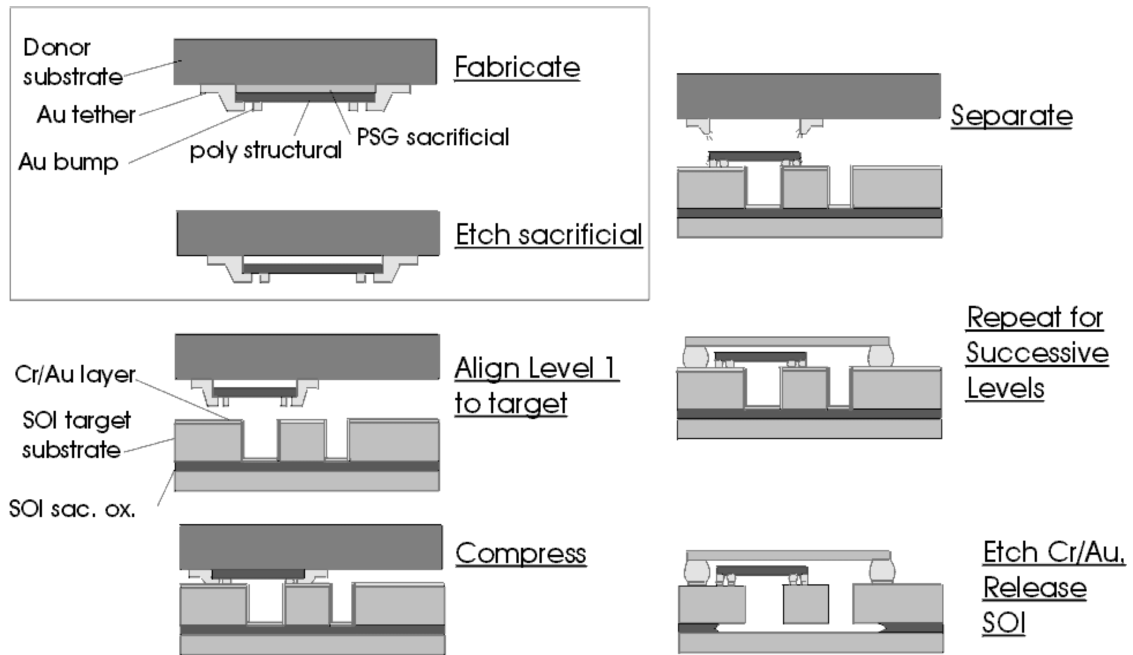

Figure 1: Basic Process

Fig. 6-2. Gold bump flip-chip process flow. (From Maharbiz [58]).

SOI chip with motors (donor) and a matching MUMPs chip with articulated legs and mechanical coupling (target). The end result would be SOI motors and SOI shuttles attached to sliders (part of the mechanical coupling) on the MUMPs chip as shown in Fig. 6-3. The alignment error between the donor and target sites is typically ~5µm which should be good enough since the motor and the slider do not need to be perfectly aligned. A proposed process flow to achieve the transfer is shown in Fig. 6-4. The SOI motors are

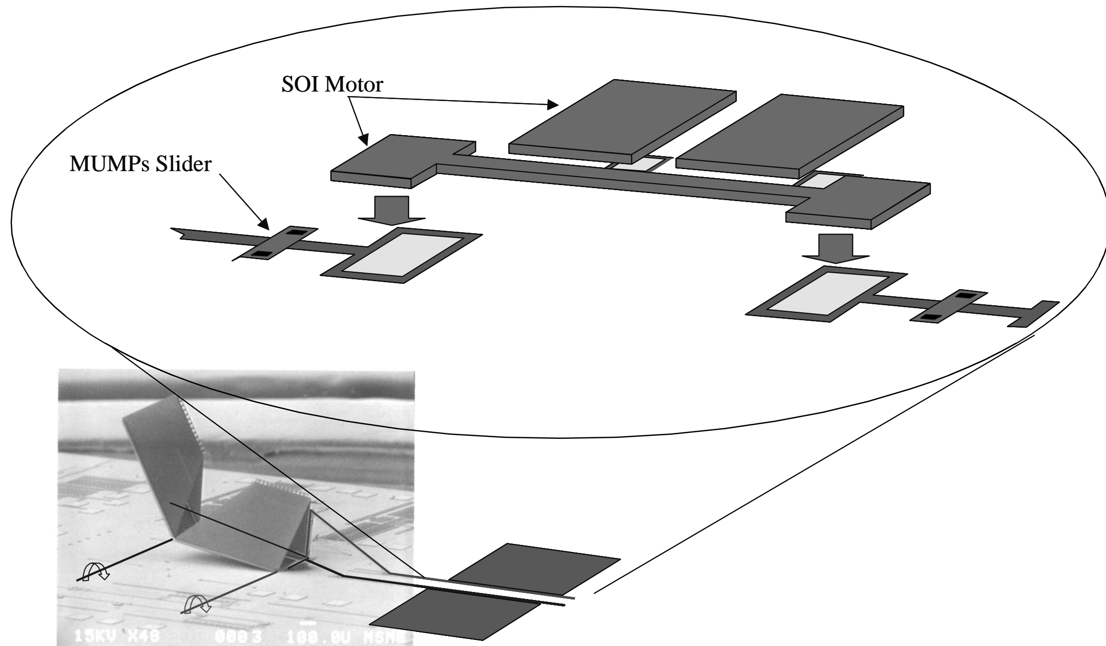

Fig. 6-3. Proposed method of connecting SOI motors to MUMPs mechanical couplings. SOI motors are patterned with gold bumps on the binding sites and flip-chip bonded to the gold pads on the MUMPs sliders.

fabricated as described in Chapter 3. The SOI wafer is planarized using a spin-on-glass technique [88]. Chromium (100A) and gold (1000A) is then evaporated on the SOI wafer as a seed layer. For improved adhesion, the two layers are evaporated one after another without breaking vacuum. An 8µm-thick Shipley's SJR5470 positive photoresist (PR) is spun-on and patterned with the gold bump mask. The SOI wafer is then electroplated in a gold solution (Technics TG25-E) to form gold bumps in the PR trenches. The photoresist is then removed in a 90º PRS-2000 bath. The SOI wafer is diced and motor structures are released in a 49% hydrofluoric (HF) acid oxide etch. At this point, the motors are connected to the SOI chip only by gold bumps that also act as tethers. On a parallel process, the MUMPs chip would be mounted on a handle wafer by wax and thinned down to the minimum thickness necessary to support the other robotics components and also withstand the assembly steps. It is not clear at this point what the thickness should be but a

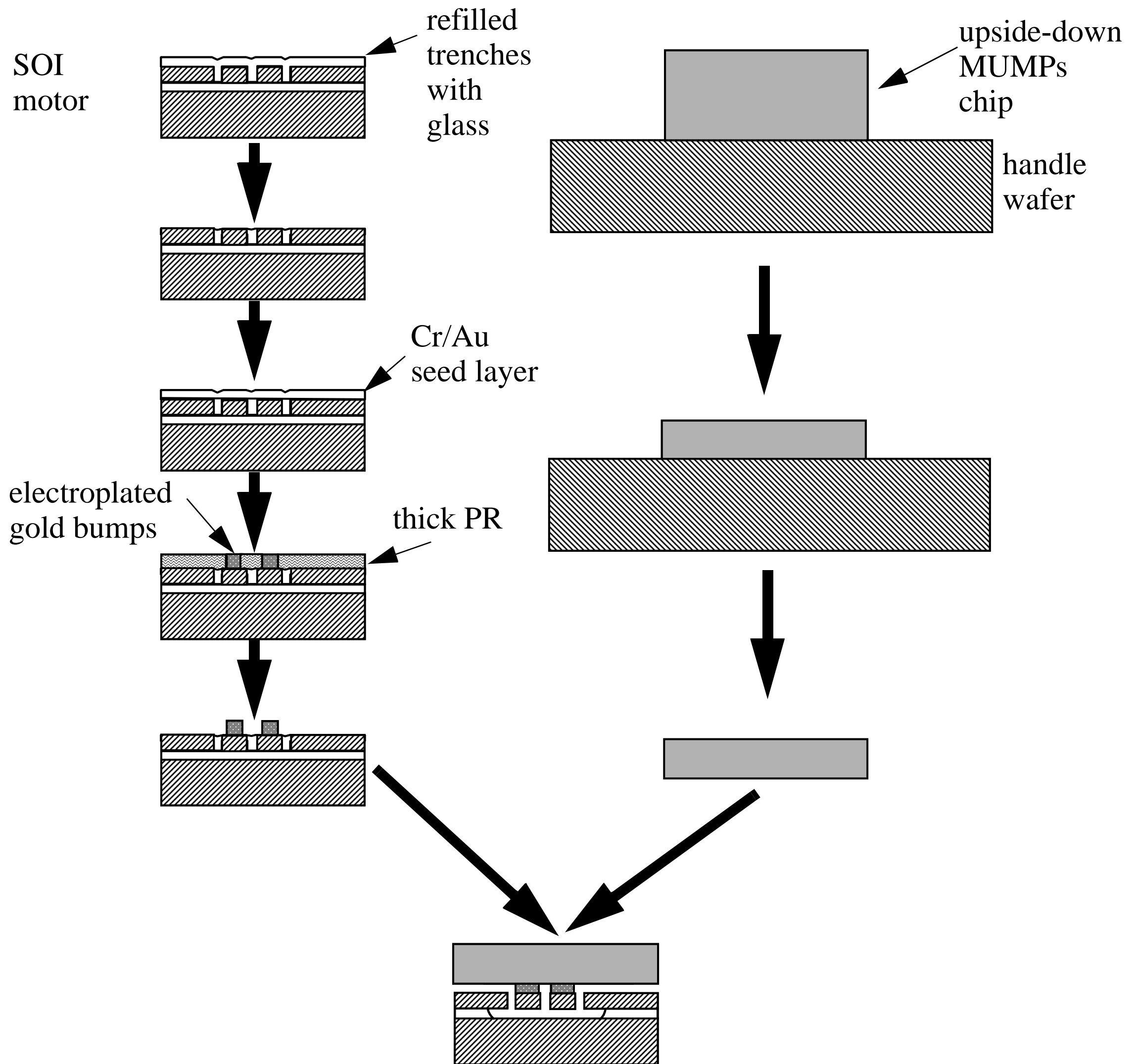

Fig. 6-4. Proposed assembly process to connect SOI motors to MUMPs mechanical couplings using flip-chip bonding. To reduce the mass of the robot, the MUMPs chip is thinned down.

thickness of ~100μm should be possible. Nguyen *et. al.* [63] reported electroplating 70μm of nickel on top of a MUMPs chip as mechanical support and then removing the entire MUMPs substrate by mechanical lapping and XeF_2 vapor-phase silicon etch [17]. This reduction of mass should be repeated on the solar array chip as a way to reduce the load on the motors. After the MUMPs chip is thinned down, the handle wafer would be

removed in an acetone bath. Finally, motors are transferred to the MUMPS chip via flip-chip bonding.

The chief challenge this process is planarizing SOI trenches that are tens of microns. Electroplating requires a conductive seed layer to work. A planarized surface is required to deposit a seed layer that is conductive throughout the entire wafer surface whereas a non planar surface with trenches or partially filled trenches would cause poor coverage and electrically isolate trench enclosures such as those used to define SOI devices. Though planarizing deep trenches is a challenge, progress has been made recently. Yeh et al. describes a clever technique of creating closely-spaced silicon beams that can be oxidized to create a large planar oxide area that can be removed with hydrofluoric acid [89]. However, this technique would also oxidize the 2µm-wide gear teeth patterns in the motors. Another method by Yasseen *et. al.* uses a custom-made spin-on-glass that can refill up to 20 microns [88]. It is not clear what the limit is on the refillable depth. Fig. 6-5 shows some polysilicon structures deposited over 10µm-deep silicon trenches, planarized by a similar technique [38].

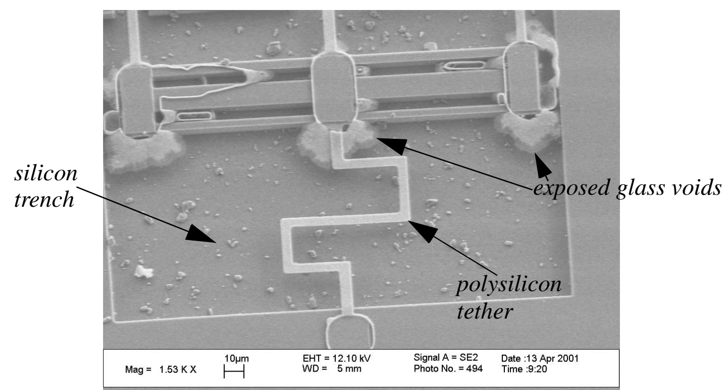

Fig. 6-5. SEM of a polysilicon serpentine beam deposited over a 10µm-deep silicon trench that was planarized through glass-refill and then chemical-mechanical polishing (CMP). Voids in the glass that were exposed after CMP were coated by the conformally-deposited LPCVD polysilicon. Courtesy of Seth Hollar.

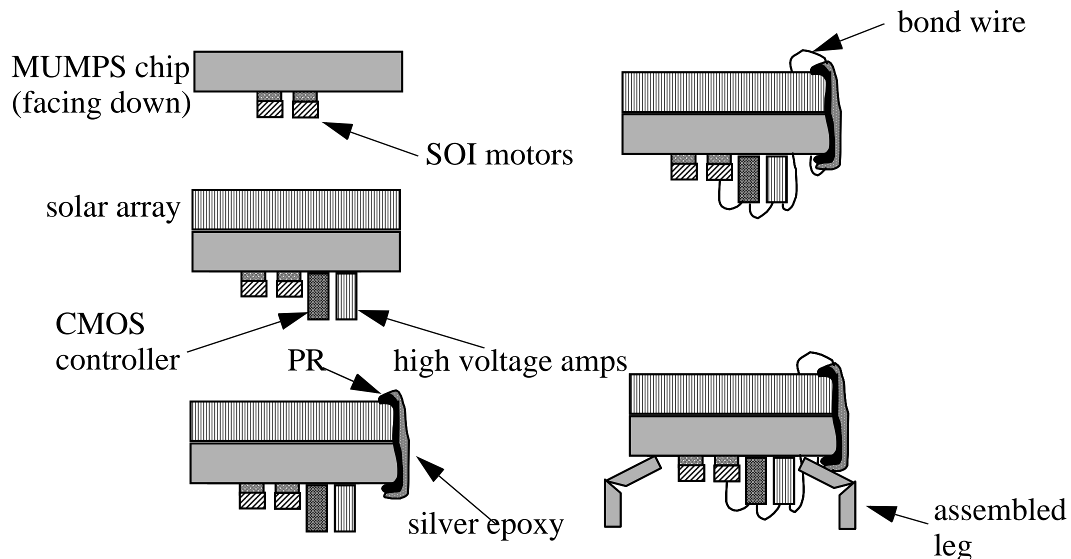

Fig. 6-6. Proposed process for assembly of the controller, solar cell, articulated legs and micromotors. The solar array, CMOS controller and high voltage amplifier (from the solar cell process) are mounted on the MUMPS chip using silver epoxy. The MUMPs and solar array substrates are shorted together and act as virtual electrical ground. PR would be painted on as an insulator and silver epoxy would be painted on top of the PR to conduct power generated by the solar cells to the components on the underside of the microrobot. The components are then wirebonded and then the legs are assembled at the probe station.

6.2.2. Proposed assembly process for motorized legs and Smart Dust

Next, the Smart Dust components need to be mounted and electrically connected to the motorized MUMPs chip. Fig. 6-6 shows a proposed assembly process based on a technique already demonstrated in Smart Dust [85]. First, the solar array, CMOS controller and high voltage amplifier (from the solar cell process) are mounted on the MUMPS chip using silver epoxy. Note the MUMPs substrate is in contact with the solar array substrate and would serve as a common potential for the electronics and motors. The toughest challenge in this process is most likely to be wiring between the solar array and the power consuming components on the MUMPs chip. Fortunately, only two connections would be

needed from the solar array-- a low voltage (~1.5V) power line for the CMOS controller and a high voltage power line (~30V) for the motor buffer and motors. A thin layer of photoresist would be painted on one of the edges of the solar array/MUMPs chip as an insulator from the substrate. Silver epoxy would painted on top of the PR to conduct power generated by the solar cells to the components on the underside of the microrobot. The components would then be wirebonded and then the legs would be assembled at the probe station. The MUMPs legs are designed with polysilicon tethers that tie to down to the substrate. These keep the unassembled polysilicon plates from rotating unintentionally until they are ready to be assembled. To reduce the robot mass, the solar array chip should be thinned down. The final thickness should be lower than the thinned MUMPs chip because while the MUMPs chip still have to withstand the pressures from the flip-

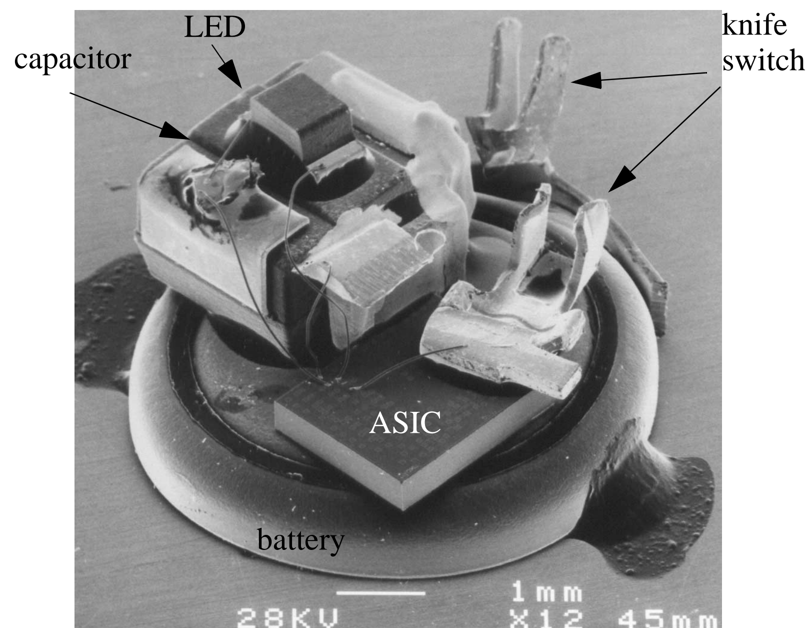

Fig. 6-7. SEM of a 138mm^3 Smart Dust node with light intensity dependent emissions. In this system, a resistor, 15μF capacitor, knife switch, green LED, and 0.35μm CMOS ASIC containing a photodiode, relaxation oscillator, frequency divider, current source, and current sink FET are mounted onto a 3V Mn-Li button cell. Courtesy of Brett Warneke [85].

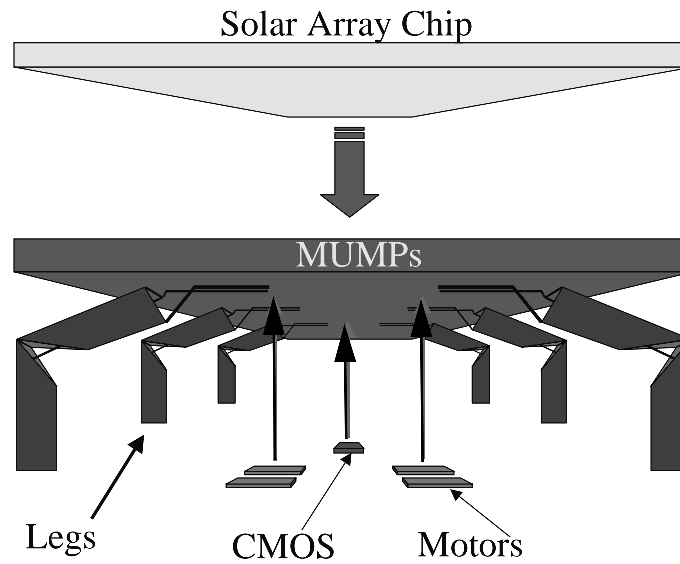

Fig. 6-8. Concept of microrobot component. The robot consists of six 2-DOF legs, motors for every link of each leg, a CMOS controller, motor buffer and a solar array chip.

chip bonder and subsequent handling in the HF etch bath the solar array chip needs only to be mounted on the MUMPs chip. An example device that demonstrates part of the proposed assembly process is the Smart Dust mote shown in Fig. 6-7 [85]. This device was assembled by mounting a capacitor, LED, application specific integrated circuit (ASIC) CMOS and wire connectors to a 3V Mn-Li button cell battery using silver epoxy and skillful wire bonding.

6.3 Power

Next, the power budget for the initial microrobot design shown in Fig. 6-8 is estimated. The initial autonomous microrobot design will be comprised of the basic elements described in Chapter 1: 1) legs (links and mechanical coupling), 2) motors, 3) solar cells, 4) motor buffers and 5) a CMOS controller. The robot would have six legs and use a alter-

nating tripod gait. Each leg will have two links for a total of 12 links so there will be 12 motors and 12 motor buffers. Table 6-1 shows the initial design.

Table 6-1: Initial Design for a six-Legged Microrobot

Component	Die Area (mm^2)	Mass (µg)	Power Consumption (µW)
Legs	6	27.6	---
Motors	36	4140	324µW
Motor Buffers	0.32	37	23µW
Solar Cells	---	23000	---
Controller	1	356	< 50nW
Mechanical support (MUMPS)	---	23000	---
Bond pads	---	---	54µW
Total	**43.3**	**50560**	**401µW**

Power is dissipated mainly by the motors, the CMOS controller and motor buffers. To calculate the power dissipated in the actuator, we estimate the forces needed to lift the weight of the microrobot and to overcome the adhesion forces in the mechanical coupling sliders of the microrobot. If we thinned both the $1cm^2$ MUMPs (leg) and solar array chips down to a thickness of 100µm, the combined weight of all components is approximately 0.5mN (50mg). From test structures, the adhesion forces sliders ranged from 2-100µN [95]. We arbitrarily multiplied the adhesion forces by a safety factor of ten to arrive at the estimated force of 1mN. Thus, each actuator should provide 1.5mN (weight + adhesion) of force.

Power dissipation for electrostatic gap-closing actuators was described in Chapter 3. To produce 1.5mN of force using a 30V supply and a 3µm initial gap in the GCA's, an

initial GCA capacitance of 10pF is required. If the final gap (as defined by the gap stop) is one third of the initial gap, then the final GCA capacitance will be three times the initial capacitance. If we operate the GCA at 1kHz, then the power dissipated in the motor will be 27μW. With 12 motors, the total power dissipation will be 324μW.

The energy cost for Smart Dust controllers is estimated to be about 1pJ/instruction for an 8-bit controller at 1V [23]. The energy cost of controlling the microrobot would depend on several factors including the number of motors, number of control signals per motor and the motor speed. The basic inchworm motor requires 4 bits to control (2 x-y actuator arrays). With 12 motors, the controller would need a 48-bits output. If the output registers are written sequentially, it would take 6 instructions to load (assuming 8-bit registers) and 1 instruction to simultaneously drive all 48 bits to the motor buffers. Therefore, it would take 7 instructions per step in the inchworm motor cycle described in Fig. 4-3. For a motor that operates at 1000 cycles per second, the power dissipation would be 7 $\frac{\text{instructions}}{\text{step}} \times 1000 \frac{\text{steps}}{\text{sec}} \times \frac{\text{1pJ}}{\text{instruction}} = 7\text{nW}$. In comparision, a CoolRISC core achieves an average energy consumption of 2.8pJ/instruction/bit on a 1.5V supply for a power consumption of around 150nW. Note that this does not include energy consumption of supporting components such as the SRAM or the clock. Although this overly simplifies the controller, it gives an estimate of the power consumption.

In addition, power is dissipated by the motor buffers. These buffers are CMOS converters with two transistors. Power dissipation in the buffer transistors is fundamentally based on two mechanisms: static leakage current and switching activity [23]. The power dissipated due to the first mechanism is:

$$= I_L V_{DD} \tag{6-1}$$

where I_L is the leakage current and V_{DD} is the supply voltage. The leakage current for these transistors is about 0.1μA. The power dissipated by the switching activity is:

$$P = \frac{Energy}{Cycle} \cdot \frac{Cycles}{Sec} = C_g V_{DD}^2 \cdot f \tag{6-2}$$

where C_g is the gate capacitance and f is the switching frequency. Using the above equations and transistor dimensions, we estimate that the 30V buffers from the solar cell process would dissipate roughly 23μW of power when driven with a 1kHz signal from the controller.

Finally, we estimate the power dissipated in the parasitic capacitances (bond pads and wires in the motors and controller) to be approximately 54μW. By adding all the power expenditures, the total power dissipation comes to roughly 421μW. Full sunlight has a power density of ~1mW/mm^2 and bright indoor illumination has about 1μW/mm^2. With 1cm^2 solar cell with a modest 10% conversion efficiency, the microrobot will have 10mW of power outdoors in full sunlight and 10μW indoors. Therefore, an indoor robot would have to operate at ~1% of the outdoor speed.

CHAPTER 7. CONCLUSION

7.1 Summary of Results

Articulated robot legs, mechanical couplings, inchworm motors and mechanical digital-to-analog converters have been presented. These devices, along with low-power CMOS controllers, solar cells and high-voltage transistors from Smart Dust, form the building blocks of a new class of autonomous microrobots.

Rigid links have been made by folding hinged polysilicon plates into a hollow triangular beam. These links can range from tens of microns to millimeters in length. By designing links in series with hinges connecting them, articulated multiple degrees-of-freedom (DOF) mechanisms can be created. Structures with up to 3-DOF have been fabricated with lengths of up to 2.4mm. One-DOF links have been tested to support up to 2.6gm of mass in the axial direction.

To connect rigid links to motors on the substrate, multiple DOF mechanical couplings have been created from four- and five-bar linkages. These mechanical couplings convert linear displacement of sliders on the substrate to angular rotation at the connected link. A 2-DOF leg with two links was fabricated with mechanical couplings for each link. A four-bar linkage (sliding crank) is used to couple the 1st link. A five-bar linkage in series of a four-bar linkage has 2 DOF and can be used to couple the 2nd link.

Electrostatic gap-closing actuators (GCA) can provide a force density on the order of $1mN/mm^2$ at 30V and an aspect ratio of 25:1. These densities improve as lithographic

limits decrease and anisotropic etch aspect ratios increase. GCA's are also limited in travel, so their large forces can only be applied over short distances. Fortunately, one GCA can be used to drive a clutch, allowing a second GCA to make intermittent contact with a moving shuttle. Repeated cycling through the gripping/pulling/releasing sequence generates large displacements while maintaining the full force available from the GCA primary using an inchworm-like motion.

Early problems with the electrostatic inchworm motors were related to clutch slipping, and clutch and gap-stop adhesion. The former problem has been addressed by using a gear teeth on the shuttle and clutch, and the latter by using a thicker SOI rather than thinner polysilicon structural layer. It is not clear why the adhesion problems have disappeared in the thicker single crystal silicon. The surface roughness of the sidewalls due to a DRIE etch may decrease the adhesion force, or the adhesion force may be relatively independent of film thickness, while the restoring force due to the support springs increases linearly with thickness.

Motors have been demonstrated with 80µm of travel, stepping rates of 1000 full steps/second corresponding to 4mm/s shuttle velocity, and ~260µN of force. In all cases, displacement was limited by contact with a physical constraint (spring travel limits, nearby structures, etc.) rather than an intrinsic limit.

For microrobot applications, the energy efficiency of these motors is very attractive. In addition, a motor with dimensions of 3mm x 1mm x 50µm can lift over 130 times its own weight with 33V. The inchworm motion of the motors with near-zero static power consumption is also attractive for solar powered bugs of the future, which may need to integrate charge for many milliseconds before each phase of motor actuation.

Lastly, as a demonstration of a novel idea conceived by Steve Burgett, mechanical digital-to-analog converters (DAC) have been realized. Four- and six-bit DAC's have been demonstrated in the MUMPs process and the motor SOI process. The DAC's are less sensitive to input signal noise and loading effects due to its mechanical digital design and stiff output. Due to these properties, DAC's could potentially be used in microrobots for open-loop actuation of linkages where joint angle information is difficult to obtain. The main drawback of the DAC's is the total travel is small, limited to less than twice the stroke of the input bit actuators.

7.2 Future research directions

The work presented here along with Smart Dust are the first steps towards an autonomous microrobot. Future microrobotic research should focus on integration, component optimization, and systems design.

7.2.1. Integration/Assembly

Although rigid articulated legs were fabricated in MUMPs, earlier attempts to fabricate motors on the same chip were less successful due to stiction problems. Subsequently, motors were fabricated and demonstrated in the SOI/DRIE process. Transfer of these SOI motors to the MUMPs legs is one option to explore. However, there are many alternatives to also consider. One option would be to fabricate both legs and motors in the same SOI process. This will require additional structural layers to create mechanical couplings. To accomplish this, we can bond a thin SOI layer (~2μm) to the the SOI wafer or to planarize the SOI wafer after etching. The second option would allow traditional surface micromachining of polysilicon on top of the thick SOI devices. Another option is combine the solar cell process with the motors and legs since the solar cells are also fabri-

cated on the SOI wafers. This option would greatly simplify the assembly issue as the only components to be assembled is the CMOS controller. However, it also poses the challenge of integrating CMOS with mechanical structures. Recent work with integrating SiGe with CMOS could be a solution [29].

7.2.2. Optimization

The electrostatic inchworm motors presented in this work demonstrates the feasiblity of an efficient actuator with large force and large displacement. The 8% efficiency is decent but there is a lot more room in theory to improve. Currently, the motors operate with voltage-controlled step input, which has an efficiency limit of 50%. Adiabatic charging should be explored. The relatively slow mechanical response time of the micromotor compared to its the electrical constant allows slower linearly-ramped charging which could increase the efficiency limit to ~90%.

In addition to efficiency, power density can be improved with scaling. Advances in lithography and etch aspect ratio should both improve the performance of electrostatic gap-closing actuators. The motors presented here are based on 2μm lithography, with most features 3μm or larger. Based on a simple dynamic model, it appears that these designs could be directly scaled down by a factor of 3 without a decrease in actuation voltage, and without seeing serious squeeze-film damping effects. Such a scaled motor would have the same force output, and the same velocity (smaller, faster steps), but only one tenth the layout area. Deep sub-micron scaling with this exact design will necessitate voltage scaling, but a careful mechanical re-design should enable motors that are ultimately limited by field emission from the GCA's, rather than destructive pull-in.

The legs dimensions can also be optimized. It is still not clear what the legs should look like for the microrobot. A lot of it would have to do with its task and terrain. Insect locomotion could provide an insight to what the optimal number of links and the dimensions of each link should be.

7.2.3. Computer aided design

The optimizations mentioned above would require simulations tools. Ideally, these simulation tools would take process information, layout, and electrical input parameters to simulate the kinematics and dynamics of the microrobot coupled with motors. In addition, a library of parameterized components would allow microrobots to be designed on a schematic level. Genetic algorithms may be an interesting approach to optimizing microrobots. Needless to say, no such tools exists yet. Instead, continued improvements on the current tools would be more practical.

An assembly simulator with collision detection would be useful for hinged structures. This would allow designers to assemble hinged structures before fabrication. 3DμV is a good start [56]. The drawback is that the simulator can not recognize hinges from the layout and instead, hinges needed to be specified by the designer with a special layer.

Simulations of planar structures with electrical and mechanical models is possible with SUGAR [19] which runs on Matlab and uses nodal analysis for faster simulation compared with finite element analysis. SUGAR is well suited for simulating planar structures such as the micromotor and the mechanical digital-to-analog converter. The drawback here is a lack of a layout extracter and damping models. A commercial program by Conventor, MEMCAD, which uses finite element analysis to extract device parameters for

the faster nodal analysis of mutliple interacting devices is another potential simulator for microrobots.

Overall, autonomous microrobotics and Smart Dust will continue to push the limits of miniaturiation of computing, sensing, commucations, and actuation of micromechanisms. Autonomous microrobots will definitely be realized in the next few years and could become a household item by the next decade.

BIBLIOGRAPHY

[1] T. Akiyama, D. Collard, and H. Fujita, **“**Scratch drive actuator with mechanical links for self-assembly of three-dimensional MEMS**,”** Journal of Microelectromechanical Systems, vol.6, no.1, IEEE, March 1997. p.10-17

[2] T. Akiyama and H. Fujita, “A quantitative analysis of Scratch Drive Actuator using buckling motion,” Proceedings. IEEE Micro Electro Mechanical Systems, Amsterdam, Netherlands, Jan. 29 - Feb. 2, 1995, pp. 310-15.

[3] M. Ataka, A. Omodaka, N. Takeshima, and H. Fujita, “Fabrication and operation of polyimide bimorph actuators for a ciliary motion system,” Journal of Microelectromechanical Systems, vol.2, no.4, Dec. 1993, pp.146-50.

[4] W.C. Athas, L.J. Svensson, J.G. Koller, N. Tzartanis, and E.Y. Chou, “Low-power digital systems based on adiabatic-switching principles,” IEEE Transactions on VLSI Systems, vol. 2, Dec., 1994, pp. 398-406.

[5] B. Atwood, B. Warneke, and K.S.J. Pister, “Preliminary circuits for smart dust,” 2000 Southwest Symposium on Mixed-Signal Design, Feb. 27-29, 2000, San Diego, CA, USA, pp.87-92

[6] F. Ayazi and K. Najafi, “High aspect-ratio combined poly and single-crystal silicon (HARPSS) MEMS technology,” Journal of Microelectromechanical Systems, vol.9, no.3, IEEE, Sept. 2000. pp.288-94.

[7] F. Ayazi and K. Najafi, “High aspect-ratio polysilicon micromachining technology,” Sensors and Actuators A (Physical), vol.A87, no.1-2, Dec. 1, 2000. pp.46-51.

[8] M. Baltzer, T. Kraus, and E. Obermeier, “A linear stepping actuator in surface micromachining technology for low voltages and large displacements,” Interna-

tional Conference on Solid-State Sensors and Actuators, Chicago, IL, USA, June 16-19, 1997, vol. 2, pp. 781-4.

[9] C. Bellew, "An SOI Process for the Fabrication of Solar Cell Arrays and Transistors," research report for the Master of Science degree in Mechanical Engineering, December, 2000.

[10] R.A. Brennen, M.G. Lim, A.P. Pisano, and A.T. Chou, "Large displacement linear actuator," Technical Digest. IEEE Solid-State Sensor and Actuator Workshop, Hilton Head Island, SC, USA, June 4-7, 1990, pp.135-9.

[11] T.J. Brosnihan, J.M. Bustillo, A.P. Pisano, and R.T. Howe, "Embedded interconnect and electrical isolation for high-aspect-ratio SOI inertial instruments," 1997 International Conference on Solid-State Sensors and Actuators, Chicago, IL, USA, June 16-19, 1997. pp. 637-40.

[12] M.R. Boyd, S.B. Crary, and M.D. Giles, "A heuristic approach to the electromechanical modeling of MEMS beams," in Proc. Solid-State Sensor and Actuator Workshop Hilton Head, SC, USA, June 13-16, 1994, pp. 123-126.

[13] M. Calin, N. Chaillet, J. Agnus, A. Bourjault, A. Bertsch, and S. Zissi, L. Thiery, (Edited by: G. Morel and F.B. Vernadat), "Shape memory alloy compliant microrobots," A Proceedings volume from the 9th Information Control in Manufacturing Symposium, Nancy-Metz, France, 24-26 June 1998, vol.1, pp.241-8.

[14] H-D. Chai, Electromechanical Motion Devices, New Jersey, Prentice Hall, 1998, p.1.

[15] C. Liu, T. Tsao, Y-C. Tai, and C-M. Ho, "Surface micromachined magnetic actuators," Proceedings IEEE Micro Electro Mechanical Systems. An Investigation of

Micro Structures, Sensors, Actuators, Machines and Robotic Systems, Oiso, Japan, Jan. 25-28, 1994, pp.57-62.

[16] P.B. Chu, N.R. Lo, E. Berg, and K.S.J. Pister, “Optical Communications Using Micro Corner Cube Reflectors,” Tenth IEEE International Micro Electro Mechanical Systems Conference (MEMS ‘97), Nagoya, Japan, Jan. 26-30, 1997, pp. 350-5.

[17] P.B. Chu, J.T. Chen, R. Yeh, G. Lin, J.C.P. Huang, B.A. Warneke, and K.S.J. Pister, “Controlled pulse-etching with xenon difluoride**,”** Proc. of The Ninth International Conference on Solid-State Sensors and Actuators, Chicago, IL, USA, June 16-19, 1997, pp.665-8.

[18] P.B. Chu and K.S.J. Pister, “Analysis of closed-loop control of parallel-plate electrostatic microgrippers,” Proc. IEEE International Conference on Robotics and Automation, San Diego, California, May 8-13, 1994, vol.1, pp. 820-5.

[19] J.V. Clark, N. Zhou, and K.S.J. Pister, “MEMS simulation using SUGAR v0.5,” Technical Digest. Solid-State Sensor and Actuator Workshop, Hilton Head Island, SC, USA, June 8-11, 1998, pp.191-6.

[20] D. Collard, Y. Fukuta, T. Akiyama, D. Chauvel, H. Fujita, **“**Integrated motion system for self-alignment of micro-optical devices,” Proceedings of the SPIE - The International Society for Optical Engineering, vol.2783, (Micro-Optical Technologies for Measurement, Sensors, and Microsystems, Besancon, France, June 12-13, 1996, pp.117-24.

[21] J. Comtois and V. Bright, “Applications for surface-micromachined polysilicon thermal actuators and arrays,” Sensors and Actuators A (Physical), Vol. A58, no. 1, pp. 19-25.

[22] R.A. Conant, R. S. Muller, "Cyclic Fatigue Testing of Surface-Micromachined Thermal Actuators," presented at the 1998 ASME International Mechanical Engineering Congress and Exposition, Nov 15-20, 11998, Anaheim, CA, DSC-Vol. 66, pp. 273-277.

[23] L. Doherty, B.A. Warneke, B.E. Boser, K.S.J. Pister, “Energy and Performance Considerations for Smart Dust,” to be published in a special issue of the International Journal of Parallel and Distributed Systems and Networks, 2001.

[24] T. Ebefors, J. U. Mattsson, E. Kalvesten, and G. Stemme, “A walking silicon microrobot,” Proc. The Tenth International Conference on Sensors and Actuators (Transducers '99), Sendai, Japan, June 7-10, 1999, pp. 1202-1205.

[25] R.S. Fearing, “Powering 3 Dimensional Microrobots: Power Density Limitations,” Tutorial on Micro Mechatronics and Micro Robotics, ICRA, 1998.

[26] P.E. Kladitis, V.M. Bright, K.F. Harsh, and Y.C. Lee, “Prototype microrobots for Micro positioning in a manufacturing process and micro unmanned vehicles,” Proceedings of The Twelfth IEEE International Conference on Micro Electro Mechanical Systems, January 17-21, 1999, pp. 570-5.

[27] R. Feynman, “There’s Plenty of Room at the Bottom,” talk given at the 1959 Meeting of the Americal Physical Society reprinted in the Journal of Microelectromechanical Systems, Vol. 1, No. 1, March, 1992, pp. 60-66.

[28] A.M. Flynn, L.S. Tavrow, S.F. Bart, R.A. Brooks, D.J. Ehrlich, K.R. Udayadumar, and L.E. Cross, “Piezoelectric micromotors for microrobots,” Journal of Microelectromechanical Systems, Vol. 1, No. 1, March, 1992, pp. 44-51.

[29] A.E. Franke, D. Bilic, D.T. Chang, P.T. Jones, T.-J. King, R.T. Howe, and G.C. Johnson, “Post-CMOS integration of germanium microstructures,” Proceedings of 12th International Workshop on Micro Electro Mechanical Systems - MEMS, Orlando, FL, USA, Jan. 17-21,1999, pp.630-7.

[30] T. Fukuda, A. Kawamoto, F. Arai, and H. Matsuura, “Steering mechanism and swimming experiment of micro mobile robot in water,” in Proc. IEEE Workshop on Micro Electro Mechanical Systems (MEMS ’95), Amsterdam, The Netherlands, Jan. 29-Feb. 2, 1995, pp. 300-305.

[31] E.J. Garcia and J.J. Sniegowski, “Surface Micromachined Microengine,” Sensors and Actuators A (Physical), Vol. A48, no. 3, pp. 203-14.

[32] M. Gebhard and W. Benecke, “Microtechnologies for microscaled robots and components,” Proceedings 1995 INRIA/IEEE Symposium on Emerging Technologies and Factory Automation. ETFA'95, vol.3, Paris, France, 10-13 Oct. 1995, pp.9-20.

[33] F.J. Gil and J.M. Guilemany, “Energetic evaluation for inducing the thermoelastic martensitic transformation by mechanical stress in Cu-Zn-Al single crystals,” Intermetallics, vol.7, no.6, Elsevier, 1999. p.699-704.

[34] T.S. Gray, Applied Electronics; a first course in electronics, electron tubes, and associated circuits, 2nd edition, Cambridge, The MIT Press, 1954, p. 154.

[35] G. Lim, K. Minami, M. Sugihara, M. Uchiyama, and M. Esashi, “Active catheter with multi-link structure based on silicon micromachining,” in Proc. IEEE Workshop on Micro Electro Mechanical Systems (MEMS ’95), Amsterdam, The Netherlands, Jan. 29-Feb. 2, 1995, pp. 116-121.

[36] H. Guckel, J. Klein, T. Christenson, K. Skrobis, M. Laudon, E.G. Lovell, “Thermo-magnetic metal flexure actuators,” Technical Digest. IEEE Solid-State Sensor and Actuator Workshop, Hilton Head Island, SC, June 22-25, 1992, p.73-5.

[37] D.S. Gunawan, L.-Y. Lin, K.S.J. Pister, “Micromachined corner cube reflectors as a communication link,” Sensors and Actuators A (Physical), vol.A47, (no.1-3), (EUROSENSORS VIII, Toulouse, France, 25-28 Sept. 1994.) March-April 1995. pp.580-3.

[38] S. Hollar, unpublished work on deep trench planarization using custom-made spin-on-glass, March, 2000.

[39] M.R. Houston, R. Maboudian, and R.T. Howe, “Self-assembled monolayer films as durable anti-stiction coatings for polysilicon microstructures,” Technical Digest of the Solid-State Sensor and Actuator Workshop, Hilton Head Island, SC, USA, 3-6 June 1996, pp.42-7.

[40] V. S. Hsu, J.M. Kahn, and K.S.J. Pister, “Wireless Communications for Smart Dust,” UC Berkeley Electronics Research Laboratory Memorandum, Jan. 30, 1998.

[41] K. Ikuta, “Micro/miniature shape memory alloy actuator,” Proceedings 1990 IEEE International Conference on Robotics and Automation, Cincinnati, OH, USA, May 13-18, 1990, pp.2156-61.

[42] T. Indermaur and M. Horowitz, “Evaluation of charge recovery circuits and adiabatic switching for low power CMOS design,” IEEE Symposium on Low Power Electronics. Digest of Technical Papers, San Diego, CA, USA, Oct. 10-12, 1994, pp.102-3.

[43] J. Judy, "Batch-fabricated ferromagnetic microactuators with silicon flexures," Doctoral dissertation, University of California at Berkeley, Fall, 1996.

[44] C.G. Keller and R.T. Howe, "HEXSIL Tweezers for Teleoperated Micro-Assembly," Proceddings of the Tenth Annual Workshop of Micro Electro Mechanical Systems, Nagoya, Japan, Jan. 26-30, 1997, pp. 72-77.

[45] P.E. Kladitis, V.M. Bright, K.F. Harsh, and Y.C. Lee, "Prototype Microrobots for Micro Positioning in a Manufacturing Process and Micro Unmanned Vehicles," Proceedings of The Twelfth IEEE International Conference on Micro Electro Mechanical Systems, January 17-21, 1999, pp. 570-5.

[46] P.E. Kladitis, R.J. Linderman, and V.M. Bright, "Solder self-assembled micro axial flow fan driven by a scratch drive actuator rotary motor," Technical Digest 14th IEEE International Conference on Micro Electro Mechanical Systems, Interlaken, Switzerland, Jan. 21-25, 2001. pp.598-601.

[47] G.T.A. Kovacs, <u>Micromachined Transducers Sourcebook</u>, WCB McGraw-Hill, 1998.

[48] E.J.J. Kruglick, "Microrelay design, performance, and systems," Ph.D. dissertation, Spring, 1999.

[49] P. Krulevitch, A.P. Lee, R.B. Ramsey, J.C. Trevino, J. Hamilton, and M.A. Northrup, "Thin film shape memory alloy microactuators," Journal of Microelectromechanical Systems, vol.5, no.4, IEEE, Dec. 1996. p.270-82.

[50] K. Kuribayashi, T. Taniguchi, M. Yositake, and S. Ogawa, (Edited by: A.P. Jardine, G.C. Johnson, A. Crowson, and M. Allen), "Micron sized arm using reversible TiNi alloy thin film actuators," Smart Materials Fabrication and Materials for Micro-

Electro-Mechanical Systems, San Francisco, CA, USA, April 28-30, 1992, pp.167-75.

[51] A.P. Lee, D.R. Ciarlo, P.A. Krulevitch, S. Lehew, J. Trevino, and M.A. Northrup, “A practical microgripper by fine alignment, eutectic bonding and SMA actuation,” Proceedings of the International Solid-State Sensors and Actuators Conference, Stockholm, Sweden, 25-29 June 1995, pp.755-9.

[52] S-S. Lee, L-S. Huang, C-J. Kim and M-C. Wu, **“**Free-space fiber-optic switches based on MEMS vertical torsion mirrors**,”** Journal of Lightwave Technology, vol.17, (no.1), IEEE, Jan. 1999. p.7-13.

[53] B. Leibowitz, B. E. Boser, and K. S. J. Pister, "CMOS 'smart pixel' for free-space optical communication," Proceedings of the SPIE - The International Society for Optical Engineering, vol. 4306A (Electronic Imaging '01), San Jose, CA, 21-26 January 2001.

[54] L.Y. Lin, J.L. Shen, S.S. Lee, and M.C. Wu, ”Surface-micromachined micro-XYZ stages for free-space microoptical bench**,”** IEEE Photonics Technology Letters, vol.9, no.3, IEEE, March 1997. p.345-7.

[55] R.J. Linderman, V.M. Bright, **“**Optimized scratch drive actuator for tethered nanometer positioning of chip-sized components**,”** Technical Digest. Solid-State Sensor and Actuator Workshop, Hilton Head Island, SC, USA, June 4-8, 2000, pp.214-17.

[56] N.R. Lo and K.S.J. Pister, “3D µV-a MEMS 3-D visualization package,” Proceedings of the SPIE - The International Society for Optical Engineering, vol.2642, Micromachined Devices and Components, Austin, TX, USA, Oct. 23-24, 1995, pp.290-5.

[57] A. Luque and G.L. Araujo, Physical Limitations to Photovoltaic Energy Conversion, New York, Adam Hilger (IOP Publishing Ltd), 1990, p. 122.

[58] M. Maharbiz, R.T. Howe, and K.S.J. Pister, “Batch Transfer Assembly of Micro-Components to Surface and SOI MEMS,” Proc. of The 10th International Conference on Solid-State Sensors and Actuators, Sendai, Japan, June 7-10, 1999, pp. 787-92

[59] V. Milanovic, L. Doherty, D.A. Teasdale, S. Parsa, and K.S.J. Pister, “Micromachining technology for lateral field emission devices,” IEEE Transactions on Electron Devices, vol.48, no.1, IEEE, Jan. 2001. pp.166-73.

[60] V. Milanovic, M. Last, and K.S.J. Pister, “Torsional Micromirrors with Lateral Actuators,” to be presented at the 11th International Solid State Sensors and Actuators Conference (Transducers '01), Munich, Germany, June 10-14, 2001.

[61] N. Miki and I. Shimoyama, “Flight performance of micro-wings rotating in an alternating magnetic field,” Technical Digest. Twelfth IEEE International Conference on Micro Electro Mechanical Systems, Orlando, FL, USA, 17-21 Jan. 1999

[62] G.T. Mulhern, D.S. Soane, and R.T. Howe, “Supercritical Carbon Dioxide Drying of Microstructures,” in Tech. Dig. 7th International Conference on Solid-State Sensors and Actuators (Transducers ‘93), 1993, pp. 296-298.

[63] H. Nguyen, J.G.-D. Su, H. Toshiyoshi, and M.C. Wu, “Device Transplant of Optical MEMS for out of plane beam steering,” Proceedings of the Fourteenth Annual International Conference on Microelectromechanical Systems (MEMS 2001), Interlaken, Switzerland, January 21-25, 2001, pp. 325-328.

[64] P.M. Osterberg and S.D. Senturia, "M-Test: A test chip for MEMS material property measurement using electrostatically actuated test structures," Journal of Microelectromechanical Systems, Vol. 6, No. 2, June, 1997, pp. 107-118.

[65] F. Paschen, Ann. Physik, vol. 37, p.69, 1889.

[66] P. Patra and D.S. Fussell, "On efficient adiabatic design of MOS circuits," in Proc. Fourth Workshop Physics Computation, 1996, pp. 260-269.

[67] S. Paul, A.M. Schlaffer, and J.A. Nossek, "Optimal Charging of Capacitors," IEEE Trans. on Circuits and Systems--I: Fundamental Theory and Applications, Vol. 47, No. 7, July, 2000, pp. 1009-16.

[68] K.S.J. Pister, M.W. Judy, S.R. Burgett, and R.S. Fearing, "Microfabricated hinges," Sensors and Actuators A (Physical), vol.A33, (no.3), June 1992. p.249-56.

[69] Proceedings of the IEEE Micro Robots and Teleoperators Workshop. An Investigation of Micromechanical Structures, Actuators and Sensors, Hyannis, MA, USA, 9-11 Nov. 1987.

[70] M.T.A Saif and N. MacDonald, "A millinewton microloading device," Proc. The Eighth International Conference on Sensors and Actuators (Transducers '95), Stockholm, Sweden, June 25-29, 1995, pp. 60-3, Vol. 2.

[71] I. Shimoyama, H. Miura, C. Kimura, and M. Kikuta, "Analyzing the dynamics of ants and application to microrobots," in Proc. ASME Winter Annual Meeting, Dynamic Systems and Control, Micromechanical Sensors, Actuators, and Systems, Atlanta, Georgia, Dec. 1-6, 1991, Vol. 32, pp. 279-284.

[72] A. Singh, D.A. Horsley, M.B. Cohn, A.P. Pisano, and R.T. Howe, R.T., "Batch transfer of microstructures using flip-chip solder bump bonding," Proceedings of

International Solid State Sensors and Actuators Conference (Transducers '97), Chicago, IL, USA, 16-19 June 1997, pp. 265-8.

[73] J.H. Smith, "Monolithic integration of CMOS with smart sensors," Proceedings Sensors Expo. Boston, MA, USA, 13-15 May 1997.

[74] J.G. Smits, "Design considerations of a piezoelectric-on-silicon microrobot," Sensors and Actuators A, Vol. 35, 1992, pp. 129-135.

[75] U. Srinivasan, M.R. Houston, R.T. Howe, and R. Maboudian, "Alkyltrichlorosilane-based self-assembled monolayer films for stiction reduction in silicon micromachines," Journal of Microelectromechanical Systems, vol.7, no.2, IEEE, June 1998. pp.252-60.

[76] U. Srinivasan, D. Liepmann, and R.T. Howe, "Microstructure to substrate self-assembly using capillary forces," Journal of Microelectromechanical Systems, vol.10, no.1, March 2001. pp.17-24.

[77] J.B. Starr, "Squeeze-film damping in solid-state accelerometers," IEEE Proc. Solid State Sensor and Actuator Workshop, Hilton Head, South Carolina, June 4-7, 1990, pp. 44-47.

[78] G-D.J. Su, S-S. Lee, and M.C. Wu, "Optical scanners realized by surface-micromachined vertical torsion mirror," IEEE Photonics Technology Letters, vol.11, no.5), IEEE, May 1999. pP.587-9.

[79] K. Suzuki, I. Shimoyama, H. Miura, and Y. Ezura, "Creation of an insect-based microrobot with an external skeleton and elastic joints," in Proc. IEEE Workshop on Micro Electro Mechanical Systems (MEMS '92), Travemunde, Germany, Feb. 4-7, 1992, pp. 190-195.

[80] N. Tas, J. Wissink, L. Sander, T. Lammerink, and M. Elwenspoek, “Modeling, design and testing of the electrostatic shuffle motor,” Sensors and Actuators A (Physical), Vol.A70, no.1-2, Oct. 1, 1998, pp.171-8.

[81] N. Takeshima and H. Fujita, “Fabrication and operation of polyimide bimorph actuators for a ciliary motion system,” in Proc. ASME Winter Annual Meeting, Micromechanical Sensors, Actuators, and Systems, Atlanta, Georgia, Dec. 1-6, 1991, Vol. 32, pp. 203-209.

[82] W.C. Tang, T-C.H. Nguyen, and R.T. Howe, R.T., “Laterally driven polysilicon resonant microstructures,” Sensors and Actuators, vol.20, no.1-2, 15 Nov. 1989. p.25-32.

[83] A. Teshigahara, M. Watanabe, N. Kawahara, Y. Ohhtsuka and T. Hattori, “Performance of a 7-mm microfabricated car,” Journal of Microelectromechanical Systems, Vol. 4, pp. 76-80, 1995.

[84] H. Toshiyoshi, D. Kobayashi, M. Mita, G. Hashiguchi, H. Fujita, J. Endo, and Y. Wada, “Micro Electro Mechanical Digital-to-Analog Converter (MEMDAC),” Proc. of The 10th International Conference on Solid-State Sensors and Actuators, Sendai, Japan, June 7-10, 1999, pp. 994-997.

[85] B. Warneke, B. Atwood, and K.S.J. Pister, "Smart Dust Mote Forerunners," Proceedings of the Fourteenth Annual International Conference on Microelectromechanical Systems (MEMS 2001), Interlaken, Switzerland, January 21-25, 2001, pp. 357-360.

[86] D. Wood, J.S. Burdess, and A.J. Harris, “Actuators and their mechanisms in microengineering,” Engineering Science and Education Journal, vol.7, no.1, Feb. 1998. p.19-27.

[87] T. Yasuda, I. Shimoyama, and H. Miura, “Microrobot actuated by a vibration energy field,” in Tech. Dig. 7th International Conference on Solid-State Sensors and Actuators (Transducers ‘93), Yokohama, Japan, June 7-10, 1993, pp. 42-45.

[88] A.A. Yasseen, J. D. Cawley, M. Mehregany, “Thick glass film technology for polysilicon surface micromachining,” Journal of Microelectromechanical Systems, Vol. 8, No. 2 , June 1999, pp. 172 -179

[89] J-L.A. Yeh, H. Jiang and N.C. Tien, “Integrated polysilicon and DRIE bulk silicon micromachining for an electrostatic torsional actuator,” Journal of Microelectromechanical Systems, Vol. 8, No. 4, Dec. 1999, pp. 456-65.

[90] R. Yeh, R. Conant, and K.S.J. Pister, “Mechanical Digital-to-Analog Converters,” Proc. of The 10th International Conference on Solid-State Sensors and Actuators, Sendai, Japan, June 7-10, 1999, pp. 998-1001.

[91] R. Yeh, S. Hollar, and K.S.J. Pister, "A Single Mask, Large Force, and Large Displacement Electrostatic Inchworm Motor," Proceedings of the Fourteenth Annual International Conference on Microelectromechanical Systems (MEMS 2001), Interlaken, Switzerland, January 21-25, 2001, pp. 260-264.

[92] R. Yeh, E.J.J. Kruglick, and K.S.J. Pister, "Microelectromechancial Components for Articulated Microrobots", Proc. The Eighth International Conference on Sensors and Actuators (Transducers '95), Stockholm, Sweden, June 25-29, 1995, pp. 346-349.

[93] R. Yeh, E.J.J. Kruglick, and K.S.J. Pister, "Surface-micromachined components for articulated microrobots", Journal of Microelectromechanical Systems, March 1996, Vol. 5, No. 1, pp. 10-17.

[94] R. Yeh, E.J.J. Kruglick, and K.S.J. Pister, “Towards an articulated silicon microrobot,” in Proc. ASME Winter Annual Meeting, Micromechanical Systems, Chicago, Illinois, Nov. 6-11, 1994, DSC-vol 55-2, pp. 747-754.

[95] Yeh, R. and Pister, K.S.J., "Measurement of Static Friction in Mechanical Couplings of Articulated Microrobots," The International Society for Optical Engineering, vol.2642, Micromachined Devices and Components, Austin, TX, USA, Oct. 23-24, 1995. pp.40-50.

[96] S.G. Younis and T.F. Knight Jr., “Non-dissipative rail drivers for adiabatic circuits,” Proc. Sixteenth Conference on Advanced Research in VLSI, Chapel Hill, NC, USA, March 27-29, 1995, pp. pp. 404-14.

APPENDIX A. MATLAB CODE FOR FORCE OPTIMIZATION OF GAP-CLOSING ACTUATOR ARRAYS

This appendix contains the Matlab code for optimizing gap-closing actuator (GCA) arrays for high force density. The inputs are minimum feature size, etch aspect ratio and maximum allowable voltage. The output is the optimum seperation between GCA units, maximum force density and dimensions of the electrodes at the maximum force density.

```
clear;
% Young’s modulus of Silicon
mod=150e9;
% Permittivity of air or vacuum
epsi=8.85e-12;
% initial gap
do=input('Initial Gap (um)= ')*1e-6;
% actuator stroke-> min feature size should be used
d=input('Actuator Stroke (um)= ')*1e-6;
v=input('Maximum applied Voltage (V)= ');
% silicon etcher aspect ratio
ar=input('Silicon Etcher Aspect Ratio (depth/width of trench)= ');
%  optimum electrode thickness is a function of the aspect ratio and min gap
t=ar*d;
% number of points to plot per width and length
points=50;
% width
w_start=d;
w_end=7e-6;
w_points=points;
w_step=(w_end-w_start)/w_points;
% length
len_start=10e-6;
len_end=600e-6;
len_points=points;
```

```
len_step=(len_end-len_start)/len_points;
len_support=100e-6;
% separation between gca unit cells normalized to initial gap (do)
z_start=1.1;
z_end=3;
z_step=.1;

x=1;
y=1;
z=1;

for l=z_start:z_step:z_end,
for i=w_start:w_step:w_end,
  for j=len_start:len_step:len_end,
    vmax(x,y,z)=sqrt((0.28*mod*i^3*d^3)/(epsi*j^4*(1+0.42*(i/t))));
    if vmax(x,y,z)>v,
      vm=v;
    else
      vm=vmax(x,y,z);
    end
    fe1(x,y,z)=(0.5*epsi*t*j*vm^2)/do^2;
    fe2(x,y,z)=(0.5*epsi*t*j*vm^2)/(l*do)^2;
    vol(x,y,z)=(d*(l+1)+2*i)*t*(j+len_support);
                fd(x,y,z)=(fe1(x,y,z)-fe2(x,y,z))/vol(x,y,z);
    length(y)=j;
        y=y+1;
        end
  y=1;
  width(x)=i;
  x=x+1;
end
% find max fd for each z
maxfd(z)=max(max(fd(:,:,z)));
x=1;
sep(z)=l;
z=z+1;
end
% find dimensions for max fd
% x = width
% y = length
% z = separation (factor of gap)

% returns the max fd and the z at max force density (fd)
[fdmax,zmax]=max(maxfd);
% returns the max fd of each column of fd(:,:,zmax) <-- 2x2 matrix
[a,b]=max(fd(:,:,zmax),[],1);
```

```
% 'a' is a vector where each element is the max fd of length
% b is a vector giving the row of the max length
[fdmax,i]=max(a);% find max fd in 'a'

% optimum [width length z fd(mN/mm^2)]
optimum=[width(b(i)) length(i) sep(zmax) fdmax*t*1e-3]

figure(1)
mesh(length*1e6,width*1e6,fd(:,:,zmax)*t*1e-3)
title(‘maximum force density vs. width and length’)
ylabel('width (um)')
xlabel('length (um)')
zlabel('fd (mN/mm^2)')

figure(2)
plot(sep,maxfd*t*1e-3)
title(‘maximum force density vs gca unit seperation’)
xlabel('separation (normalized to initial gap)')
ylabel('force density (mN/mm^2)')
```

APPENDIX B. SINGLE MASK MOTOR PROCESS

The following is the process flow that was used to fabricate the motors and, later on, the mechanical digital-to-analog converters. The process here is for a 15μm-thick SOI device layer. Thicker device layers have also been processed but the STS etch time would have to be adjusted according to the latest etch rate data. All steps and modules are performed in the Berkeley Microfabrication Laboratory (BML, see http://www-microlab.eecs.berkeley.edu). All equipment names are in *italics*. Two often-used standard BML modules are given at the end of the appendix.

Starting material: 4" SOI wafer, 2μm-thick buried thermal oxide, 15μm-thick device layer, resistivity of ~3-5 $\Omega \cdot cm$, device orientation <100>, substrate thickness/resistivity/orientation varies (does not matter).

Motor/DAC Process:

1. Grow 5000Å of wet thermal oxide for the oxide mask
    - 1.1 Standard clean module
    - 1.2 *Tylan 3/4*: Wet oxidation, program "SWETOXB," 1000ºC, t=1:40:00
2. Pattern trench mask
    - 2.1 Standard lithography module
    - 2.2 Hardbake

VWR convection oven, 120ºC, 45min

2.3 Etch 5000Å oxide

LAM 2, recipe= "SIO2ET.RCP", 30 sec

2.4 Strip PR

Sink 5: PRS-3000, 90ºC, 10min

Spindry

2.5 Standard clean module (dirty piranha only)

3. Etch device layer down to the buried oxide layer (nominal etch depth of 15µm)

3.1 STS, recipe HEXA100, t=19min (need to manually check for endpoint)

4. Dice

4.1. Disco saw, diamond blade, speed 10cm/s, remaining depth=115µm

5. Release structure

5.1. Etch individual chips in 49% hydrofluoric acid (HF), t=4min (depends on design rules for etch holes)

5.2. DI rinse until pH=7

5.3 Soak in methanol, t=30sec

5.4 Repeat above step three times to remove water from chip

5.5 CO_2 critical point dryer (CPD), rinse time=10min. Do not let samples dry during the transfer from methanol to the CPD chamber.

Module 1: Standard clean

1.1. "Dirty" piranha clean at *Sink 8*

1.1.1. Sulfuric acid and 100ml of H_2O_2 at 120ºC, t=0:10:00

1.1.2. De-ionizied (DI) water dip

1.1.3. Rinse to 10 MΩ-cm

1.1.4. Spin dry

1.2 "Clean" piranha clean at *Sink 6*

1.2.1. Sulfuric acid and 100ml of H_2O_2 at 120ºC, t=0:10:00

1.2.2. De-ionizied (DI) water dip

1.2.3. Rinse to 10 MΩ-cm

1.2.4. Spin dry

Module 2: Standard Lithography

2.1. HMDS

Primeoven: Program 0, ~120ºC, t~35min

2.2. Spin on photoresist (PR)

Svgcoat 1/2:

Spinner program 2: OCG 825 positive PR, 5000RPM, ~1.3µm

Bake program 1: 90ºC, 1min

2.3. Expose PR

*GCAWS*2 *stepper,* exposure=0.6ms, focus=250

(exposure time and focus varies with temperature, stepper calibration, etc.)

2.4. Develop PR

Svgdev: developer program 2, bake program 9 (no post exposure bake)

OCG 934, 1:1 volumetric ratio with DI.

2.5. Descum

Technics-C: gas=O2, power=50W, t=1min